Toward an affordable multi-modal motion capture system framework for human kinematics and kinetics assessment

Randa Mallat

École Doctorale MSTIC & École Doctorale EDST

Laboratoire Images, Signaux et Systèmes Intelligents
&
Centre AZM pour la recherche en biotechnologie

THÈSE EN COTUTELLE

Présentée pour l'obtention du grade de
DOCTEUR DE L'UNIVERSITÉ PARIS-EST
& L'UNIVERSITÉ LIBANAISE
par

Randa MALLAT

Toward an Affordable Multi-Modal Motion Capture System Framework for Human Kinematics and Kinetics Assessment

Analyse multimodale à bas coût pour l'évaluation de la cinématique et la dynamique des mouvements humains

---

Spécialité: Robotique

Soutenue le 28 Janvier 2021 devant un jury composé de :

Présidente du jury	DR. Agnès ROBY-BRAMI	INSERM
Directeur de thèse	Prof. Samer MOHAMMED	Université de Paris-Est Créteil
	Prof. Mohamad KHALIL	Université Libanaise
Co-encadrant de thèse	MCF. Vincent BONNET	Université de Paris-Est Créteil
Rapporteur	Prof. Bruno WATIER	Université de Toulouse
	DR. Vincent PADOIS	INRIA Bordeaux
Examinatrice	Prof. Sandy RIHANA	Université Saint Esprit Kaslik

I would like to dedicate this thesis to my loving family …

Acknowledgements

First of all, I would like to express my deepest gratitude to my advisor, Samer MOHAMMED, and co-advisor, Vincent BONNET, for their persistent guidance and the enormous support and effort put in my supervision throughout this research work. Without their helpful advice and in-depth knowledge in the field, the completion of this thesis would not be possible.

I am grateful to my second advisor, Mohamad Khalil, who, despite the physical distance between France and Lebanon, always encouraged me, showed great confidence in me and helped me completing my administrative works.

I would also like to express my sincere gratitude to all my collaborators and co-authors, specifically Gentiane VENTURE to provide me with the opportunity to be a visitor student at Tokyo University of Agriculture and Technology, Japan and for making time to meet and provide valuable feedback and comments on my research. I am also deeply indebted to Raphael DUMAS for sharing his experience and detailed advice on my contributions.

I would like to thank all the jury members for reviewing this thesis and giving their valuable and constructive suggestions and comments: Agnès ROBY-BRAMI, Vincent PADOIS, Bruno WATIER, and Sandy RIHANA.

I thank all members and friends of the LISSI lab, Lebanese University, and GVlab. It has been a great experience knowing and working with all of you.

Finally, I am incredibly grateful to my family, who have always supported and encouraged me through all the life challenges during my PhD.

Abstract

Quantifying human motor act starts with measuring and estimating kinematics and dynamics variables as accurately as possible. Monitoring human motion has a wide array of applications in functional rehabilitation, orthopaedics, sports, assistive robotics or industrial ergonomics. Today's motion capture systems usually refer to stereophotogrammetric systems and laboratory-grade force-plate that are accurate but also costly, require expert skills, and are not portable. Recently, the use of affordable sensors for human motion estimation, such as Inertial Measurement Unit or RGB-Depth camera(s), has been the subject of numerous studies. Despite their great potential to be used outside of the laboratory, these systems still suffer from limited accuracy, mainly due to inherent IMU drift and visual occlusions, and the joint kinematics and kinetics estimates are still difficult to be estimated. These drawbacks might explain why such systems are rarely used in common clinical applications or for in-home rehabilitation programs. In this context, this thesis deals with the development of a new affordable motion capture system capable of estimating accurately human 3D joint state. Unlike previous studies based on either visual or inertial sensors, the proposed approach consists in combining data from newly designed visual-inertial sensors. The system is also making use of new practical calibration methods, which do not require any external equipment while remaining very affordable. All sensors data are fused into a constrained extended Kalman filter that takes advantage of the biomechanics of the human body and of the investigated tasks to improve significantly joint state estimate. This is done by incorporating different types of constraints, such as joint limits, rigid-body and soft joint constraints, as well as modelling the temporal evolution of joint trajectories and/or sensors random bias. The system's ability to estimate accurate 3D joint kinematics has been validated through various case studies of daily life activities for upper-arm and treadmill gait. Two different prototypes with different sensors count and configurations have been investigated. Experiments conducted with several healthy subjects showed very satisfactory results when compared to a gold standard motion capture system. Overall, the average RMS difference between the two systems was below 4deg. This was also the case when a reduced number of sensors was used for gait analysis. This system was also used for the dynamics identification of a

lower-limbs human-exoskeleton system. As a result, an error below 6% was observed when comparing estimated and measured external ground reaction force and moments. Finally, beyond these validations, a dynamics assessment framework has been proposed with the aim of selecting an optimal human-exoskeleton dynamic model that is the best trade-off between the accuracy of kinetic estimation, i.e., joint torque, and simplicity of modelling. To this end, the proposed framework consists in quantifying the independent contribution of kinematic and body segments inertial parameters to joint torque estimation, as well as the effect of wearer-exoskeleton joint axes misalignment. It has been exemplified in the case of an assistive knee joint orthosis during standardized sitting knee flexion/extension movements. Results led to a minimal orthosis-wearer model that was able to reconstruct up to 97.5% of the total knee joint torque estimate.

Keywords: Human motion capture, affordable sensors, adaptive filter, biomechanics, assisted rehabilitation, exoskeletons, dynamics identification.

Résumé

La quantification des activités motrices humaines nécessite de mesurer et estimer, aussi précisément que possible, des variables cinématiques et dynamiques. L'analyse du mouvement humain possède une grande variété d'applications dans les domaines de la rééducation fonctionnelle, l'orthopédie, le sport, la robotique d'assistance, ou l'ergonomie industrielle. Les systèmes d'analyse de mouvement actuels font généralement référence à des systèmes stéréophotogrammétriques et à des plateformes de force de laboratoire qui sont précis mais également coûteux, nécessitant des compétences d'experts et ne sont pas portables. Récemment, l'utilisation de capteurs à bas coût pour l'estimation du mouvement humain, tels que les centrales inertielles et les caméras RGB, a fait l'objet de nombreuses études. Malgré leur grand potentiel d'utilisation en dehors du laboratoire, ces systèmes souffrent encore d'une précision limitée, principalement en raison de la dérive inhérente des centrales inertielles et des occlusions en cas de l'utilisation des caméras, ce qui fait que l'estimation précise de la cinématique et de la dynamique articulaire est encore difficile à garantir. Ces restrictions pourraient expliquer pourquoi de tels systèmes sont rarement utilisés dans des applications cliniques ou pour la rééducation à domicile. Dans ce contexte, cette thèse a pour objectif le développement d'un nouveau système d'analyse de mouvement à bas coût permettant l'estimation précise de l'état 3D des articulations humaines. Contrairement aux études précédentes basées sur des capteurs soient visuels soient inertiels, l'approche proposée porte sur la combinaison des données de capteurs visuels-inertiels nouvellement conçus. Le système utilise également de nouvelles méthodes pratiques de calibration ne nécessitant aucun équipement externe. Les données des capteurs sont combinées dans un filtre de Kalman étendu contraint prenant en considération la biomécanique du corps humain ainsi que les tâches réalisées pour améliorer l'estimation de la cinématique. Cela se fait en incorporant des contraintes de corps rigide, des butées articulaires, et en modélisant l'évolution temporelle des trajectoires articulaires ou de la dérive des centrales inertielles. La capacité du système à estimer la cinématique articulaire en 3D a été validée par l'analyse de plusieurs activités de la vie quotidienne du bras ainsi que l'analyse de la marche sur tapis roulant. Deux prototypes avec un nombre et des configurations de capteurs différents ont

été étudiés. Les expériences menées avec plusieurs sujets sains ont montré des résultats très satisfaisants par rapport à un système stéréophotogrammétrique de référence. Dans l'ensemble, l'erreur quadratique moyenne obtenue est inférieure à 4 degrés. Ce système a également été utilisé pour l'identification des paramètres dynamiques des membres inférieurs d'un système humain-exosquelette. Un système d'évaluation a été proposé dans le but de sélectionner un modèle dynamique optimal du système humain-exosquelette qui soit le meilleur compromis entre la précision des couples articulaires estimés et la simplicité du modèle. Dans ce contexte, le système proposé vise à quantifier la contribution indépendante des paramètres cinématiques et dynamiques dans l'estimation du couple articulaire, ainsi que l'effet du mouvement relatif entre les axes articulaires de l'exosquelette et du porteur. Une évaluation a été réalisée sur une orthèse d'assistance de genou pendant des mouvements de flexion/extension. Les résultats ont conduit à la proposition d'un modèle minimal du système humain-orthèse.

Mots clés: Analyse du mouvement humain, capteurs à bas coût, filtre adaptif, biomécanique, rééducation assistée, exosquelette, identification des paramètres dynamiques.

Nomenclature

Acronyms/Abbreviations

AC Acromion

ADL Activities of Daily Living

AoR Axis of Rotation

AR Augmented Reality

ASIS Antero Superior Illiac Spine

AT Anthropometric Tables

BSIP Body Segment Inertial Parameter

CA Constant Acceleration

CAD Computer Aided Design

CC Pearson Correlation Coefficient

CEKF Constrained Extended Kalman Filter

CLAV Clavicle

CoM Center of Mass

CoR Center of Rotation

DoF Degrees-of-Freedom

EKF Extended Kalman Filter

FS Fourier Series

GDI Gait Deviation Index

GRFM Ground Reaction Forces and Moments

HJC Hip Joint Center

IMU Inertial Measurement Unit

JSC Joint Soft Constraint

LFE Lateral Femoral Epicondyle

LHE Lateral Humerus Epicondyle

LM Lateral Malleolus

MCS Motion Capture System

MFE Medial Femoral Epicondyle

MFT Modified Frenchay Test

MHE Medial Humerus Epicondyle

MKO Multi-Body Kinematic Optimization

MM Medial Malleolus

NRMSD Normalized Root Mean Square Difference

PSIS Postero-Superior Illiac Spine

QP Quadratic Programming

RMSD Root Mean Square Difference

RoM Range of Motion

RS Radial Styloid

SARA Symmetrical Axis of Rotation Approach

SCoRE Symmetrical Center of Rotation Estimation

SS Stereophotogrammetric System

STA Soft Tissue Artifacts

UKF Unscented Kalman Filter

US Ulnar Styloid

VIMU Visual Inertial Measurement Unit

WBB Wii Balance Board

ZUPT Zero Velocity Update

Kinematic Modelling Notations

Notation	*Description*
R_0	Global reference frame
$\boldsymbol{\theta}, \dot{\boldsymbol{\theta}}, \ddot{\boldsymbol{\theta}},$	Joint positions, velocities and accelerations vectors
$\mathbf{L}$	Segment lengths vector
N_J, N_L, N_F, N_S	Number of joints, segments, frames, and sensors
$\mathbf{R}_i^j$	Rotation matrix of frame R_i w.r.t. frame R_j
$\mathbf{r}_i^j$	position vector connecting both R_i and R_j frames origins w.r.t. R_j
$\mathbf{P}_i^j = (\mathbf{r}_i^j, \mathbf{R}_i^j)$	3D pose defining frame R_i w.r.t. R_j
$\mathbf{p}$	3D position of a point
P	Arbitrary point
$\mathbf{J}$	Kinematic Jacobian matrix
$\boldsymbol{a}_s^s, \boldsymbol{\Omega}_s^s$	Measured linear acceleration, angular velocity of the sensor expressed in the sensor's local frame
$\mathbf{q}_s^0$	quaternion representing the sensor measured 3D orientation w.r.t. R_0
$(\mathbf{r}_s^l, \mathbf{R}_s^l)$	sensor-to-segment local pose
$(\mathbf{r}_{m_i}^{m_j}, \mathbf{R}_{m_i}^{m_j})$	marker i to marker j local pose

Dynamic Identification Notations

Notation	*Description*
$\mathbf{W}_H, \mathbf{W}_E, \mathbf{W}_{HE},$	Regressor matrices for the human, the exoskeleton, and the human-exoskeleton systems
$\mathbf{\Phi}_H, \mathbf{\Phi}_E, \mathbf{\Phi}_{HE},$	Standard inertial parameters vectors of the human, the exoskeleton, and the human-exoskeleton systems
$\mathbf{\Gamma}, \bar{\mathbf{F}}$	Joint torques and external wrenches vectors
M_i	Mass of a segment i
MSX_i, MSY_i, MSZ_i	Components of the first moment of inertia of a segment i along X, Y, and Z-axes
$\mathbf{I}_i$	(3×3) inertia tensor of a segment i

Extended Kalman Filter Notations

Notation	*Description*
f, h	Process and measurement models
$\mathbf{x}, \mathbf{P}$	State vector and covariance matrix
$\mathbf{y}, \mathbf{S}$	Measurement vector and covariance matrix
N_X, N_Y	State and measurement vectors dimensions
$\mathbf{F}, \mathbf{H}$	Process and measurement models Jacobian matrices
$\mathbf{v}$	Vector of measurement innovation
$\mathbf{Q}, \mathbf{R}$	Process and measurement noise covariance matrices
$\mathbf{K}(\mathbf{K}^c)$	Kalman gain (constrained gain)
$\mathbf{d}$	Vector of joints feasible RoM constraints
$\mathbf{X}^-, \mathbf{X}^+$	Upper and lower bounds of the state vector
$\mathbf{I_d}$	Identity matrix
$\mathbf{b_a}$	(3×1) acceleration bias vector
$\mathbf{a}_i, \mathbf{b}_i$	Fourier coefficients referring to the modelling of joint i
N_H, ω	Number of harmonics, movement frequency
$\mathbf{Q}_{FS}$	Process noise covariance matrices in case of a Fourier-series-based model
$\theta_{i_{sc}}$, θ_{i_M}	Soft constraint and constant mean value associated with θ_i
$\boldsymbol{\theta}_{SS}$	Joint angles vector calculated based on SS

Table of contents

Chapter 1

General Introduction

This chapter contains a general introduction to the research work described in this thesis. An overview of the proposed research motivation and key challenges, as well as the main goals, contributions, and outline of this thesis, are presented.

1.1 Motivation

Analyzing and understanding human motion has been a challenging and fascinating research field for decades due to its high interdisciplinary nature and wide range of applications. Among these applications, those related to the biomedical field appear the most prospective and promising due to growing population numbers and ages, as well as the increased prevalence of neurological conditions worldwide. A recent survey from the United Nations shows that one of six people in the world will be aged 65 and over by 2050, an increase up to more than double compared to 2019 [1]. Neurological injuries such as stroke, spinal cord injuries, and musculoskeletal weaknesses are frequent causes of motor disability worldwide, especially in the elderly population with the highest incidence [2]. Among 795,000 stroke survivors in the United States in 2015, 26% were disabled in fundamental Activities of Daily Living (ADL), and 50% experienced reduced mobility due to hemiparesis, thus needing direct assistance [2].

Assistance and care for such disabilities are usually provided by clinicians and experts in neurological pathologies, leading to substantial costs especially in case of long-term rehabilitation processes [2]. Currently, most of the rehabilitation services commonly use coventional manual hands-on treatment [3]. Moreover, to assess the clinical progress through the rehabilitation process, patients performances are usually evaluated based on subjective and momentary metrics, such as timing procedures and clinicians subjective observations. However, such metrics might be biased and thus, influence the effectiveness and rate of

patients long-term recovery [4]. The current challenges include the development of new efficient solutions to optimize existing rehabilitation processes, improve patients quality of life, while ensuring future sustainability of world healthcare services and/or reduction of the associated costs. This suggests to be able to measure, monitor, and improve patients performances, prevent or provide an early disease diagnosis, ensure a certain degree of patient's dependency to pursue their recovery at home. Particularly, the use of human motion analysis technologies for quantitative assessment of patients motion, as well as robotic assistive devices for motion assistance and rehabilitation, are promising solutions to support clinical decision-making and lead to a more effective and a faster rehabilitation process.

Laboratory-based optical Motion Capture Systems (MCSs) are traditionally used to measure human motion. Although being accurate, their relatively high costs, complex setup, and lack of portability are important limitations that restrict their widespread use, particularly in daily clinical practice. At the same time, analyzing human motion outside laboratory-controlled settings may add several further challenges, such as uncertainties about the environment, as well as limitations of sensors and equipment that can be used. Recent advances in wearable and vision-based sensing technologies have created new opportunities for capturing human motion in different challenging settings. Commercial sensors, such as Inertial Measurement Units (IMUs) and RGB/RGB-D cameras, are nowadays available and have been tested in several applications [5–9]. Despite their potential benefits, their accuracy, reliability, and usability remain a challenging aspect. As a consequence, there is still much room for improving human motion analysis using affordable and portable MCSs.

Recently, robotic assistive devices, such as powered exoskeletons and orthoses, have witnessed significant development at both software and hardware levels [10]. Exoskeletons are wearable robots that can be used to assist patients suffering from neurological and age-related motor impairments in achieving their basic ADL, as well as during rehabilitation exercise training [10]. Allowing to achieve repetitive, accurate, oriented, and long-intensive exercises, exoskeleton-assisted training shows several advantages over conventional and manual training. Indeed, exoskeletons allow improving the performance of rehabilitation training while reducing considerably the workload of therapists. They also incorporate wearable sensors that can provide quantitative measurements for an objective and repeatable diagnosis [3]. During the last decade, various research and commercial prototypes of upper- and lower-limbs exoskeletons have been developed with great potential to enhance the wearer's mobility and rehabilitation performances [10, 11].

Among open challenges of current exoskeleton prototypes, safety and ergonomic features are of critical concern. Indeed, to not hinder the wearer's natural pattern and comfort while moving, exoskeletons must be in complete symbiosis with the body anatomy. At the same

time, exoskeletons should keep ergonomic features, such as being light-weight, as well as being comfortable and accepted by the user, e.g., ease of donning and doffing of the exoskeleton [3]. In practice, however, the human body complex anatomy and its inter- and intra- wearers variability make challenging to align finely exoskeleton and wearer's axes of rotation [12]. As a result, inevitable misalignment occurs between the two axes [13]. Assessing the effect of this misalignment is therefore of crucial importance to improve robotic-assisted rehabilitation. Moreover, due to the complexity and non-linear nature of exoskeleton/wearer interactions, model-based controllers, that take into account both kinematic and dynamic parameters of the wearer/exoskeleton, should be developed to ensure a smooth control of the exoskeleton [14]. To this end, an accurate and efficient identification method of human-exoskeleton systems would help toward the development of assistive exoskeletons.

1.2 Thesis Contributions and Outline

Given the above considerations, the foremost goal of this thesis is to develop and validate an affordable, portable, user-friendly, and accurate human MCS capable of providing direct 3D joint kinematics estimates of different ADL movements.

This common goal has been primarily driven by the following scientific premises:

- **P1.** Accurate joint kinematics are of great importance to support quantitatively clinical diagnosis. Based on such data, quantitative indicators may be developed and used to automatically assess patients movement.
- **P2.** For applications taking place outside of the lab, such as clinical applications, such data must be measured using cost-effective, transportable, and light-weight sensors.
- **P3.** To improve the MCS usability, reducing the number of sensors being utilized is of great interest.
- **P4.** To ensure a smooth control and a robust performance of an assistive exoskeleton, accurate exoskeleton-wearer modelling is required, which primarily relies on the accurate knowledge of the exoskeleton/wearer kinematic and dynamic parameters.
- **P5.** An optimal exoskeleton-wearer dynamic model, that is the best trade-off between accuracy and simplicity of modelling, needs to be generated, in particular for real-time

applications.

Accordingly, the main contributions of this thesis are summarized as follows and have resulted in a number of scientific publications (see List of Publications):

- **C1.** Develop an affordable visual-inertial MCS combining the above-mentioned features and perform its experimental validation for upper-limbs joint kinematics estimation during daily rehabilitation tasks of the Modified Frenchay test (MFT), i.e., clinical index for arm mobility assessment of post-stroke patients (see section 4.1.1) [15, 16].
- **C2.** Evaluate the proposed MCS for full gait kinematics estimation using a reduced number of sensors. [17].
- **C3.** Perform affordable dynamic identification of a human-exoskeleton system based on the proposed MCS. [18]
- **C4.** Develop a new framework for dynamics assessment and optimal model selection of a human-knee joint orthosis system. It consists in quantifying wearers-orthosis knee joint axes misalignment along with a sensitivity analysis of kinematic and dynamic parameters contribution to knee joint torque estimation.
  [19].

The remaining of this thesis is outlined as follows:
Chapter 2 reviews the state-of-the-art settling the basis of the research work described in the following chapters. It overviews various disciplines and applications for analyzing human motion. It also introduces the fundamental biomechanical concepts and quantities used to describe a human/robot motion, as well as the latest and common technologies used to measure these quantities and their limitations. Finally, a brief literature review of various tracking and identification algorithms used to study human/robot movement based on different sensors configurations is provided. Limitations of these algorithms and the way they are addressed in our proposed research are also presented.

Chapter 3 is a brief introduction to the fundamental theoretical foundations used in the following chapters. It introduces a new MCS framework based on a Constrained Extended Kalman Filter (CEKF) fusing affordable data from visual and inertial sensors, and on a

biomechanical model of the human body. A practical calibration method is proposed and used to calibrate the affordable sensors and the biomechanical model being investigated. A dynamic identification pipeline for Body Segments Inertial Parameters (BSIPs) estimation is also developed.

Chapter 4 develops two case studies of the proposed MCS framework under different implementations. First, upper-limbs joint kinematics are estimated during daily rehabilitation tasks motivated by those performed in clinical settings.Second, gait kinematics are estimated using a reduced sensors-count configuration. In both studies, the resulting kinematics are validated w.r.t. those obtained using a gold standard Stereophotogrammetric System (SS).

In chapter 5, we analyze human-robot calibration and identification in two cases studies. First, a practical identification pipeline to estimate the dynamics of a human subject wearing a full lower-limbs exoskeleton is proposed. In a second study, a dynamic assessment framework is developed based on reference kinematic measurements. It aims at assessing modelling inaccuracies, including human-robot joint axes misalignment, as well as relevant kinematic and dynamic parameters, which contribute to the best trade-off between accuracy and simplicity of the human-robot modelling. The proposed framework has been exemplified in the case of a human-orthosis system where the wearer performs knee joint flexion/extension movements.

Finally, chapter 6 summarizes the findings of the previous chapters, along with directions for future research.

Chapter 2

Human Motion Analysis: State of the Art

Understanding the biomechanics, i.e., kinematics and dynamics, through human motion analysis has been a subject of interest in numerous fields with a wide array of applications. Within the specific area of biomechanics, examples of various human motion analysis applications are described in section 2.1.

This chapter explores the state of the art of biomechanical analysis with a focus on human/robot kinematic analysis and dynamic identification using tools for human body biomechanical modelling (section 2.2). Input measurements for this analysis can be derived from data collected by various MCSs that are presented in section 2.3, along with their advantages and limitations. Section 2.4 provides a brief literature review of sensors configurations, algorithms, as well as their abilities and limitations to measure human body kinematics and to identify human/robot BSIPs. Finally, human-robot physical interaction, as well as the disparities between human and robot biomechanics, are discussed in section 2.5.

2.1 Why to Analyze Human Motion ?

Applications for human motion analysis are very diverse and highly interdisciplinary (see Fig. 2.1). Among these, the current thesis focuses on biomechanical applications in general and those related to ADL and/or rehabilitation in particular. Biomechanical applications can be classified under two main objectives that are discussed below [20]: preventing and/or treating injuries, such as medical and ergonomic applications, and enhancing human motion performance, such as sports applications.

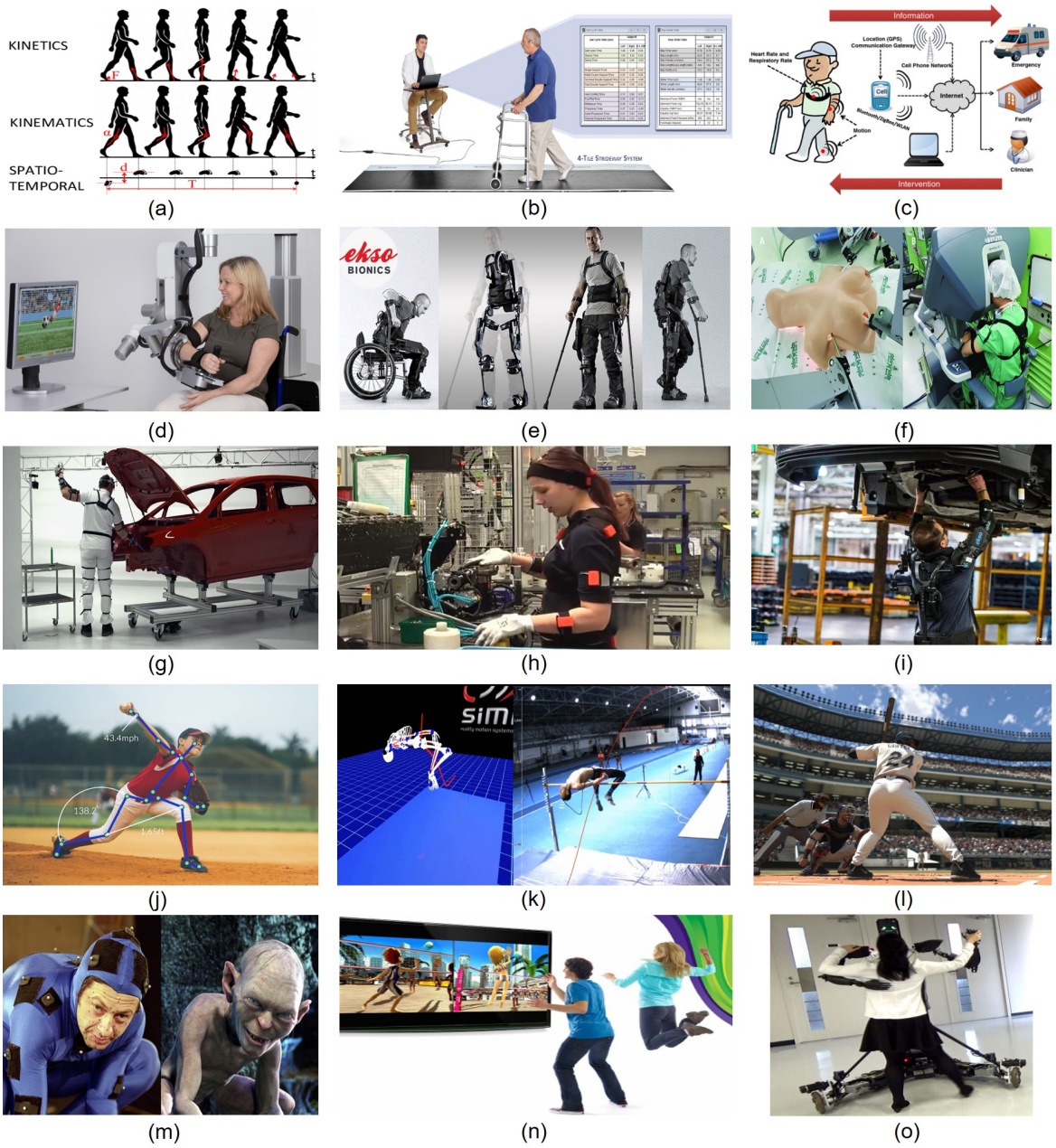

Fig. 2.1 Applications of human motion analysis are very diverse and highly interdisciplinary. (a[1], b[2], c [21]) Rehabilitation and elderly healthcare, (d[4], e[5]) Robot-assisted rehabilitation, (f) Surgical training [22], (g[6], h[7], i[8]) Industrial ergonomics, (j[9], k[10]) Sports analysis, (l[11], m[12], n[13], o[14]) Animation and entertainment.

[1] A. Sant'Anna & N. Wickström, "Symbolic Approach to Motion Analysis: Framework and Gait Analysis Case Studies", 2013

[2] https://www.tekscan.com/blog/medical/why-gait-analysis-important

[4] https://fitness-gaming.com/news/health-and-rehab/armeo-power-robotic-training.html

[5] https://exoskeletonreport.com/2015/04/12-commercial-exoskeletons-in-2015

[6] https://www.youtube.com/watch?v=lIm8MwFpqvY

Human motion analysis has great potential in several medical applications, including diagnosis of movement disorders, therapy assessment, and rehabilitation [23]. By quantifying individuals' movements, physical therapists can better characterize normal and pathological motion [24, 25]. Information such as joint trajectories may be assessed such that they allow identifying motor impairments, evaluating their degrees, and guiding the best treatment that addresses a patient's individual needs. They can also be used to examine subtle and continuous changes in a patient's motor state, the consequences of different therapies, thus develop more effective plans that help patients recover their motor abilities while reducing the time of the rehabilitation process [26]. For instance, gait analysis has been extensively studied as one of the most essential ADL for a better quality of life of individuals [27]. Gait kinematics and kinetics have been assessed in both healthy [28–32] and patients suffering from motor deficiencies [33–35].

As the motion capture technology has witnessed significant development in terms of cost and size reduction, simplicity, and artificial intelligence, new medical applications have been investigated, such as preventive medicine, e.g, sport medicine [36] (see Fig. 2.1.j, k) and occupational health [37] (see Fig. 2.1.g-i), interactive rehabilitation by means of robotics and/or virtual reality [38] (see Fig. 2.1.d, e), as well as training of medical professionals [22] (see Fig. 2.1.f). With the specific aim of preventive interventions, researchers used motion capture data in machine learning algorithms to detect fall events in elders [39, 40]. A promising system for detecting and classifying more complex movements such as walking, running, sitting, and falling using multi-body worn sensors was proposed by Ugolotti et al. [41]. Other studies have extended early diagnoses to the tracking of patients' movements at home and in real life scenarios [8], i.e. home/remote rehabilitation, which allows reducing the healthcare cost. In this context, affordable and transportable technologies, such as Kinect and/or wearable IMUs sensors, have emerged and have been widely investigated for applications of human motion analysis [6–8, 42–46]. To support home rehabilitation, some studies have further used motion capture data to reconstruct patients' 3D movements and

[7]https://www.youtube.com/watch?v=obQCSjYAZok

[8]https://www.cnet.com/roadshow/news/fords-exoskeleton-could-help-factory-workers-in-a-big-way

[9]https://www.sporttechie.com/chicago-cubs-leverage-big-data-motion-capture-technology-in-2016-run

[10]https://www.youtube.com/watch?v=rctWLp8KDgc

[11]https://www.polygon.com/2017/1/27/14414534/mlb-the-show-17-trailer-griffey-motion-capture

[12]L. Karreman, "The Motion Capture Imaginary: Digital renderings of dance knowledge", 2017.

[13]T. BERG, et al., "Interactive music: Human motion initiated music generation using skeletal tracking by kinect", *Proc. Conf. Soc. Electro-Acoustic Music*, United States, 2012.

[14]D. Granados, et al., "Dance teaching by a robot: Combining cognitive and physical human–robot interaction for supporting the skill learning process", IEEE Robotics and Automation Letters, vol. 2, no 3, p. 1452-1459, 2017.

provide a visual feedback on how rehabilitation exercises should be correctly performed [47]. The motion capture technology has also supported the development of robotic devices, such as exoskeletons, for motion assistance and rehabilitation [6]. During the last decades, assistive exoskeletons have emerged as a powerful tool to help patients recover their motor abilities and achieve their daily life activities [10]. Based on embedded sensors, e.g., encoders or IMUs, exoskeletons can estimate the limb movement, thus provide accurate and appropriate assistance to the wearer [48].

Despite the great advantages and the variety of applications of human motion analysis, medical applications tend to be limited to research laboratories due to the limited accuracy and/or challenges of using the available MCSs in the clinical practice, i.e., expensive, hardware-complex and/or non-portable systems.

Another human motion analysis application is for industrial ergonomics. Within factories, employees often have to perform tasks that require complex movements during extended hours, which may yield long-term musculoskeletal disorders. Assessing employees movements is thus of great importance. Previous methods, such as using visual observations, are highly subjective and error-prone. Recently, motion capture technology has been introduced as an accurate tool for quantifying and reconstructing employees' 3D movements in industrial ergonomics at the aim of preventing work-related musculoskeletal disorders [49, 50] (see Fig. 2.1.g, h). Based on such information, robotic devices such as occupational exoskeletons have been developed to assist employees in completing their tasks [51]. For instance, as shown in Fig. 2.1.i, an upper-limbs exoskeleton has been used at Ford Motor company to support employees during overhead automotive assembly tasks [52].

Besides rehabilitation and injury prevention, sports analysis is of great advantage in performance enhancement [36] (see Fig. 2.1.j, k). For instance, Dai et al. [53], studied the effect of landing techniques on knee load and performance during stop-jump and side-cutting tasks. Doing so, they figured out that a soft landing with greater knee flexion reduces the risk of knee injury but at the same time decreases the performance through larger stance time and mechanical work and reduced jump height and movement speed. Similarly, Sinclair and Bottom [54] suggested that females present a greater risk of knee injuries during the fencing lunge. With the aim of competitive performance, several studies have characterized a tennis optimal serve [55–58]. Further examples of sport analysis applications using motion capture technology may be found in the survey of Pueo et al. [36]. Nevertheless, an important challenge in sport analysis is to select the appropriate MCS [59]. Indeed, within sports applications, accurate measurements must usually be recorded at a relatively high sampling

rate. Furthermore, some applications may require to be used outdoor. For further details, MCSs that are currently available in the literature are discussed in section 2.3.

2.2 Biomechanics for Analyzing Human Motion

The term *biomechanics* refers to *bio*, indicating life and *mechanics*, the study of motion and forces resulting in/from it. It was used during the early 1970s as the science investigating the mechanical aspects of living organisms, including the human body [60]. In different terms, biomechanists analyze anatomical and functional aspects of the human body using tools of mechanics [61].

Biomechanical analysis is divided into kinematics and kinetics. To analyze human body kinematics is to describe the appearance of the body segments movement, including considerations of space and time [61]. Kinematics attempt answering questions such as how far, how fast, and how quickly is a body moving, i.e., distance, displacement, velocity, acceleration, whereas kinetics study the forces due to which the movement occurred. These may be assessed either qualitatively or quantitatively along with a biomechanical model used to describe the human body movement. For this purpose, the human body is usually simplified as a set of rigid segments, i.e., links, articulated with joints. An example of biomechanical analysis is to assess human joint kinematics, i.e., knee joint position, velocity, or acceleration during gait, and kinetics, i.e., knee joint torque (see Fig. 2.2).

The goal of this section is to introduce the biomechanical bases used to quantify human motion. Section 2.2.1 emphasizes the relevance of human motion quantitative analysis. Section 2.2.2 details the systematic procedure used to develop a human body biomechanical model.

2.2.1 Quantitative versus Qualitative Analysis

Analyzing human motion may be either qualitative or quantitative. Qualitative analysis means non-numerical. It describes the movement as it is visually observed. Whereas, quantitative analysis involves data measurements obtained using specific tools and equipment. For example, we might qualitatively state that the patient is unable to fully extend his elbow, his movement is slow, unsmooth, and insufficient to complete the phases of a given a task. However, such observations lack objectivity and are largely subject to intra-personal evaluation. Furthermore, they do not take into consideration subtle changes in the individual's motor state, which may vary considerably and continuously with time [4]. On the other hand, using a motion capture system, the movement may be reconstructed in 3D while providing

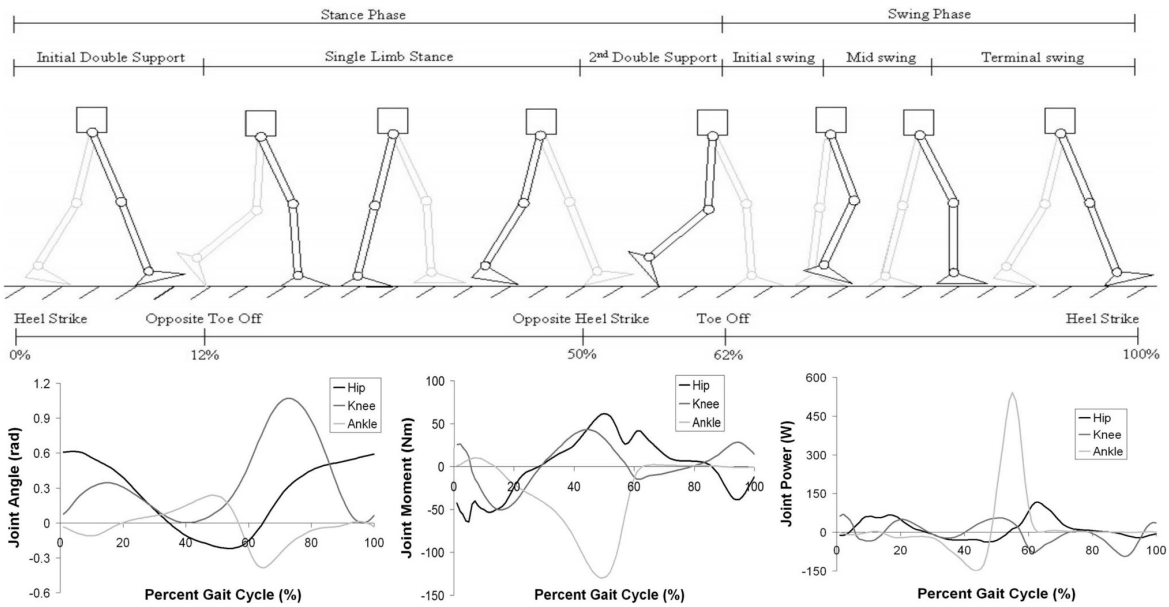

Fig. 2.2 Example of human gait kinematics and kinetics quantitative analysis [28].

measurements related to the patient motion at each instant and phase of the performed task, i.e., Range of Motion (RoM), timing, position, speed, muscles contribution, joint forces and moments. Such information would be of crucial importance to help clinicians and trainers develop their diagnosis.

The quantification of human physical activities may be of significant relevance in several applications, as discussed in section 2.1. Nevertheless, within quantitative measurements, careful attention must be given to the quantities to be measured, the appropriate MCSs to be used, as well as the validity and reliability of the measured data.

In this thesis, we focus on kinematics and kinetics quantitative assessment associated with a biomechanical model of the human body.

2.2.2 Biomechanical Modelling of the Human Body

The groundwork of human motion quantitative analysis is often a biomechanical model of the human body. A biomechanical model is used to provide a realistic and straightforward representation of the human body skeletal structure. It allows describing the motor coordination and the functional performance of the human locomotor system [62].

The human body is usually described as a system of multi-bones segments linked with joints, i.e., multi-body model. Every joint consists of a number of Degrees-of-Freedoms (DoFs) indicating in how many different directions it can move. In general, the human body

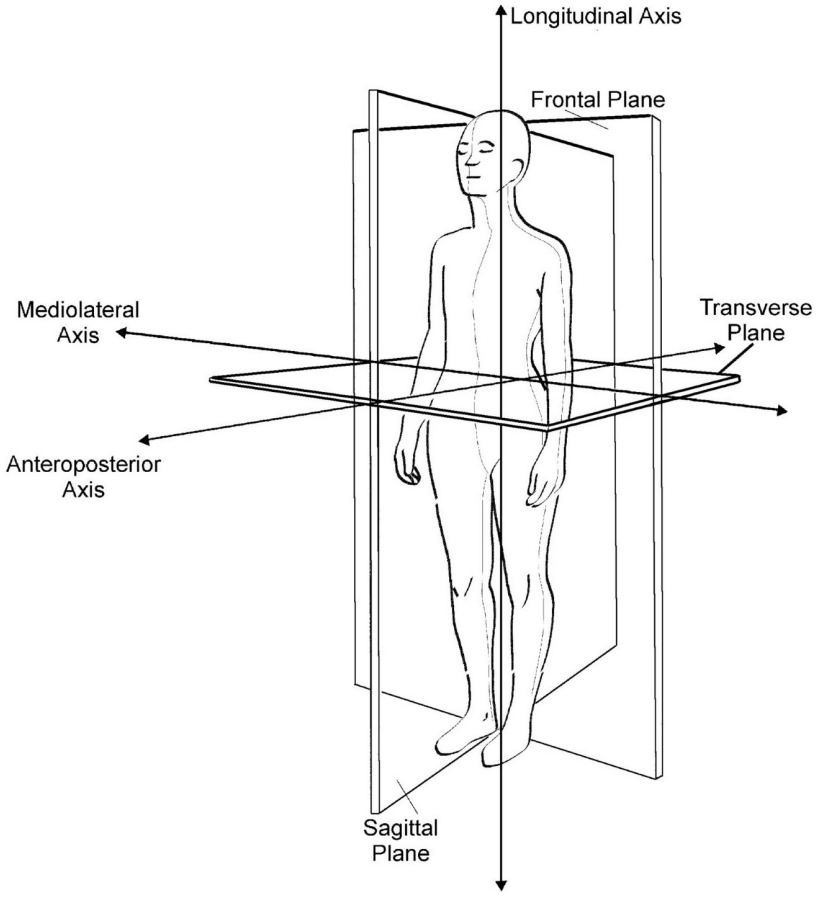

Fig. 2.3 The major anatomical planes of human motion, and axes of rotation [20].

moves within three anatomical planes that are defined in Fig. 2.3: frontal, sagittal, and transverse.

It might be very complex to represent the human body skeletal system in practice. According to Zatsiorsky [63], it is composed of 148 moving bones segments connected by 147 joints, which suggests a total of 244 DoFs. Thus, it is common in the literature to simplify the human body skeleton to the most relevant segments and joints. Usually, most of the biomechanical models describe the human body as a one or several kinematic chains of rigid bodies, representing bones segments, linked by mechanical joints.

Mechanical joints are either prismatic or revolute, referring to 1 DoF translational or rotational movement, respectively. Thus, most of the human body joints are described as a combination of prismatic and revolute joints, i.e., complex joints, with zero-length zero-mass segments. A complex joint may combine up to six DoFs, i.e., three prismatic and three revolute joints, describing all the possible relative movements between two adjacent segments. However, a biomechanical model is usually kinematically constrained to ensure realistic

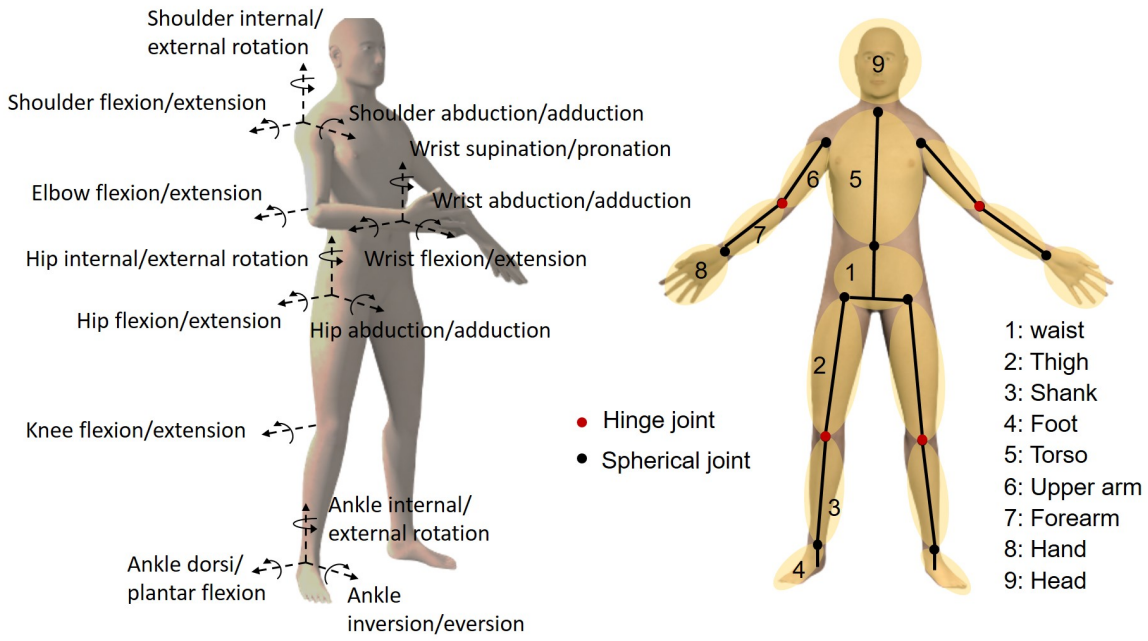

Fig. 2.4 The human body biomechanical model composed of multi-rigid segments articulated with joints.

motions of the human body. An example of kinematic constraints is to assume the knee joint as a single DoF revolute joint, i.e., hinge joint, performing rotation in the sagittal plane with a given RoM.

2.2.2.1 Human Body Kinematics Modelling

There are two types of kinematic parameters: global, such as spatio-temporal parameters, and local, such as joint trajectories. The latter may be assessed in 3D and may be either linear or angular, i.e., linear/angular position, velocity, and acceleration. An angular position refers to the orientation of a segment anatomical frame w.r.t. a global reference one. Whereas a joint angle is the relative orientation between two anatomical frames associated with two consecutive segments. In general, human body joint angles describe six basic rotations of body segments relative to each other. These rotations are generally referred to as flexion/extension, abduction/adduction, and internal/external, and occur in the sagittal, frontal, and transverse planes about the mediolateral, anteroposterior, and longitudinal axes, respectively (see Fig. 2.4.a) [64]. Note that flexion, abduction, and internal positive rotations follow the directions shown in Fig. 2.4.a. In the case of other joints, such as the pelvis, wrist, and ankle, these rotations may have different names. For instance, the ankle dorsi/plantar flexion and wrist

supination/pronation also refer to the rotations of these joints about the mediolateral and longitudinal axes, respectively.

A local anatomical frame, i.e., Cartesian coordinate system, is used to define each body segment. In the literature there are numerous ways to build a multi-body kinematics model. A multi-body Forward Kinematics Model (FKM) allows to calculate the Cartesian pose of segments anatomical frames as a function of joints angles and segment lengths. In contrast, an Inverse Kinematic Model (IKM) computes the joint angles that provide a particular Cartesian pose of the segments anatomical frames.

The Modified Denavit-Hartenverg Convention Because modelling of human body is dealing with rigid bodies and ideal mechanical joints, it is more and more common in the literature [65] to use robotics modelling tools, that were developed to be efficient in terms of calculation time for real-time applications, to compute kinematic and kinetic parameters of the human body. A classical and well-known robotics modelling tool, allowing to obtain the homogeneous transformation matrix between two consecutive frames, is the Modified Denavit Hartenberg (MDH) [66]. MDH representation is a systematic procedure with a minimal representation since it is based only on four descriptive parameters. However, the model frames require to follow certain rules that are given below:

1. A static global reference frame R_0 with axes X_0, Y_0, Z_0 is first assigned randomly. Usually R_0 is defined at the pelvis as a static base of the human body kinematic chain. However, in practice, the pelvis is a floating base which pose is described w.r.t. R_0, i.e., static laboratory frame. Thus, six additional DoFs describing the pelvis 3D pose must be added to the model. All body segments frames are defined w.r.t. R_0.

2. A frame R_i with axes X_i, Y_i, Z_i is assigned to the segment i such that:

   (a) Z_i is aligned with the motion axis of joint i.

   (b) X_i is aligned with the common perpendicular of both Z_i and Z_{i+1}, given that $i+1$ refers to the joint that is subsequent to joint i in the kinematic chain.

   (c) Y_i is established using the right-hand rule

A (4×4) transformation matrix defining the i^{th} segment's frame R_i relative to its adjacent R_{i-1} can then be calculated as a function of the four parameters given below [67]:

- α_i: the angle between Z_{i-1} and Z_i about X_{i-1}
- d_i: the distance between Z_{i-1} and Z_i along X_{i-1}

- θ_i: the angle between X_{i-1} and X_i about Z_i
- r_i: the distance between X_{i-1} and X_i along Z_i

such that:

$$\begin{aligned}\mathbf{T}_i^{i-1} &= \begin{bmatrix} & \mathbf{R}_i^{i-1} & & \mathbf{r}_i^{i-1} \\ 0 & 0 & 0 & 1 \end{bmatrix} = \mathbf{TR_x}(\alpha_i)\,\mathbf{Tr_x}(d_i)\,\mathbf{TR_z}(\theta_i)\mathbf{Tr_z}(r_i) \\ &= \begin{bmatrix} cos\theta_i & -sin\theta_i & 0 & d_i \\ cos\alpha_i sin\theta_i & cos\alpha_i cos\theta_i & -sin\alpha_i & -r_i sin\alpha_i \\ sin\alpha_i sin\theta_i & sin\alpha_i cos\theta_i & cos\alpha_i & r_i cos\alpha_i \\ 0 & 0 & 0 & 1 \end{bmatrix} \\ & \qquad\qquad i = 1,..,N_F \end{aligned} \tag{2.1}$$

where $\mathbf{R}_i^{i-1}(3\times3)$ is the rotation matrix going from frame R_{i-1} to frame R_i and $\mathbf{r}_i^{i-1}(3\times1)$ is the position vector connecting both frames origins. $\mathbf{TR_x}$ and $\mathbf{TR_z}$ are the (4×4) transformation matrices corresponding to a rotation about X and Z axes, respectively. $\mathbf{Tr_x}$ and $\mathbf{Tr_z}$ are the (4×4) transformation matrices corresponding to a translation along X and Z axes, respectively. The value of joint i is then evaluated as $\bar{\sigma}_i\theta_i + \sigma_i r_i$, where $\sigma_i = 1$ in case of a revolute joint and $\sigma_i = 0$ in case of a prismatic joint. In the following of this thesis, joint values will be denoted by θ in both cases to simplify notations.

The Forward Kinematics Model Using the MDH, the FKM can be obtained through a serial multiplication of transformation matrices (Eq. 2.1) starting from the global reference frame R_0 and performed over the entire segments' frames, as follows:

$$\begin{aligned} \mathbf{P}_i^0 &= FKM(\boldsymbol{\theta}, \mathbf{L}) \\ \text{such that} \quad \mathbf{T}_i^0 &= \mathbf{T}_p^0\mathbf{T}_i^p \\ & \qquad i = 1,..,N_F \end{aligned} \tag{2.2}$$

where $\mathbf{P}_i^0$ is the Cartesian pose, i.e., position and orientation, of frame R_i w.r.t. the global reference frame R_0. It is composed of (3×1) position vector $\mathbf{r}_i^0$ and of (3×3) rotation matrix $\mathbf{R}_i^0$ representing the frame 3D orientation in R_0. $\boldsymbol{\theta}(N_J\times1)$ is the vectors of all joints to be calculated in the next chapters and $\mathbf{L}(N_S\times1)$ the vector of all segments' lengths to be measured. N_J, N_S, and N_F denote the total number of joints, segments, and frames, respectively. p denotes the index of the segment that is antecedent to the current segment i in the kinematic chain being investigated. Notice that within serial chains $p = i-1$. However,

in parallel chains, such as the human body, p may be different. For instance, the left foot previous segment is the pelvis rather than the right foot.

The Cartesian velocity of a segment i expressed in the global reference frame is calculated using the FKM first derivative, as follows:

$$\begin{bmatrix} \mathbf{v}_i^0 \\ \mathbf{\Omega}_i^0 \end{bmatrix} = \mathbf{J}(\boldsymbol{\theta})\dot{\boldsymbol{\theta}} \tag{2.3}$$

where $[\mathbf{v}_i^0\ \mathbf{\Omega}_i^0]^T$ is composed of (3×1) linear and angular velocity vectors referring to segment i, respectively. $\dot{\boldsymbol{\theta}}$ refers to the $(N_J\times1)$ joints velocities vector and $\mathbf{J}$ is the $(6\times n)$ kinematic Jacobian matrix with n the number of DoFs used to describe the movement of segment i relative to R_0. A practical way for calculating $\mathbf{J}$ is given by the Eq. 2.4 below [66]:

$$\begin{aligned} \mathbf{J}(\boldsymbol{\theta}) = \begin{bmatrix} \mathbf{J_v} \\ \mathbf{J_\Omega} \end{bmatrix} = \begin{bmatrix} \sum_{j=1}^{n}[\sigma_j\mathbf{z}_j + \bar{\sigma}_j(\mathbf{z}_j\times\mathbf{L}_n^j)] \\ \sum_{j=1}^{n}\bar{\sigma}_j\mathbf{z}_j \end{bmatrix} \\ \mathbf{L}_n^j = \mathbf{r}_n^0 - \mathbf{r}_j^0 \\ \mathbf{z}_j = \mathbf{R}_j^0\,\mathbf{z}_j^j \end{aligned} \tag{2.4}$$

where $\mathbf{J_v}$ and $\mathbf{J_\Omega}$ are the $(3 \times n)$ Jacobian matrices referring to linear and angular velocities respectively. Given Eq. 2.1, $\mathbf{L}_n^j$ denotes the (3×1) position vector going from the origin of frame R_j to the one of frame R_n. $\mathbf{z}_j$ and $\mathbf{z}_j^j = [0\ 0\ 1]^T$ denote the (3×1) unit vectors along the Z-axis of frame R_j expressed in R_0 and R_j, respectively.

2.2.2.2 Human Body Dynamics Modelling

In general, the dynamic equations of motion of a kinematic chain are governed by its base and body segments kinematics, kinetics, and Body Segment Inertial Parameters (BSIPs). BSIPs, in 3D, consist of ten parameters to be identified per each body segment (see sections 2.4.3 and 3.3), as follows:

- Mass (1×1)
- Centre of Mass (CoM) 3D position vector (3×1)
- Inertia tensor (3×3): symmetric matrix with 6 independent parameters to be identified

All BSIPs of a segment i can be grouped into a vector $\mathbf{\Phi}_i(10\times1)$ to be identified, and are referred to as standard inertial parameters [68].

The inverse dynamic model provides the joint forces and torques as a function of the joint trajectories. Whereas the forward dynamic model allow to calculate the joint accelerations as a function of joint positions, velocities, torques, as well as external wrenches [67]. There are two main methods for representing the dynamic equations of a multi-body system: the Euler–Lagrange formulation, deriving the system energy as a whole, and the recursive Newton–Euler formulations, based on the equilibrium of the forces acting on each body segment. Although being equivalent, the latter involves no differentiation and is computationally more efficient so it can be easily implemented both numerically and symbolically.

The Newton-Euler method consists of two recursive calculations, forward and backward, for propagating the kinematics and dynamics quantities throughout a multi-body system. Starting from the reference coordinate system, the forward recursion computes the angular velocity, angular and linear acceleration of each segment based on those of its antecedent.

Thus, given $\boldsymbol{\theta}$, $\dot{\boldsymbol{\theta}}$, and $\ddot{\boldsymbol{\theta}}$ as the $(N_J \times 1)$ joint positions, velocities, and accelerations vectors, respectively, the angular velocity $\boldsymbol{\Omega}_j^j$ associated with a frame R_j is that of its antecedent expressed in R_j in addition to the new velocity added by joint j:

$$\begin{aligned} \boldsymbol{\Omega}_j^j &= \boldsymbol{\Omega}_{j-1}^j + \bar{\sigma}_j \, \dot{\boldsymbol{\theta}}_j \, \mathbf{z}_j^j \\ \boldsymbol{\Omega}_{j-1}^j &= \mathbf{R}_{j-1}^j \, \boldsymbol{\Omega}_{j-1}^{j-1} \\ j &= 1, .., N_F \end{aligned} \tag{2.5}$$

Similarly to Eq. 2.5, the linear velocity $\mathbf{v}_j^j$ can be calculated. By differentiating the equations of linear and angular velocities w.r.t. time, the angular and linear accelerations associated with frame R_j can be obtained respectively by the Eq. 2.6 and Eq. 2.7 below:

$$\dot{\boldsymbol{\Omega}}_j^j = \mathbf{R}_{j-1}^j \, \dot{\boldsymbol{\Omega}}_{j-1}^{j-1} + \bar{\sigma}_j \left(\ddot{\boldsymbol{\theta}}_j \, \mathbf{z}_j^j + \dot{\boldsymbol{\Omega}}_{j-1}^j \times \dot{\boldsymbol{\theta}}_j \, \mathbf{z}_j^j \right) \tag{2.6}$$

$$\dot{\boldsymbol{v}}_j^j = \mathbf{R}_{j-1}^j \left[\dot{\boldsymbol{v}}_{j-1}^{j-1} + \dot{\boldsymbol{\Omega}}_{j-1}^{j-1} \times \mathbf{L}_j^{j-1} + \boldsymbol{\Omega}_j^j \times \left(\boldsymbol{\Omega}_j^j \times \mathbf{L}_j^{j-1} \right) \right] + \sigma_j \left(\ddot{\boldsymbol{\theta}}_j \, \mathbf{z}_j^j + 2 \, \boldsymbol{\Omega}_{j-1}^j \times \dot{\boldsymbol{\theta}}_j \, \mathbf{z}_j^j \right) \tag{2.7}$$

In a second step, the backward recursion is performed throughout frames $R_{j=N_F}$ to $R_{j=1}$. It allows computing the forces and torques required to create a desired acceleration, obtained above, at a current joint j. First, the forces acting on a segment j are calculated as the sum of forces exerted on it by segment $j+1$ expressed in R_j as well as the external forces accelerating it, as follows:

$$\begin{aligned} \mathbf{f}_j^j &= \mathbf{F}_j^j + \mathbf{f}_{j+1}^j \\ \mathbf{f}_{j+1}^j &= \mathbf{R}_{j+1}^j \mathbf{f}_{j+1}^{j+1} \\ \mathbf{n}_j^j &= \mathbf{N}_j^j + \mathbf{R}_{j+1}^j \mathbf{n}_{j+1}^{j+1} + \mathbf{L}_{j+1}^j \times \mathbf{f}_{j+1}^{j+1} + \mathbf{MS}_j^j \times \mathbf{F}_j^j \\ \mathbf{\Gamma}_j &= (\sigma_j \mathbf{f}_j + \bar{\sigma}_j \mathbf{n}_j)^T \mathbf{z}_j \end{aligned} \tag{2.8}$$

where $\mathbf{f}_j$ and $\mathbf{n}_j$ are the forces and moments exerted on segment j by its antecedent segment, and $\mathbf{F}_j^j$ and $\mathbf{N}_j^j$ are the total external forces and moments exerted on segment j, respectively. $\mathbf{MS}_j$ is the (3×1) position vector defining the CoM of segment j w.r.t. R_j.

As a result, the inverse dynamic model of a floating base system is typically given as:

$$\begin{bmatrix} \mathbf{H}_{ww} & \mathbf{H}_{wc} \\ \mathbf{H}_{cw} & \mathbf{H}_{cc} \end{bmatrix} \begin{bmatrix} \ddot{\boldsymbol{\theta}}_w \\ \ddot{\boldsymbol{\theta}} \end{bmatrix} + \begin{bmatrix} \mathbf{b}_w \\ \mathbf{b}_c \end{bmatrix} = \begin{bmatrix} \mathbf{0} \\ \mathbf{\Gamma} \end{bmatrix} + \sum_{k=1}^{N_c} \begin{bmatrix} \mathbf{J}_{w_k}^T \\ \mathbf{J}_{c_k}^T \end{bmatrix} \mathbf{F}_k \tag{2.9}$$

where the upper part of the equation represents the base link dynamics, and the lower part accounts for the other chain's segment dynamics:

- $\mathbf{H}_{ww}$ (6×6) and $\mathbf{H}_{wc}$ $(6 \times N_J)$ are the base-link inertia matrices; $\mathbf{H}_{cw}$ $(N_J \times 6)$, $\mathbf{H}_{cc}$ $(N_J \times N_J)$ are the chains segments inertia matrices;
- $\ddot{\boldsymbol{\theta}}_w$ denotes the (6×1) linear and angular acceleration vector of the base-segment in the global system of reference;
- $\ddot{\boldsymbol{\theta}}$ and $\mathbf{\Gamma}$ are the $(N_J \times 1)$ joint acceleration and torque vectors, respectively;
- $\mathbf{b}_w$ (6×1) and $\mathbf{b}_c$ $(N_J \times 1)$ are the bias force vectors describing centrifugal, Coriolis, and gravity forces of the base-link and of the chain segments, respectively;
- N_c is the number of contact points with the environment;
- $\mathbf{J}_{w_k}$ and $\mathbf{J}_{c_k}$ are the Jacobian matrices expressed at contact point k that map external wrenches $\mathbf{F}_k = \begin{bmatrix} F_{X_k} & F_{Y_k} & F_{Z_k} & M_{X_k} & M_{Y_k} & M_{Z_k} \end{bmatrix}^T$ to the base-link and chains segments, respectively.

Software packages have been developed which allows performing symbolic optimization of these equations. In the current thesis Symoro+ [67] is used for dynamic models calculation.

2.3 Motion Capture Systems and Technologies

Various systems and technologies can be used to capture the human body movement. The current section aims at introducing the noninvasive motion capture technologies available in the literature with a focus on visual and inertial systems It is organized as follows: vision-based systems (section 2.3.1), IMUs (section 2.3.2), and force plates (section 2.3.3). An overview of additional sensors that may be used to assess human movement, beyond the current thesis, is given in section 2.3.4. Finally, section 2.3.5 presents systems based on a combination of the above sensors, like the one proposed in this thesis, referred to as hybrid systems.

2.3.1 Vision-Based Systems

Vision-based systems, also known as cameras-based or optical systems, use a number of cameras to capture information related to the human body movement. For this purpose, one [69, 70, 42] or multiple [71], static [69, 71] or moving [72] cameras may be used. Traditional systems track the trajectories of markers placed on the human body using multi-positioned cameras. More recently, marker-less systems have been alternatively developed using depth-camera sensors incorporated into devices such as the Microsoft Kinect [8].

2.3.1.1 Marker-Based Systems

Invasive imaging techniques are known as gold standard for analyzing human skeletal motion. Such techniques, however, are subject to several limitations. Beside being costly and restricted to a specific clinical environment, these expose the human body to radiation, and they usually do not allow real-time and full 3D multi-joints tracking because of either a very limited field of view, i.e., fluoroscopy, or inability to track motor tasks, i.e., X-ray images [62, 73]. Alternatively, optical and marker-based MCSs, also known as Stereophotogrammetric Systems (SSs), are considered as the non-invasive gold standard in motion capture [59]. Commonly in the literature, the reliability of new MCSs is validated by comparing their associated result with that obtained using such a system [74, 42, 75].

Stereophotogrammetry dates back to 1800s and is known as the science of quantifying human motions using measurements from two or multiple photographic images [76]. SSs often consist of active, i.e., emitting light, or passive, i.e., reflecting the light, markers placed on the human body to estimate its pose, i.e., position and orientation. Because of their reflectivity, these markers are synchronously detected from different views using multiple infrared cameras, which allows reconstructing their 3D position, i.e., time-of-flight

triangulation [77]. It is beyond the scope of this section to further explain how these 3D positions are calculated. However, further details may be found in [77]. An example of a SS is presented in Fig. 2.5.a. For 3D pose calculation, a minimum of three markers is typically required per each body segment. These are clustered on the skin above bones or anatomical landmarks surrounding joints of interest [78, 77] (see Fig. 2.5.b). Hereafter, different inverse kinematic algorithms may be used to compute the human body pose based on markers trajectories tracked throughout the RoM [62, 79].

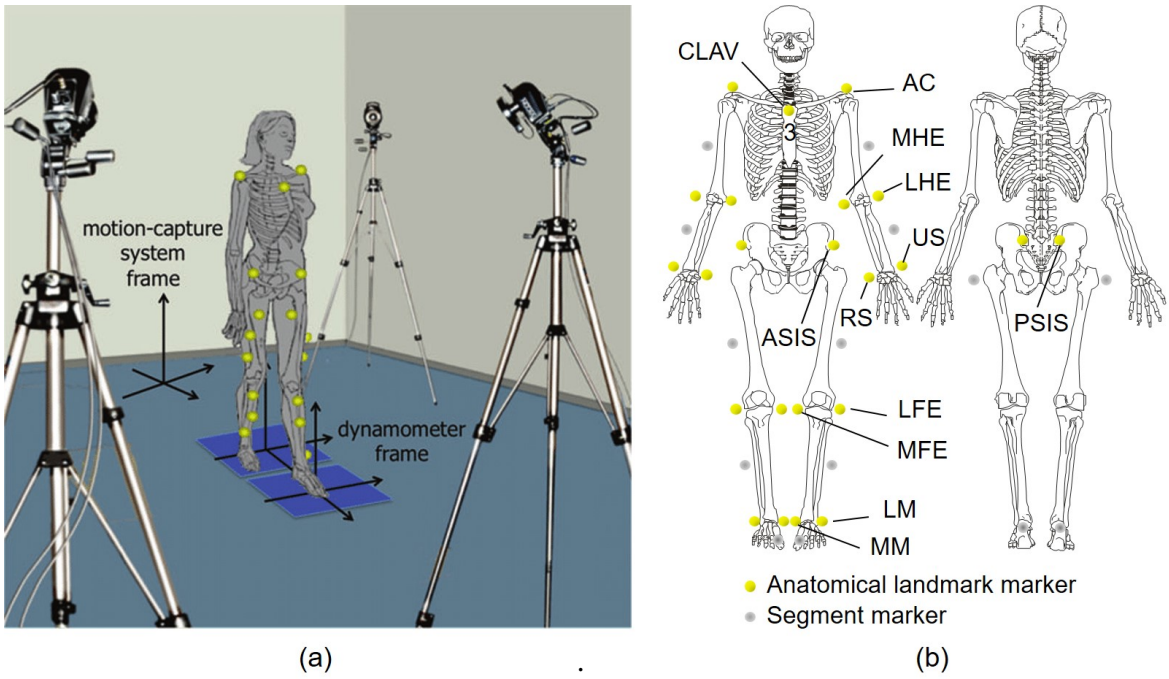

Fig. 2.5 (a): Motion analysis laboratory equipped with a SS and two force plates embedded in the floor [80]. (b): Set of reflective markers placed on the human body to estimate its pose. Lower-limbs anatomical landmarks: right/left Postero-Superior Illiac Spines (PSIS), Antero-Superior Illiac Spines (ASIS), Lateral and Medial Femoral Epicondyles (LFE and MFE), Lateral and Medial Malleolus (LM and MM). Upper-limbs anatomical landmarks: Middle Clavicle (CLAV), right/left Acromions (AC), Lateral and Medial Humerous Epicondyles (LHE and MHE), Radial and Ulnar Styloids (RS and US)

To record markers data, several commercial SSs are available in the market. These aim at facilitating the end-users real-time motion capture and visualization through high sampling rate cameras, retro-reflective markers and their accessories, as well as a processing software. Some of the world-wide leading manufacturers in SSs are the following [81]: Vicon (England), Optitrack (United States), Qualisys (Sweden), Motion Analysis (United States), and NDI (Canada). These systems have been widely used in various applications [82] and have all proven a sub-millimeter accuracy in tracking markers trajectories [83, 84, 71, 85, 86].

Among them, Optitrack [83, 82] features ease-of-use and more affordable prices, and is used in this thesis to measure stereophotogrammetric data.

Although being accurate, SSs sustain significant limitations in human motion analysis. Like any noninvasive sensors/markers-based MCS, these experience the fact that markers are skin-mounted and not bones-mounted. Such restriction would jeopardize the accuracy of the resulting pose estimate due to the so-called Soft-Tissue-Artifacts (STA) [87]. In practice, the movement and deformation of the underlying tissue (e.g., muscle, adipose) cause inevitable small displacements of the skin-mounted markers relative to the underlying bones [62]. These displacements yield a mismatch between the skin-markers and the tracking bone movements, thus errors in the latter's estimate, which are commonly referred to as STA [87]. Several research groups have sought to assess the magnitude of the STA and their effect on joint kinematics estimation. They primarily used invasive techniques and showed substantial and varying results based on markers locations and the activity being investigated [88–90]. Other groups have developed algorithms for reducing the effect of STA on bone pose estimate [88]. These tackled the problem at both single-body [91, 92] and multi-body [65] levels. More recently, new studies have been devised to model the displacement, i.e., rotation and translation, of a cluster of markers as the STA to be compensated for [87]. Among the algorithms, the Multi-body Kinematic Optimization (MKO) [65] has shown great potential and is used in the current thesis to compute the human body reference joint kinematics based on stereophotogrammetric data (see section 3.5). However, a study providing a full understanding of the problem and/or STA-free measurements remains a challenge [87].

Beside STA, SSs suffer from further limitations that make them inadequate for a large number of applications and/or users. Indeed, these systems are the most expensive ones in the 3D motion capture market due to their cutting-edge technology, such as high resolution/sampling rate cameras, as well as licensed sophisticated software. Prices may hit the bar of hundreds of thousands of dollars. Moreover, the hardware setup requires a complex and cumbersome preparation. Multiple cameras and cables need to be appropriately located to film subjects movement from different views while avoiding markers occlusion. Occlusion occurs when markers are invisible to the cameras due to a third body, such as obstacles present in the capture volume, or the subject's body segments while moving, which results in gaps within the trajectories of occluded markers. To this end, an increased number of tracking cameras placed in different positions is usually used in attempting to reduce occlusion, which require a dedicated large capture volume. Moreover, to compensate for the effect of STA and to avoid markers drop, markers must be carefully placed on the human body, especially those attached to the anatomical landmarks. Otherwise, the accuracy of the underlying segment pose estimate may be compromised, as shown by he works of Cappozzo et al. [88–90].

This process of markers placement may be time-consuming for end-users, especially when tracking the whole-body motion.

Fig. 2.6 ArUco markers

Recently, MCSs based on Augmented Reality (AR) markers has been developed as a low-cost alternative to track objects 3D pose [93]. These systems can use only one camera, although it would restrict the markers capture volume. AR markers, also known as fiducial (individually identifiable) markers, are planar, easily identifiable markers based on a unique and binary printed pattern. Once it is detected in the image, this pattern allows extracting the 3D position and orientation of the object that it is attached to using computer vision algorithms. Among several fiducial maker systems proposed in the literature, e.g., ARToolKit, ARToolKit, ARTag, ArUco, we use ArUco markers [94] together with OpenCV library [95] in this thesis. ArUco markers (see Fig. 2.6) are geometrically square, they consist of a black border and an inner binary matrix that is used to store a unique binary code of each pattern. A dictionary of ArUco markers allows identifying the different patterns. This is done in steps starting from the detection of square markers in the captured image, corners refinement and perspective distortion correction; then the resulting image is re-sampled into a binary matrix based on the marker size [95]. This matrix will be searched in the given dictionary so that it can be validated as ArUco if it matches with the markers or discarded in case of failure [95]. To make the detection process easier, ArUco dictionaries are designed with an optimized distance between markers so that they would be distinguishable while minimizing the chance of misidentifying a marker. After identifying the markers, and providing the camera calibration (see section 3.1.2), the markers tracked pose can be estimated w.r.t. the camera local coordinate system based on the markers detected corners, together with Levenberg-Marquardt optimization [96] [94] [95].

Few studies have assessed the accuracy of ArUco markers pose estimation in the literature [97, 98]. For instance in [99], AR markers pose was measured statically and compared to a gold standard SS with Root Mean Square Differences (RMSDs) of 1.4±0.6mm and 1.6±0.3deg, as the best obtained result for position and orientation, respectively. Despite this very good RMSD, the accuracy of AR markers pose estimate might be considerably affected by numerous factors in addition to markers occlusion, such as the camera calibration

and settings, i.e., resolution, distortion, focal length, as well as lighting conditions, distance from the camera, markers sizes, and viewing angle [99, 97]. Nevertheless, the fact of being extremely low-cost, robust, fast, and easy-to-use makes AR markers an interesting tool that can be used for pose estimation in several applications. Currently, such systems are mostly used for AR [100] and robot localization [101, 102]. Very few studies have explored the potential of using AR markers for the purpose of human motion analysis, which might be much further challenging [69, 103, 98]. In this context, there is a remaining gap of work to be done to validate the use of AR markers for applications of human motion analysis.

2.3.1.2 Marker-less Systems

Unlike traditional SSs, marker-less camera-based MCSs do not require physical body markers. Instead, they usually perceive depth using an infrared light-based pattern. Therefore, no markers suits need to be worn, and no complicated setup is required, which makes human motion capture much faster, easier, and more convenient for subjects. Devices based on RGB-depth sensors, such as the Kinect (Microsoft), with embedded skeleton tracking algorithms, are nowadays available [42, 8]. Yet, the Kinect was shown relevant for general purpose applications, where accuracy and speed are less crucial, and is still considered as not reliable and accurate enough for quantifying human motion (RMSD < 10deg) [104]. More recently, marker-less MCSs based on an RGB camera and a machine learning algorithm were applied to much further challenging scenes with multiple persons tracking [105, 106]. However, these systems are not yet accurate enough to estimate human body biomechanics, such as joint angles, and thus are not of interest for the clinical community. Moreover, such algorithms often need to be trained based on large scale datasets, which requires significant computational power.

2.3.2 Inertial Measurement Units-Based Systems

In the context of using wearable sensors for motor activity assessment, the IMUs have been widely promoted thanks to the advances in micro-electromechanical systems technology. Specifically, thanks to the considerable reduction in size (miniaturization), in cost and in energy consumption, these sensors can be used for ADL assessment in both indoor and outdoor environment settings without being restricted to a laboratory setup [107]. Moreover, IMUs-based MCSs, unlike camera-based ones, do not require line-of-sight and do not suffer from a limited sampling rate of the sensors.

[1] https://handsontec.com/index.php/product/mpu6050-accelerometer-gyro-sensor-module
[2] https://www.apdm.com
[3] https://www.xsens.com

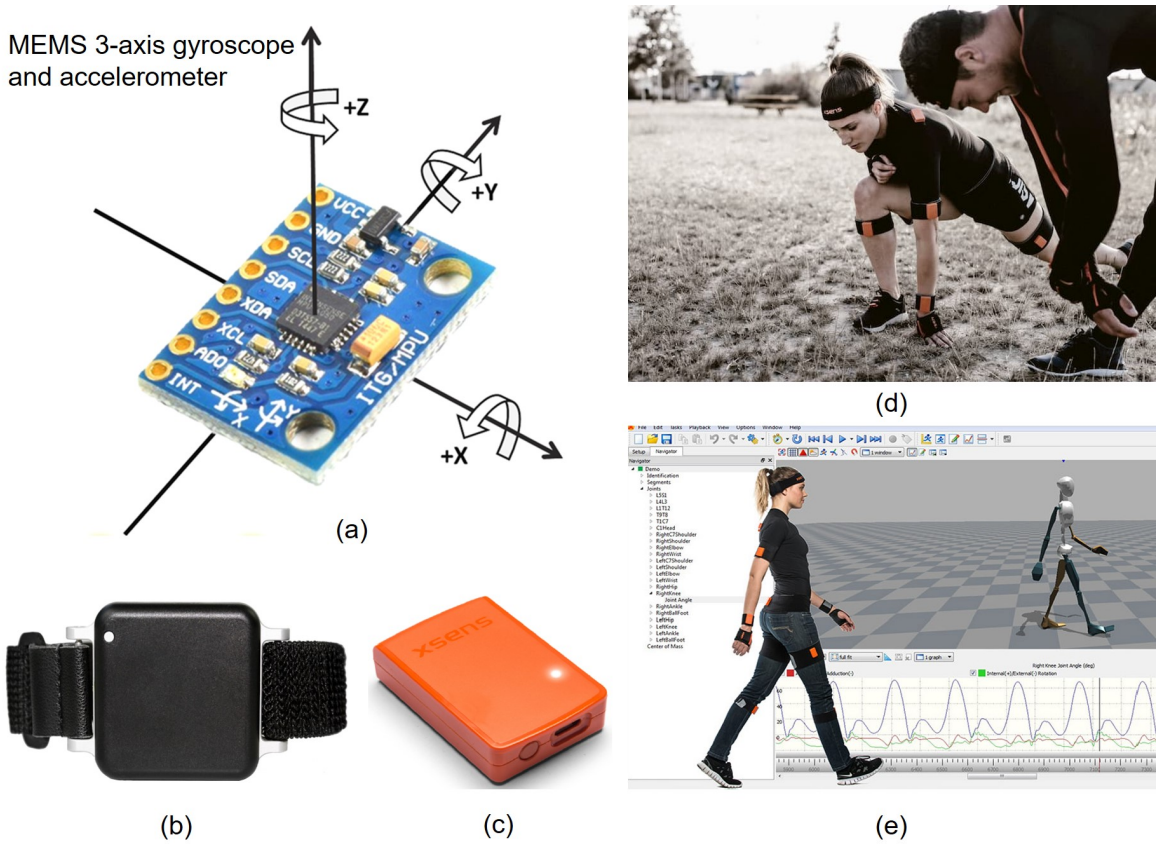

Fig. 2.7 Examples of commercial IMUs for indoor/outdoor motion tracking. (a): MPU 6050 embedding 3-axis accelerometer and gyroscope[1], (b): Opal IMU[2], (c): Xsens MTw IMU[3], (d): Motion tracking while running in a natural, outdoor environment[3], (e): Motion tracking during indoor gait[3].

An IMU, such as the ones shown in Fig. 2.7, primarily incorporates triaxial accelerometer and triaxial gyroscope measuring the 3D linear acceleration and the 3D angular velocity of the body that they are attached to, respectively. They may also include an additional triaxial magnetometer that measures the surrounding 3D magnetic field. Measurements are provided w.r.t. the IMU local coordinate system. For instance, one single-axis accelerometer consists of a mass-spring system to measure the 1D linear acceleration due to motion. Based on both Hooke's ($F = kx$) and Newton's ($F = ma$) laws, the displacement of a given mass m causes the deformation x of a spring with a known stiffness factor k, resulting in a force F that is linearly related to the acceleration a to be calculated. a is added to a static gravitational component g, both constituting the output of the sensor.

Commonly, one IMU sensor is assumed to be rigidly attached to each body segment of interest, and each IMU pose relative to its corresponding body segment needs to be priorly

calibrated (see section 2.4.1). IMUs can then track body segments poses, and joint trajectories can be obtained using inverse kinematics [108].

Theoretically, the IMU's 3D pose can be obtained by integrating and double integrating the gyroscope and accelerometer data, respectively. However, the accuracy of the IMU's pose estimation may be jeopardized due to the presence of non-linear and time-dependant drift in the sensor data. Moreover, in the vicinity of ferromagnetic materials, magnetic field may be disturbed resulting in additional drift [109]. For instance, the integration and double integration of noisy gyroscope and accelerometers data resulted, respectively, in a drift of 10-25deg after one minute [110], and in a position error that grows cubically in time [111].

Studies that have been developed in the literature for IMUs drift correction and IMUs-to-segments calibration are reviewed in section 2.4.

2.3.3 Force Plates

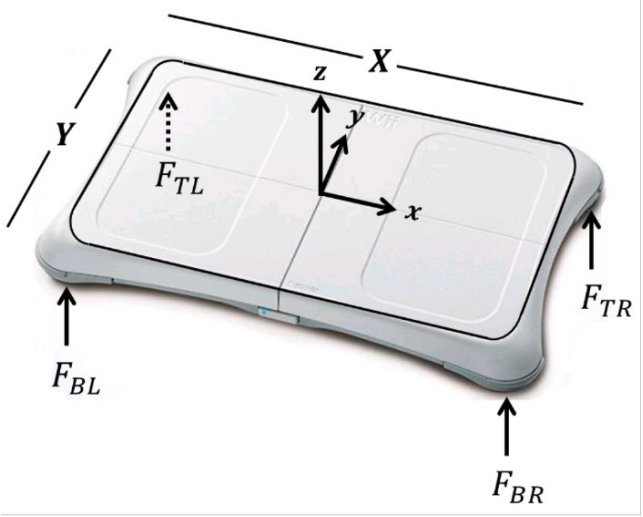

Fig. 2.8 The Wii Balance Board [112].

Human body kinetics are commonly analyzed in a laboratory equipped with SSs and force plates (see Fig. 2.5). Force plates or platforms are usually floor-embedded, such as the ones shown in Fig. 2.5. They are known by their high accuracy in measuring 3D Ground Reaction Forces and Moments (GRFMs). However, like SSs, these suffer from several limitations. Such devices are costly and require complicated hardware installation, making their use restricted to laboratory and inaccessible to the clinical community or for ADL assessment. Using a force plate for kinetics analysis requires subjects to stand on it while performing motor activities. The device's measurement surface, however, is small limiting the movements to be analyzed. Others have introduced mobile force plates such as the

AccuGait from AMTI[1] or the affordable Wii Balance Board (WBB) [112]. Both do not solve the issue of small measurement surface, however due to their portability and ease-of-use, these can be used in different environments with an advantageous trade-off price-accuracy. Moreover, by using the WBB, only the vertical force can be measured and the moments along the horizontal axes can be calculated (see Fig. 2.8).

The restrictions above have driven researchers to find alternative solutions to provide GRFMs measurements. They have shown possible the calculation of GRFMs by combining body joint kinematics and BSIPs into the dynamic equations of motion (Eq. 2.9) [113]. Accurate joint kinematics, however, are usually computed using SSs, which recall previous limitations of expensive costs and restriction to dedicated laboratory use, hence, emphasize the need to develop affordable, portable, and accurate MCSs.

2.3.4 Further Technologies

Beyond this thesis, further technologies have been used to analyze human motion, some of them being depicted in Fig. 2.9. Mechanical, acoustic, and magnetic systems are examples of such technologies.

Mechanical systems mainly consist of an articulated series of rigid mechanical pieces, such as exoskeleton robots worn by the human body. These pieces are linked through electro-mechanical transducers such as potentiometers or shaft encoders that are positioned about the joints of interest. The degree of deformation is proportional to the variation in angular displacement, which is measured during movements and can be conveyed wirelessly to a host computer. However, these systems are usually cumbersome, not practical, and suffer from misalignment with the user's joints, which may result in further errors in the joint angles estimates.

Acoustic or ultrasonic systems [114], such as the one depicted in Fig. 2.9.c, use high-frequency ultrasound waves to measure the position of an object. These waves travel through the air at the known speed of sound, such that the transmitter-receiver distance is determined based on the Time-of-Flight principle. Acoustic systems are relatively affordable compared to SSs, but much less accurate. Similarly to vision-based systems, they might be subject to line-of-sight obstruction between both emitters and receivers. The presence of walls, floors, and obstacles in the capture volume results in multi-path reflections, thus in additional noise in the measured distance. The performance of such systems might also be affected by environmental factors such as temperature, humidity, and wind. For instance, Bischoff et al. [115] used an ultrasonic system for sport localization and reported an error up to 0.05m.

[1] https://www.amti.biz

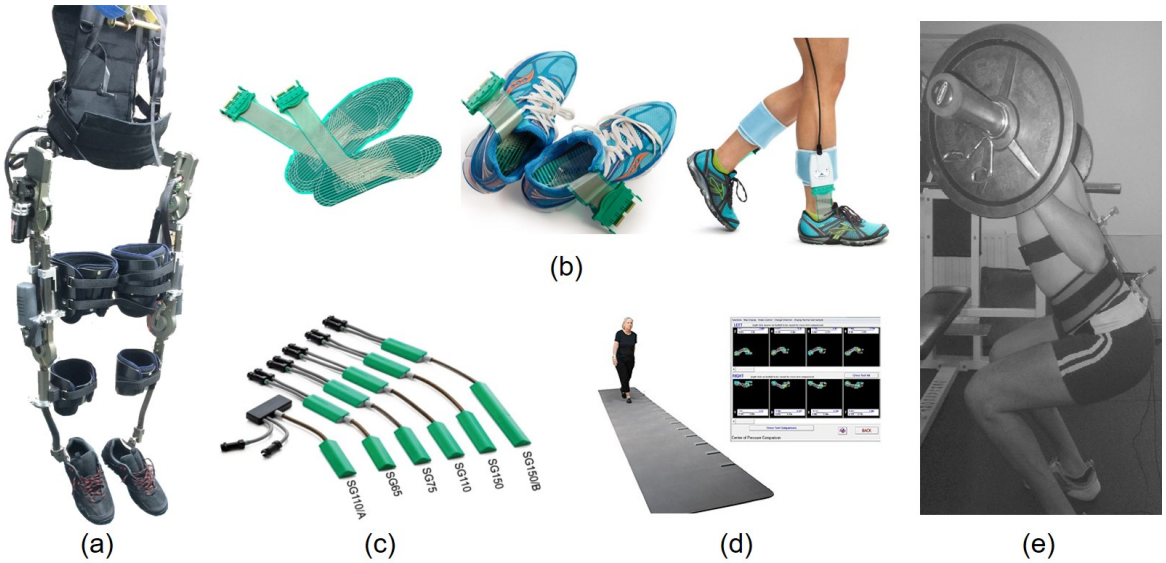

Fig. 2.9 Further technologies used to analyze human motion. (a) Lower-limbs exoskeleton E-ROWA [48], (b) The in-shoe F-scan system[1], (c) Flexible goniometers [46], (d) The GAITRite[2], (e) Acoustic MCS [114].

Magnetic systems use magnetic sensors placed on the object being tracked. The magnetic field generated by a magnetic transmitter is measured by these sensors and used to calculate object pose w.r.t. the transmitter. An example of such a system has been used in [116] for joint positions estimation. Although magnetic systems are occlusion-free and provide absolute 3D position measurements, they are subject to several limitations. Most importantly, they are highly sensitive to ferromagnetic disturbances, which make them poorly suitable to operate in non-ideal environments.

Other technologies exist for analyzing human motion. For instance, the GAITRite is a portable tool that is frequently used for gait analysis in clinical settings. It allows measuring the pressure under each foot as well as quantifying gait spatio-temporal parameters. Among in-shoe sensors by Tekscan (Boston, MA, USA), the F-scan provides pressure, timing and force data for gait analysis and the FlexiForce measures foot force distribution for falls detection. Other systems such as goniometers to measure joint angles and electromyography (EMG) to measure patients muscles activity while moving can be used [46]

[1] www.tekscan.com
[2] www.accesshealth.com

2.3.5 Hybrid Systems

More recently, hybrid systems have been promoted in motion capture technology. These consist in the combination of different types of sensors at the aim of providing a more robust and accurate 3D pose estimate. In this context, acoustic-inertial [117, 118], magnetic-visual [119], GPS-inertial [120], and visual-inertial systems have been developed. Examples of visual-inertial MCSs include accelerometers-AR markers [121], IMU-camera [122], IMU-laser [123], and gyroscope-aided optical flow-based systems [37]. However, such systems were only validated for object indoor/outdoor localization with limited accuracy exceeding few centimetres. Within the specific area of biomechanical motion estimation, some studies have proposed to combine visual and inertial sensors for joint kinematics estimation [70, 124–127] and are discussed in section 2.4. While such systems have shown their efficiency in mainly compensating for the IMUs drift, their tracking accuracy and/or expansion to several joints 3D motion estimation remain a major challenge with a great room for improvement.

Motivated by these studies, a new visual-inertial human MCS has been proposed and validated in this thesis.

2.4 Available Algorithms for Analyzing Human Motion

This section provides a brief literature review on algorithms related to human motion biomechanical analysis. Specifically, those related to the use of visual-inertial sensors for sensors-to-segments calibration (section 2.4.1), segments pose estimation (section 2.4.2), as well as algorithms for BSIPs identification (section 2.4.3), which have been investigated in this thesis, are reviewed along with their main contributions and limitations.

2.4.1 Sensors-to-Segments Calibration

When dealing with a MCS based on physical body sensors such as IMUs, one may consider the relative motion of the sensor attached at human body segment as the motion of that segment [128, 129]. In practice, the sensor local coordinate frame is not aligned with the human joint, which may result in large tracking errors [130, 131]. Moreover, there is a lack of standards on how to place IMUs sensors on body segments since IMUs do not provide pose measurements [132]. Thus, a sensor-to-segment calibration is first required to locate each sensor pose w.r.t. its corresponding body segment anatomical frame. The sensors calibrated pose is then assumed to be constant and used to track human body joint kinematics based on the sensors acquired data and an inverse kinematics process.

Traditionally, calibration techniques rely on a set of predefined specific body postures/movements [133, 134], such as T-pose and N-pose in Xsens MVN [135, 136] and upright posture [137], to be performed by the subject. Such calibration techniques, however, are cumbersome and could result in further errors based on the subjects ability to perform postures/movements accurately; thus they are not suitable to be used in clinical settings [132].

Some studies have proposed to use functional calibration methods but with simpler motions. For instance, a set of simplified movements that could be conducted by children was specified in [138]. With these movements, the authors aimed at calibrating the orientation of five IMUs sensors placed on the upper-limbs w.r.t. arbitrarily defined joint functional frames. Given that each conducted movement involved a single axis of the functional frame, all sensors data were introduced into an optimization process to estimate the best reliable axis per each movement. However, this study showed the convergence of the proposed algorithm without proper validation of joint angles estimation. Other researchers have used arbitrary functional movements along with kinematic constraints to locate IMUs on their corresponding body segments [139–142]. By assuming two adjacent segments equipped with two IMUs sensors and rotating around a fixed joint axis/center, they explored geometric constraints on angular velocity rotational direction and/or joint center linear acceleration. The transformation between both IMUs and body segments local frames were then identified through optimization to satisfy these constraints. These methods consisted of a few number of DoFs (1 or 2 DoFs) and were implemented for the elbow [141], knee, and ankle joints [139, 140]. Moreover, they required a relatively sufficient variation of the investigated joint RoM. However, a study on the types of movements that may lead to the most accurate results was not provided in these studies [143]. Although in [142], the authors extended the previous work to 3DoFs joint angle estimation, the proposed calibration method relies on the use of magnetometer data.

Recently, Chen et al. [130] proposed an online sensors-to-segments calibration method without using magnetometers data. The method was validated for online tracking of human treadmill gait using two commercial Xsens IMUs placed at the thigh and shank body segments. First, the quaternions defining the placement of each IMU w.r.t its corresponding hip/knee joint anatomical frame were calculated. This was done using the inclination due to the gravity at an initial, static lower-limbs position, as well as the heading angle optimized to satisfy the angular velocity constraint of the hinge joint motion located at the knee. In a second step, the calibrated IMUs-to-segments quaternions, accelerometers and gyroscopes data were introduced into a gradient descent optimization that estimated the knee flexion angle as well as the hip flexion and adduction angles. Results were validated using joint encoders of a

two DoFs robot, as well as w.r.t stereophotogrammetric and IMU-based benchmark tracking systems, and showed a mean RMSD lower than 4deg. Despite this interesting approach, results were validated with a single healthy subject and without 3D joint angles estimation.

In this thesis, a practical sensors-to-segments calibration method using a custom AR markers-based wand is developed (see section 3.2.1). Although the proposed method is conducted offline, the fact that the sensors 3D poses could be directly measured by the AR markers makes the calibration of the sensors-to-segments poses straightforward.

2.4.2 Segments Pose Estimation

As stated earlier, IMUs-based MCSs suffer from time-dependent and non-linear integrational drift, which causes the estimated pose to largely diverge [110, 111]. To deal with long-term drift, generally, accelerometers and magnetometers data are used. By combining accelerometer and gyroscope data using a sensor-fusion algorithm such as the Kalman filter, the drift effect was shown to be considerably mitigated [144]. However, with such approach, only the IMU 2D orientation can be estimated while the estimation of the orientation about the gravity axis remains inaccurate [145–147]. For a drift-free 3D orientation estimation, it has been shown that an additional source of information such as magnetometers or kinematic constraints must be added [146, 148, 149, 108, 150, 109]. Since magnetometers are sensitive to ferromagnetic disturbances, they are often used in controlled environments and tend to be avoided for applications outside of the laboratory [151, 152].

Instead of magnetometers, several studies have proposed to reduce the drift effect by using a minimum of one IMU sensor per each body segment of interest, together with a multi-body biomechanical model that allows the straightforward calculation of 3D joint kinematics. For instance, Lin and Kulić [150] proposed to estimate 3D leg motion in real-time by fusing IMU data using an EKF and a lower-limbs kinematic model. They achieved an average RMSD of 6.5deg when estimated joint angles were compared with those obtained using a reference SS. Further constraints were implemented by El Gohary et al. [109] at the aim of achieving better accuracy of upper-limbs 3D joint kinematics estimates. Using an Unscented Kalman Filter (UKF) and an upper-limbs kinematic model, they integrated a priori knowledge of joints physiological constraints to ensure feasible joint angles estimates, IMU random bias model to reduce the effect of unexpected error growth, as well as the concept of Zero Velocity Update (ZUPT) to correct the motion velocity. By resetting the motion velocity to zero once it is under a given threshold, the ZUPT allows cancelling the drift during the static phases of a motion while reducing the accumulated errors in the estimation of joint angles. However, it is susceptible to dynamic motion where the threshold values used to detect the different phases are not constant and have to be tuned as a function of the subject profile and movement. The

approach proposed by El Gohary et al. [109] showed remarkable results with a mean RMSD below 3deg except for the shoulder internal/external rotation joint where a larger RMSD was reported. However, it is important to note that these results were obtained with a 6 DoFs robotic arm, which suggests the absence of errors due to STA and sensors-to-segments calibration.

In general, two primary adaptive filters are frequently used in the literature for inaccurate sensors-fusion: the EKF and the UKF. Besides reducing the influence of the sensors' noise and generating filtered output signals, such filters-based algorithms allow the real-time estimation of indirect variables, such as joint angles of the biomechanical model being investigated and on which the sensors are attached. The Kalman Filter is a least square error optimizer filter assuming that the system being investigated is linear. In the case of a non-linear system, the EKF can be used as the first-order or second-order approximating estimator. In the case of high non-linearity, it is possible to use an UKF. The UKF works similarly to the EKF, but instead of using a single point to linearize the model, it takes sigma points and weights for each point to better approximate the system derivative. As stated by Laviola et al. [153], in an UKF several Runge-Kutta integrations are needed to propagate the sigma points through time, whereas in an EKF only one integration has to be performed. This will, obviously, dramatically influence the calculation time. UKF is usually favoured over EKF when the Jacobian of the model is difficult to be obtained. However, several studies [153, 109] have shown that when estimating human motion UKF does not improve significantly the estimation results. In this thesis, an EKF was selected given that the Jacobian of the models being investigated were computed symbolically. Details of the EKF formulation may be found in section 3.4.

When using an adaptive filter such as the EKF, significant errors might be due to non-optimal tuning of the filter parameters, yielding an emphasized influence of the IMU drift on joint kinematics estimate [154]. A good solution for drift correction is by considering problem-specific knowledge such as modelling the temporal evolution of joint trajectories during periodic gait cycle, or by making assumptions about the evolution of the signals being measured, i.e., angular velocity and linear acceleration [155–157, 154]. The assumption that joint trajectories may be modelled through a low-order Fourier series during periodic motions has already been made in the literature through several studies [158–160]. For instance, Joukov et al. [154] showed the superiority of a Fourier series-based model over a regular constant acceleration model used to describe joint temporal evolution during gait. A feedback adaptive frequency phase oscillator served to identify Fourier series coefficients. According to the authors, the learning rate and parameters tuning of the oscillator were decisive in the performance of their proposed method. Nevertheless, by performing a grid search, they were

able to fine-tune the filter parameters and obtain an accurate RMSD of 2.4deg for the hip and knee joint angles estimates. However, it should be noted that the proposed method could not estimate ankle angles, required a cumbersome sensor-to-segment calibration process, and used one IMU per segment configuration.

Some recent works have investigated the possibility of reducing the number of tracking sensors. A reduced sensors-count configuration allows improving the usability of the tracking system by simplifying the required setup and promoting subjects comfort. However, sparse measurements may lead to indetermination of the inverse kinematics problem to be solved and substantial inaccuracies in the kinematics estimate to be present. In [161], a planar squat task was analyzed based on a single IMU sensor located at the lower trunk. A lower-limb planar kinematic model, along with physiological constraints, were used in an offline optimization process aiming at estimating hip, knee, and ankle flexion/extension angles. The latter were modelled using a Fourier series expansion and were assessed with a mean RMSD of 3deg. Later, the authors extended their approach to the tracking of more complicated lower-limbs 3D rehabilitation motions [159]. Despite that a single IMU mounted at the shank was used to evaluate 3D joints angles, this method was also offline and confined to very specific case. More recently, Sy et al. [136] proposed to estimate hip and knee 3D joint angles using only three IMUs sensors attached to the sacrum, right and left shanks. The proposed method is based on the use of an EKF, including assumptions and constraints such as rigid body constraints, ZUPT, assuming flat floor, or making use of the total pelvis height. The presented results displayed a RMSD greater than 10deg when compared to a gold standard SS. This relatively large RMSD might be due to the fact that a proper sensor-to-segment calibration was missing and that a constant acceleration model was used to describe the joint trajectories evolution, which is intrinsically incorrect in human motion.

Recently, human motion quantification has been greatly promoted in assisted rehabilitation and assessment scales for patients suffering from motor impairments. During robot-aided rehabilitation therapy, Bertomeu-Motos et al. [162], [163] proposed to use data from magneto-inertial or accelerometer sensors along with the end-effector pose provided by the robot to quantify arm joint trajectories. Their algorithm was validated with post-stroke patients and w.r.t. a SS, showing a very good RMSD of 3.5deg. Nevertheless, these methods rely on the complementary use of the robot to solve inverse kinematics and do not consider the misalignment between the sensors and their corresponding anatomical segments. Repnik et al. [164] used Mihelji's algorithm [165], based on a Jacobian weighted pseudo-inverse, an adaptive Kalman gain, and magneto-inertial redundant data, to quantify the arm movements of post-stroke patients in a clinical environment. They analyzed metrics such as movement

time, smoothness, trunk stability, and similarity of the hand trajectory during the performed tasks. Nevertheless, the study lacks a proper quantitative validation of the joint trajectories.

To cope with the shortcomings of IMUs-based and markerless camera-based MCSs, other researchers have recently proposed to use extremely affordable and drift-free AR markers as an alternative solution to estimate the human body motion. In [69], gait analysis was conducted using a set of camera-tracked AR markers, one marker per body segment, which poses were introduced into a commercial Multi-body Kinematics Optimization (MKO). Results displayed a RMSD of 2.3cm for the step length and between 2.5deg and 6.7deg for pelvis, hip, and knee joint angles estimates. However, a large size of markers was used in this study, which allows to increase the tracking accuracy of the detected markers. Moreover, the system might be subject to markers occlusions. From an ergonomic perspective, such large markers might be awkward for patients performing ADL/rehabilitation tasks, and might be not suitable to track the movement of segments such as the foot or the wrist. Similarly, very large markers-based tracking was used in [98] to estimate the knee flexion/extension angle of a transtibial prosthesis, but using a much more expensive camera (2000$). With a reduced size of AR markers tracked with a single RGB-D camera, Bonnet et al. [103] proposed an affordable MCS that was able to estimate shoulder and elbow joint angles with a good accuracy of 3.8deg when compared to a SS. However, the system ran offline, was sensitive to markers occlusions and dealing with very simple motions.

Finally, in an attempt to compensate for each of the sensors drawbacks, particularly occlusion, drift, as well as sensors-to-segments calibration, some studies have analyzed the potential of fusing visual-inertial sensors for human body kinematics estimation [70, 124, 125, 29, 126]. Bleser et al. [70], for example, proposed to combine IMUs sensors and visual markers tracked with a chest-mounted IMU-camera using an EKF based on an upper-limbs kinematic model. With the proposed system, the authors intended to track the arm position while performing a specific task in an industrial environment. However, the system was not quantitatively validated. Instead, the authors showed the possibility of using the system as an alternative drift-free solution to IMU-magnetometers based ones in the presence of magnetic disturbances. The system performance in case of visual markers occlusion was not investigated as well. Moreover, a classical IMUs-to-segments calibration was performed based on static postures and magnetometers data. Glonek et al. [124] studied upper-limbs motion by fusing IMU and Kinect data. The system, using a classical static T-pose-based calibration, achieved a poor accuracy of the elbow joint angle (ranging from 4 to 15deg) and of the elbow and wrist joint positions (up to 3cm) estimates. According to the authors, the relatively large RMSDs might be due to IMU drift, while joint occlusions in some of the performed motions considered as challenging.

Motivated by the previous studies, the research presented in this thesis develops a new affordable, portable, and user-friendly visual-inertial human MCS. The system aims at dealing with the occlusion, drift and/or calibration issues, and improve the accuracy/robustness of 3D kinematics estimation. Joint kinematics are estimated by fusing only the accelerometer and gyroscope data of IMUs, i.e., without using magnetometers, as well as AR markers poses, into a constrained EKF based on a biomechanical model of the human body. The proposed algorithm incorporates prior knowledge of different types of constraints, including human joint feasible RoM, as well as soft joint constraints and rigid body constraints to obtain better joint kinematics estimates. It also models the IMUs random drift to further mitigate its effect during long tracking periods. The system calibration is done using a practical method taking advantage of the AR markers poses. Moreover, different EKF formulations are studied, as well as the possibility of using a reduced sensors-count configuration to estimate accurate 3D kinematics. The proposed system, its implementation and validation will be described in the following chapters.

2.4.3 Estimation of Body Segments Inertial Parameters

Traditionally, BSIPs have been inferred using anthropometric models in the case of humans and Computer-Aided Design (CAD) models provided by manufacturers in the case of robots. Based on the survey of Begon et al. [166], there are two types of anthropometric models: proportional and geometrical. Geometrical models consist in modelling body segments by means of simple mathematical shapes, i.e., ellipsoids, spheres, cylinders, or cones. BSIPs are then derived based on the calculated volume of these shapes. Such solutions, however, hardly represent the real BSIPs of the human since the latter's body segments are not that ideal in practice.

On the other hand, proportional models use regression equations, commonly referred to as Anthropometric Tables (AT), to estimate the human BSIPs as a function of the total body weight and height. For instance, segments' masses and lengths are expressed as a percentage of the total body mass and height, respectively. Similarly, CoM and inertia parameters are given as a function of segments' lengths, relative to the latter's proximal/distal extremity [167].

Proportional AT are usually based on statistical studies conducted on cadaveric subjects. Cadavers may be cut into pieces while evaluating each segment parameters [168]. Other researchers have used photogrammetric [169] and resonance imaging [170] techniques for this purpose. For instance, Dumas et al. [167] updated their regression AT by expressing the BSIPs in the local coordinate system of each corresponding segment. Doing so, they provided in 3D ten parameters per segment, i.e. mass, CoM 3D position, and six parameters

of the inertia tensor, which are used later in this study. AT, however, are usually based on a limited population with very specific age and mass configuration. Therefore, AT data become inaccurate when a non-typical body structure is investigated [171, 172], such as elders, children, obese, athletes, or hemiplegic.

Within robots, CAD models account for only mechanical segments that compose the robot. Thus, they do not take into consideration external components such as glued components, wires, electronics, or the embedded computer, added to the robot when it is used in practice, as well as the hardware evolution that may occur to the robot's structure with time [173, 174]. These components may constitute a non-negligible fraction of the total robot's weight, resulting in inaccuracies in the mass distribution among segments.

As a result, new identification methods have been developed in the literature for antropometric systems [171, 175]. These methods are inspired by the field of system identification developed since the 1980s for serial manipulator robots [68, 176–178]. However, for antropomorphic systems, i.e. human or humanoid robots, joint torques are not systematically available at contrary to serial manipulators [175]. Consequently, Venture et al. [171] proposed to use the external wrench, expressed at the base-link level and that can be measured by a force plate, to perform dynamic identification. The decoupling between joint torques and external wrench at the base-link level can be observed on the upper part of the general dynamics equation of a floating base system (see Eq. 2.9).

2.5 Human-Robot Physical Interaction

Robots exhibiting human-like behaviours are envisaged in our future society. Examples of expected scenarios include helping students in their learning, taking care of elders, and cooperating with humans in industries and other workplaces [179]. An example of a dance teaching robot from [180] is depicted in Fig. 2.1.o. Contrary to traditional industrial robots which follow precise actions programmed a priori, future robots may need to interact, both cognitively and physically, with the user [181]. Particularly, they need to perceive to a certain degree the activity they are confronted with, thus select the appropriate action they have to run in real-time [181].

Among human-robot interaction schemes, powered exoskeletons have attracted increasing interest in the last two decades for applications in performance enhancement [182], motion assistance and rehabilitation [10]. In rehabilitation, exoskeletons allow the execution of repetitive, accurate, and long-intensive exercises, leading to a more efficient and a faster rehabilitation process, as well as a considerable reduction in the workload of therapists [3, 11]. In general, exoskeletons are designed to be worn by the user and to replicate his

natural movement. With joint kinematics seemingly resembling those of the wearer, they allow specific-joint assistance by transferring a desired supportive torque to the wearer's impaired joints [3, 183].

As the exoskeletons operate in close interaction with the wearer, a primary function is to provide appropriate assistance without hindering the safety, comfort, and natural movement of the wearer. In general, physical properties such as size, weight, joint kinematics and dynamics, as well as the level of injury, may considerably vary between wearers. Therefore, there is an emerging need to develop subject-specific and model-based exoskeletons controllers, which account for these variations and provide a true assistance-as-needed to the wearer [182], [10], [48].

For controllers that are expected to predict the dynamic behaviour of the human-exoskeleton, an accurate model, which relies in part on a good estimation of the BSIPs, is of great importance. Moreover, an accurate dynamic model also allows inferring the wearer's motion intention through the calculation of human joint torques [184]. As a result, accurate and efficient BSIPs identification of human-exoskeleton systems would largely contribute to the development of exoskeletons robots.

Exoskeletons-assisted rehabilitation is still subject to several open challenges. One of the most difficult to tackle is the inevitable kinematic incompatibility between the wearer and the exoskeleton models. Indeed, to fully assist the wearer's joint, a correct alignment between both the exoskeleton and the wearer joint axes is required [183]. However, in practice, misalignment occurs between the two axes for two main reasons. First, the human instantaneous joint centers/axes are very difficult to be identified unless using invasive imaging techniques. For instance, the knee joint combines two rolling and sliding movements between the femur and tibia, resulting in the displacement of its joint axis pose along with its movement [12]. Second, the kinematic model of the exoskeleton robot usually consists of rigid mechanical segments articulated with pure rotational joints. The resulting human-exoskeleton joint misalignment may lead to undesired interaction forces that may load the wearer's joint during movement and results in an uncomfortable and unsafe human-robot interaction in case of large forces/torques interaction [185].

Attempts to deal with human-exoskeleton joints axes misalignment usually result in bulky and complex designs of exoskeletons [13]. Most of the exoskeletons prototypes seek the best trade-off between an accurate and a mechanically simple design of the exoskeleton [12]. Thus, there is still much room for improving the physical interaction between the human and the exoskeleton [12].

2.6 Summary

This chapter has reviewed the state of the art for human motion biomechanical analysis, specifically, for joint kinematics and BSIPs estimation. Human motion quantitative analysis is of great interest in various applications such as rehabilitation, medicine, sport, and ergonomics. For such analysis, several motion capture systems and technologies are available in the literature. Among these, SSs are the most mature representing the gold standard reference non-invasive technology currently available. Although SSs allow measuring the trajectories of retro-reflective markers with an excellent accuracy below 0.1mm, they are subject to several limitations. Most importantly, they are costly and requires a relatively complex hardware installation, which restricts their use to laboratory settings.

In general, for applications taking place outside of the laboratory and particularly for clinical applications, a human motion capture system needs to be transportable, affordable, easy-to-use, and of small dimensions to not hamper the user's motion while being accurate. There are two primary technologies that fulfill several of these criteria: IMUs-based and RGB/RGB-D cameras-based motion capture systems. Such systems have attracted increasing interest in the last years through plenty of research studies that have been developed in attempting to obtain accurate human joint kinematics estimation, some of them were discussed in section 2.4.2.

However, using IMUs to obtain accurate joint angles estimates remains a challenging problem. Nonlinear integrational drift and IMU-to-segments calibration issues might drastically affect the accuracy of the joint angle estimate and must be taken into account in any IMUs-based joint angle estimation solution. As it regards camera-based systems, there is a general consensus to say that marker-based systems are subject to occlusions and that marker-less ones are considered as relatively inaccurate for quantifying human motion, especially for clinical applications. As a result, researchers have considered the use of complementary information from either drift-free sensors or additional kinematic constraints together with IMU data. For instance, few studies have proposed to fuse visual and inertial data using adaptive filters such as the Extended Kalman Filter to compensate for each of the occlusion and drift drawbacks. Nevertheless, accuracy, reliability, and usability remain major challenges of the proposed alternative motion capture systems available in the literature.

Motivated by the previous studies, a new very low-cost, portable, and user-friendly motion capture system is proposed in this thesis. It aims at overcoming previous limitations related to human motion analysis based on affordable and portable tools. Particularly, it aims at improving robustness/accuracy of human 3D joint kinematics estimates while handling inaccuracies due to IMU drift and visual markers occlusion.

Chapter 3

Affordable Multi-Modal Motion Capture System Framework

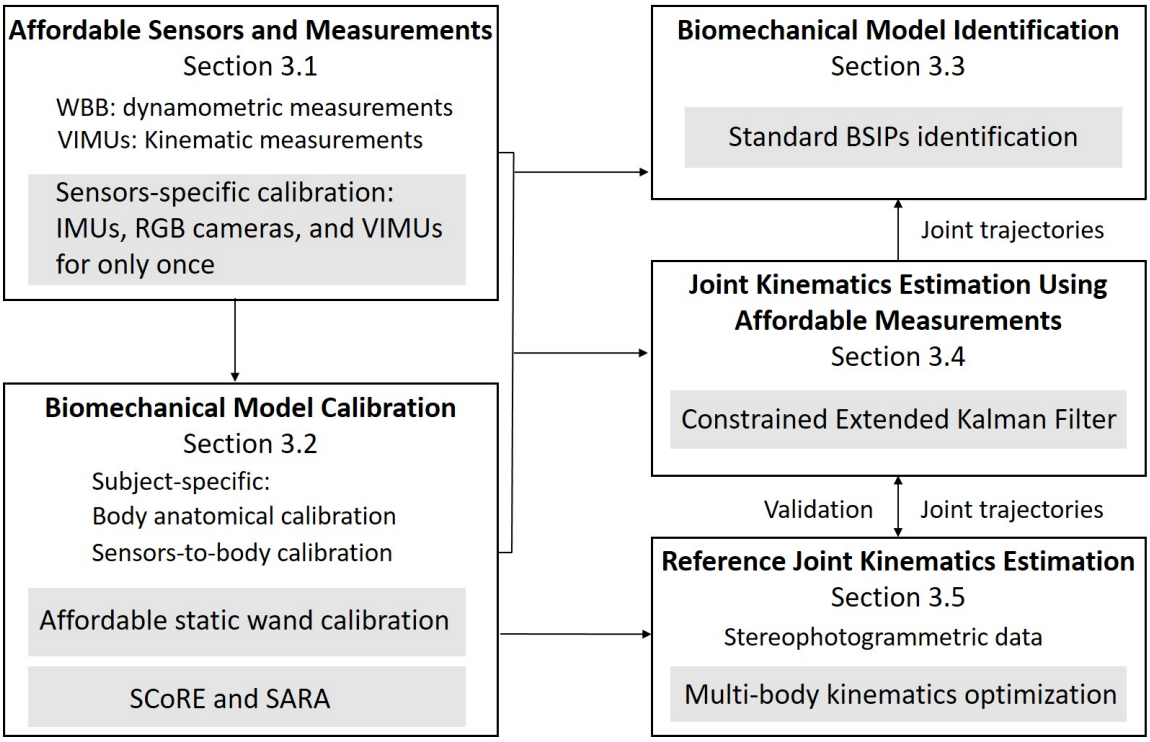

Fig. 3.1 An overview of the chapter 3 workflow.

Given the state-of-the-art presented in the previous chapter, this chapter aims at developing a new affordable MCS framework for kinematics quantitative assessment. Particularly, it presents the fundamental theoretical foundations for the following chapters. An overview of the chapter workflow is depicted in Fig.3.1. The proposed framework consists of both

kinematic and dynamometric measurements collected using affordable visual-inertial and WBB sensors, respectively. Each of these sensors requires a prior and unique calibration procedure that is described in section 3.1. Then, a subject-specific calibration (section 3.2) is used to determine joint centers positions, body segments lengths, as well as sensors placement on body segments. To compensate for the affordable sensors inaccuracies, measured data are lastly fused using both a CEKF and the biomechanical model being investigated for joint kinematics estimation (section 3.4). The resulting joint trajectories are validated using a gold standard SS (section 3.5) and introduced as inputs for the dynamic identification pipeline developed in section 3.3.

3.1 Affordable Sensors and Measurements

The proposed system is based on the simultaneous use of affordable IMUs, and a set of AR markers tracked with an affordable RGB camera. Thus, a new prototype of visual-inertial sensor has been developed in this thesis and is depicted in Fig.3.2. A Visual IMU (VIMU) consists of an IMU sensor and a minimum of one AR marker located on its top, providing synchronous measurements of the 3D pose, 3D linear acceleration, and 3D angular velocity of the body that it is attached to. Prior to data collection, each IMU (section 3.1.1), RGB camera (section 3.1.2), and the IMU-to-AR marker 3D rigid transformation (section 3.1.3) need to be calibrated. This calibration process is required to link all measurements to the same global reference as well as to obtain reliable input data.

On the other hand, dynamometric measurements are collected using an affordable WBB. Calibration of the WBB is relatively easily done by applying different known weights at the center point of the board surface, as described in [186]. The WBB amplifiers outputs are then calibrated as a function of the vertical force input.

3.1.1 Inertial Measurement Units Calibration

Due to imperfect manufacturing and physical characteristics, IMUs raw data usually suffer from systematic inaccuracies as well as random noise. Particularly, an IMU might be subject to inaccurate scaling factors, non-orthogonal sensor's local frame, and non-zero biases. The process of identifying and compensating these inaccuracies is known as IMU calibration.

Commercial IMU sensors are usually factory calibrated using specific external equipment. The latter provide known reference values that are compared with the IMU raw measurements to determine its inaccuracies parameters. However, this is not the case for the affordable IMUs, such as the ones used in this study. Thanks to the approach proposed by Tedaldi et

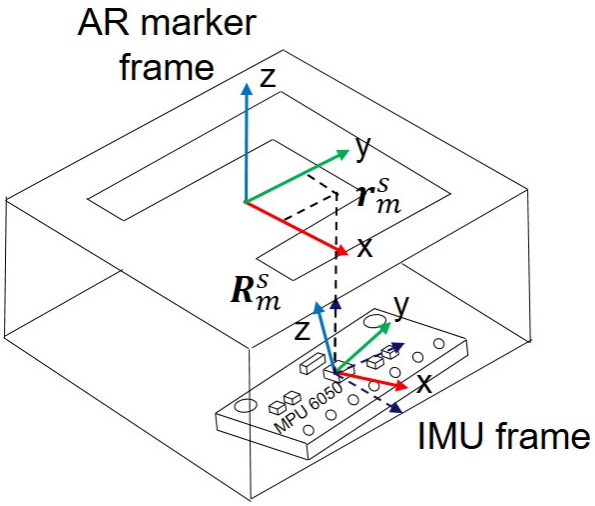

Fig. 3.2 A VIMU first prototype composed of an affordable IMU sensor and a minimum of one AR marker located on its top. The marker-to-IMU 3D rigid transformation ($\mathbf{r}_m^S$, $\mathbf{R}_m^S$) that must be compensated from calibration due to mounting inaccuracies is also described.

al. [187], the calibration of extremely affordable accelerometers and gyroscopes sensors is possible without the aid of any external equipment. It consists of a sensor multi-position scheme to identify the inaccuracies that could affect the sensor based on gravity sensing.

In this context, the independent contribution of each of the above-mentioned inaccuracies is used to derive a mathematical calibration model of the sensor relating its both raw and calibrated outputs. Ideally, both accelerometer and gyroscope share a single 3D frame with perfect orthogonal axes, defining the IMU local frame. Otherwise, they would measure inconsistent linear acceleration and angular velocity about two different axes, that both do not represent the real movement, i.e., rotation or translation, axis of the IMU. In practice however, each accelerometer and gyroscope axis is deviated by a relatively small angle yielding two distinct non-orthogonal frames of both sensors. Let assume $\mathbf{R_M}$ the rotation matrix linking the real misaligned frame of the sensor to a desired ideal frame. According to Tedaldi et al. [187], $\mathbf{R_M}$ is given as:

$$\mathbf{R_M} = \begin{bmatrix} 1 & -\alpha_{yz} & \alpha_{zy} \\ 0 & 1 & -\alpha_{zx} \\ 0 & 0 & 1 \end{bmatrix} \tag{3.1}$$

where α_{yz}, α_{zy}, and α_{zx} represent the non-orthogonality misalignment errors to be identified, such that α_{ij} denotes the rotation of the sensor i^{th} axis around the j^{th} axis of the new assumed

orthogonal frame. Using $\mathbf{R_M}$, the sensor's frame may be orthogonalized and its corresponding deviated output due to misalignment, may be corrected.

On the other hand, scaling factors are constant scalars that allow converting the current sensor's output in terms of physical quantities, that is to say acceleration or velocity measurements. A bias error is a non-zero constant offset added to the sensor's output although it is not undergoing any movement. Let the matrix $\mathbf{S}$ and the vector $\mathbf{b}$, given below, denoting scaling and bias errors, respectively:

$$\mathbf{S} = \begin{bmatrix} S_x^s & 0 & 0 \\ 0 & S_y^s & 0 \\ 0 & 0 & S_z^s \end{bmatrix} \quad \mathbf{b} = \begin{bmatrix} b_x^s \\ b_y^s \\ b_z^s \end{bmatrix} \tag{3.2}$$

with S_i^s and b_i^s, $i = x,y,z$, are the scaling and bias factors along the i^{th} axis, respectively.

As a result, the error model of an IMU sensor, particularly of an accelerometer sensor, may be formulated as follows:

$$\mathbf{a}_{sc}^s = \mathbf{R_M}\,\mathbf{S}\,(\mathbf{a}_s^s + \mathbf{b}) \tag{3.3}$$

where $\mathbf{a}_{sc}^s$ is the calibrated acceleration that is function of the sensor raw acceleration $\mathbf{a}_s^s$ and the vector $\mathbf{V}_{acc} = \begin{bmatrix} \alpha_{yz} & \alpha_{zy} & \alpha_{zx} & S_x^s & S_y^s & S_z^s & b_x^s & b_y^s & b_z^s \end{bmatrix}$ gathering the different inaccuracies to be identified.

In the current study, the approach proposed by Tedaldi et al. [187] is used to calibrate accelerometers sensors. Doing so, $\mathbf{V}_{acc}$ is identified based on the fact that the acceleration's magnitude measured in static position corresponds to gravity. Thus, all parameters are computed by minimizing the cost function given by Eq. 3.4 over a set of $N_P \simeq 50$ different static poses of the sensor.

$$f(\mathbf{V}_{acc}) = \min_{\mathbf{V}_{acc}} \sum_{k=1}^{N_P} (\|\mathbf{g}\|^2 - \|\mathbf{a}_{sc}^s\|^2)^2 \tag{3.4}$$

where $\|\mathbf{g}\|$ represents the norm of the gravity vector. The optimization problem was solved using the standard Levenberg-Marquardt algorithm [96].

Regarding the gyroscope sensor, a simple subtraction of the mean bias occurred after one minute of static recording was sufficient to show data consistency. Once obtained, the calibration parameters are kept constant whenever we use the same sensors.

3.1.2 RGB Cameras Calibration

To detect AR markers 3D poses from 2D images, camera(s) calibration is first required. Both single (section 3.1.2.1) and stereo cameras calibration (section 3.1.2.2), considered in the current thesis, are concisely explained below.

3.1.2.1 Single Camera Calibration

In general, camera calibration refers to identify the camera intrinsic and extrinsic parameters. Extrinsic parameters describe the pose of a camera w.r.t. a second one or to the global system of reference. They allow expressing 3D world coordinate points in the camera's coordinate system and vice-versa. Whenever a camera is moved or re-oriented, its extrinsic parameters change, thus need to be re-calibrated.

On the other hand, intrinsic parameters refer to a camera's individual characteristics, such as focal length and distortion coefficients. By having such parameters, a mathematical camera model that allows the conversion from 3D to 2D image coordinate points can be defined. For instance, the pinhole model is commonly used in the literature and OpenCV library [95].

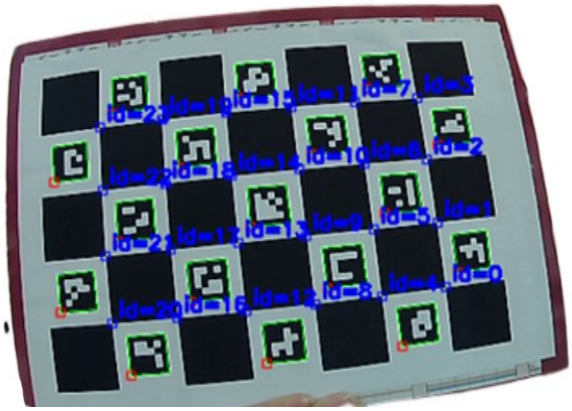

Fig. 3.3 ChArUco board.

To calibrate the camera model unknown parameters, we need to measure external 3D coordinate points from the scene covering the camera's field of view. A calibration pattern is commonly used to obtain easily interpretable and more accurate measurements of 3D world coordinate points. For better accuracy, it must be captured through a minimum of 10 images taken from different poses [95]. Calibration is then based on detecting corners of the calibration pattern and their corresponding 2D coordinate points where they appear in the image. Hereafter, the required unknown parameters are usually estimated by minimizing

the reprojection error between the projected, i.e., model-derived, and the measured image coordinate points in a least-squares mode.

Among calibration patterns that can be used, the so-called ChArUco board (Fig. 3.3), together with open-source ArUco [94] (see section 2.3.1.1) and OpenCV [188] libraries, is used in this thesis. It consists of a chessboard where the white squares are filled with ArUco markers. Given that a unique ID identifies each marker, the chArUco board allows defining an ID for each detected corner on the board. This would be useful in several situations such as in pose estimation or when the calibration board is not entirely detected in front of the camera.

3.1.2.2 Global Reference Frame and Stereo Calibration

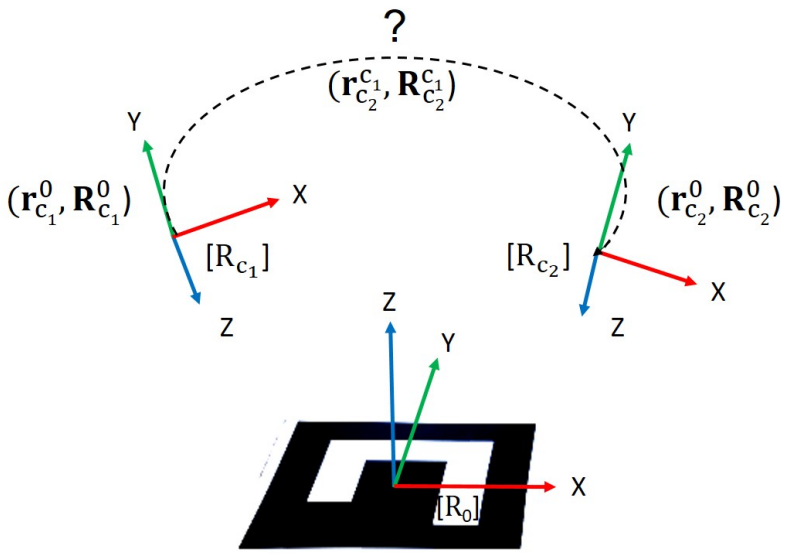

Fig. 3.4 The global system of reference R_0 is assigned using a dedicated AR marker. For stereo calibration, each camera 3D pose is derived w.r.t. R_0.

As discussed in the previous section, camera intrinsic parameters are calibrated using a ChArUco board. As a result, an AR marker 3D pose is detected w.r.t. the camera's local coordinate system using open-source ArUco library [94] (see section 2.3.1.1). This pose, however, is not easy to be interpreted neither to be derived using a kinematic model for example. Thus, the camera's 3D pose, i.e., extrinsic parameters, is derived w.r.t. a global reference frame R_0 that is defined using an independent AR marker. As a result, all markers poses can be expressed in R_0, as given by the Eq. 3.5 below:

$$\begin{aligned} \mathbf{r}_m^0 &= \mathbf{r}_c^0 + \mathbf{R}_c^0\, \mathbf{r}_m^c \\ \mathbf{R}_m^0 &= \mathbf{R}_c^0\, \mathbf{R}_m^c \end{aligned} \tag{3.5}$$

where ($\mathbf{r}_c^0$ (3×1), $\mathbf{R}_c^0$ (3×3)) and ($\mathbf{r}_m^0$ (3×1), $\mathbf{R}_m^0$ (3×3)) refer, respectively, to the 3D pose of the tracking camera and a random AR marker w.r.t. R_0. Whereas $\mathbf{r}_m^c$ (3×1) and $\mathbf{R}_m^c$ (3×3) denote the marker's 3D pose detected in the camera's local coordinate system.

In the case of two or multiple cameras, it is important to further align the different local coordinate systems w.r.t. R_0. For instance, the stereo calibration, carried out in this thesis, refers to further identify the 3D transformation between two cameras whose relative pose is fixed (see Fig. 3.4). Each camera's pose is derived relatively to R_0 and used to align the cameras corresponding local frames as follows:

$$\begin{aligned} \mathbf{r}_{c_2}^{c_1} &= (\mathbf{R}_{c_1}^0)^T\, (-\mathbf{r}_{c_1}^0 + \mathbf{r}_{c_2}^0) \\ \mathbf{R}_{c_2}^{c_1} &= (\mathbf{R}_{c_1}^0)^T\, \mathbf{R}_{c_2}^0 \end{aligned} \tag{3.6}$$

with ($\mathbf{r}_{c_2}^{c_1}$ (3×1), $\mathbf{R}_{c_2}^{c_1}$ (3×3)) denoting the required 3D pose of camera 2 local frame w.r.t. camera 1 local frame, as shown in Fig. 3.4.

3.1.3 Visual Inertial Measurement Unit (VIMU) Calibration

Once both IMUs (section 3.1.1) and RGB camera(s) (section 3.1.2) are calibrated, VIMU calibration is the last sensor-dependent calibration that needs to be done prior to data collection. Due to mounting imperfections, a calibration process of the VIMU is needed, which corresponds to the identification of the 3D rigid transformation between its embedded IMU sensor and the center of each AR marker located on its top (see Fig. 3.2). Indeed, the IMU measurements are provided in their sensor local frame, whereas, the 3D pose at the center of an AR marker can be expressed w.r.t. the global reference frame R_0 (see the previous section). To link all measurements to the global reference frame, the IMU-marker relative transformation must be known. Otherwise, the position and orientation offsets between IMU and marker will result in inconsistent input data for joint kinematics estimation.

In the literature, standard hand-eye and Kalman-filter based approaches have been usually used for camera-IMU calibration [189]. In this study, the pose information provided by the AR marker can be used. A two-fold calibration process is conducted in this context. First, the rotation matrix $\mathbf{R}_m^s$ (3×3), from the IMU local frame to the one of the AR marker, is determined by collecting data over N_P different static pose of the sensor in front of the camera. For each static pose i, both marker rotation matrix $\mathbf{R}_{m_i}^0$ (3×3) and the IMU linear acceleration $\mathbf{a}_{sc_i}^s$ (3×1) are measured. The marker acceleration statically expressed in its

corresponding local frame is thus given by projecting the gravity vector $\mathbf{g}$, expressed in R_0, as follows:

$$\mathbf{a}_{m_i}^{m} = (\mathbf{R}_{m_i}^{0})^T \mathbf{g} \quad i = 1, ..., N_P \tag{3.7}$$

The required $\mathbf{R}_m^s$ can be computed as shown in Eq. 3.8, through the Moore-Penrose pseudo-inverse of the vector $\mathbf{a}_m^m$ $(3 \times N_P)$ gathering all markers accelerations expressed in the marker's local frame. $\mathbf{a}_{sc}^s$ $(3 \times N_P)$ refers to the vector of all IMU accelerations measured in the IMU local frame.

$$\mathbf{R}_m^s = \mathbf{a}_{sc}^s \, (\mathbf{a}_m^m)^+ \tag{3.8}$$

Once the IMU-to-marker 3D orientation differences have been estimated, the second step consists in calculating the marker 3D position in the IMU frame. Thanks to $\mathbf{R}_m^s$ from Eq.3.8, both IMU and marker will rotate with known angular velocities. In other terms, when the sensor is rotating, it is possible to infer the marker angular velocity from the IMU's one using $\mathbf{R}_m^s$. Regarding the acceleration, the change in the sensor's motion direction will result in an additional centripetal acceleration that is function of the perpendicular distance toward the center of rotation. Thus, the relation between IMU and marker linear accelerations can be calculated based on the following equation [189]:

$$\mathbf{a}_m^m = \mathbf{R}_m^s \, [\mathbf{a}_s^s - \mathbf{a}_c^s] + \mathbf{a}_c^m \tag{3.9}$$

where $\mathbf{a}_c^s$ and $\mathbf{a}_c^m$ represent the centripetal accelerations of the IMU and the markers in their associated coordinate system, respectively. The centripetal acceleration of a body B at a point P is given by [189]:

$$\mathbf{a}_c^B = \mathbf{\Omega}_B^B \times (\mathbf{\Omega}_B^B \times \mathbf{r}_P^B) \tag{3.10}$$

with $\mathbf{r}_P^B$ is the translation vector connecting the point P to the center of rotation and $\mathbf{\Omega}_B^B$ is the angular velocity of the body B in its associated frame. Based on the marker's 3D pose, linear regression is used to identify the center of rotation. Furthermore, the marker linear acceleration is numerically computed as the filtered second derivative of its measured position. Thus, by applying these equations, the unknown translation vector $\mathbf{r}_m^s$ linking the marker to the IMU w.r.t. the IMU local frame can be estimated.

3.2 Biomechanical model Kinematics Calibration

Once VIMUs are calibrated, a biomechanical model (refer to section 2.4) is used to relate the VIMUs measurements with the human body joint kinematics to be calculated. Commonly, a

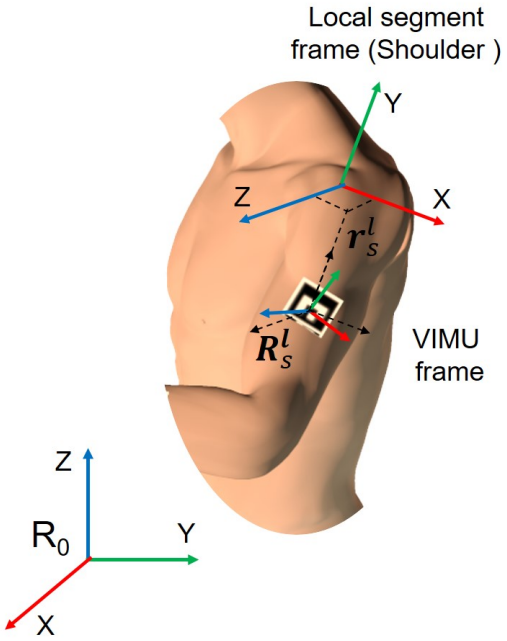

Fig. 3.5 The sensor local pose w.r.t. its segment anatomical frame ($\mathbf{r}_s^l, \mathbf{R}_s^l$) exemplified for the shoulder.

minimum of one VIMU sensor is assumed to be rigidly attached to each body segment and used to track its kinematic parameters. A sensor-to-segment 3D rigid transformation therefore exists between each VIMU frame and its corresponding body segment anatomical frame (see Fig. 3.5). This transformation, as well as segments lengths, have to be accurately estimated so that sensors data allow calculating consistent joint angles using inverse kinematics. To this end, a prior biomechanical model calibration is required. It consists, first, of an anatomical calibration that allows defining the poses of the body segments anatomical frames, i.e., joint centers/axes, w.r.t. the global reference frame R_0. Using these poses, segments lengths can be calculated as the distance between each two consecutive joint center positions. Second, a sensor-to-segment 3D constant relative pose, i.e., ($\mathbf{r}_s^l$, $\mathbf{R}_s^l$) in Fig. 3.5, is calculated and used to align the sensors data in their corresponding segments anatomical frames. This suggests both sensors and anatomical poses to be collected simultaneously w.r.t. R_0. Calibration outcomes are then used as inputs to the dynamic equations of motion for both kinematics and dynamics estimation (see Fig. 3.1 and Eq. 2.9).

In this study, anatomical calibration has been conducted using a new practical method that is proposed in section 3.2.1 based on AR markers detected poses and a custom calibration wand. Section 3.2.2 presents functional method used from the literature for our reference joint centers/axes estimation.

3.2.1 Affordable Static Wand-Based Calibration

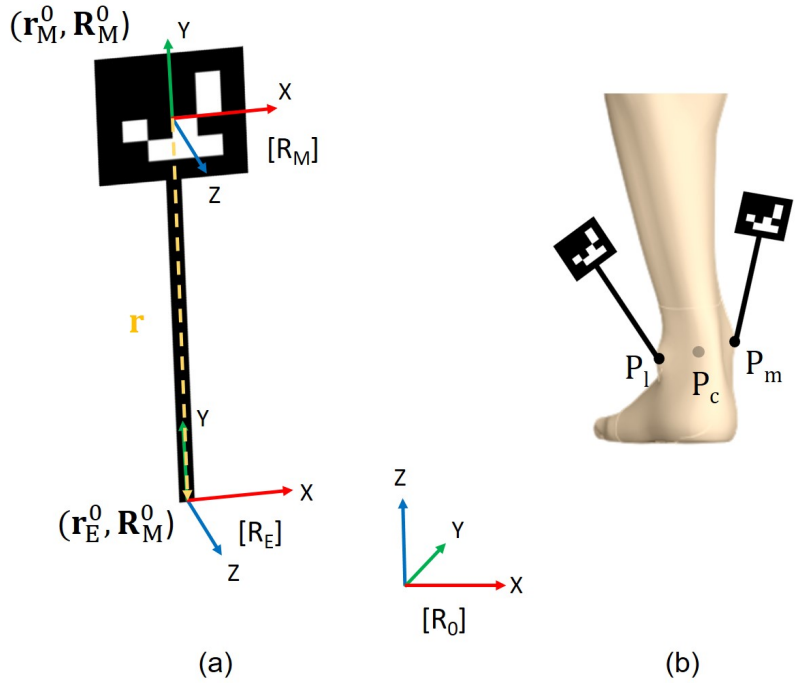

Fig. 3.6 Affordable wand-based calibration. (a): The proposed calibration wand of well-known dimensions. (b): Pin-pointing anatomical landmarks of interest using the calibration wand is exemplified for the ankle.

Since it is difficult to access anatomical joint centers positions, a custom calibration wand (Fig. 3.6), of known dimensions, has been designed. It is composed of a dedicated AR marker on one side and of a stick on the other side making it easy to pin-point anatomical landmarks of interest. Once the AR marker is detected in front of the camera, its 3D pose is obtained w.r.t. the global reference frame R_0 and is used to estimate the pin-pointed position at the wand's extremity, as follows:

$$\mathbf{r}_E^0 = \mathbf{r}_M^0 + \mathbf{R}_M^0 \, \mathbf{r} \tag{3.11}$$

where $\mathbf{r}_E^0$ (3 ×1) is the 3D position of the wand's extremity point E to be calculated w.r.t. R_0 and $\mathbf{r}$ (3 ×1) is the known position vector connecting E to the center of the AR marker. $\mathbf{r}_M^0$ (3 ×1) and $\mathbf{R}_M^0$ (3 ×3) denote the 3D pose at the center of the AR marker expressed in R_0.

The estimation of joint center positions is then based on simple linear regressions $\mathbf{p}_C = \frac{\mathbf{p}_m + \mathbf{p}_l}{2}$ with $\mathbf{p}_C$ representing the 3D position of the joint center and $\mathbf{p}_m$, $\mathbf{p}_l$ the medial and lateral positions of anatomical landmarks, respectively. For instance, Fig. 3.6.b exemplifies

the ankle joint center as the middle point between pin-pointed lateral and medial malleolus. Similarly, the pelvis joint center position is computed as the mid-point between left and right PSIS and ASIS landmarks (see Fig. 2.5.b for the definition of anatomical landmarks). The regression proposed by Bell [190] is used to predict the Hip Joint Center (HJC) position based on the distance between the left and right ASIS, as given by the Eq. 3.12 below:

$$\begin{aligned} \mathbf{p}_{RHJC}^{PEL} &= \mathbf{p}_{RASIS}^{PEL} + d \begin{bmatrix} 0.19 & -0.30 & -0.14 \end{bmatrix}^T \\ \mathbf{p}_{LHJC}^{PEL} &= \mathbf{p}_{LASIS}^{PEL} + d \begin{bmatrix} 0.19 & -0.30 & 0.14 \end{bmatrix}^T \end{aligned} \tag{3.12}$$

where $\mathbf{p}_{RHJC}^{PEL}$, $\mathbf{p}_{LHJC}^{PEL}$ and $\mathbf{p}_{RASIS}^{PEL}$, $\mathbf{p}_{LASIS}^{PEL}$ represent respectively the 3D positions of right and left HJC and ASIS expressed in the pelvis anatomical frame defined according to Bell [190], and d denotes the LASIS-RASIS distance.

Pin-pointing anatomical landmarks is performed simultaneously while recording VIMUs data statically, such that each sensor's local pose can be calculated w.r.t. its corresponding segment anatomical frame.

3.2.2 Symmetrical Center and Axis of Rotation Estimation

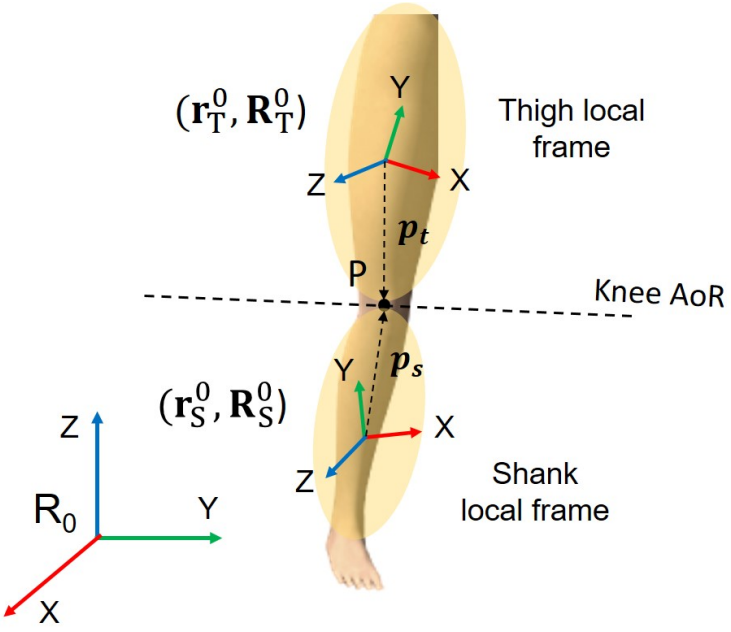

Fig. 3.7 SCoRE and SARA notations exemplified for the knee.

In this thesis, the method proposed and validated by Ehrig et al. [191, 192] has been considered for anatomical calibration. Unlike the wand-based static calibration, this method requires functional movements that would sufficiently excite the joints centers/axes to be identified. Particularly, joint centers are located using the Symmetrical Center of Rotation Estimation (SCoRE) method [191]. Whereas, the Symmetrical Axis of Rotation Approach (SARA) allows estimating joint axes [192]. Both SCoRE and SARA rely on the assumption that the moving Center/Axis of Rotation (CoR/AoR) of a target joint is stationary w.r.t. the two adjacent segments it connects. For the sake of clarity, let's consider these methods to estimate the knee joint CoR and AoR. Two local coordinate systems are required to be defined at the thigh and shank segments (see Fig. 3.7). Let $\mathbf{p_t}$ and $\mathbf{p_s}$ be the 3D positions of a point P expressed in the thigh and shank local frames, respectively. P represents the required CoR, or an arbitrary point located on the target AoR (see Fig. 3.7). Since both $\mathbf{p_t}$ and $\mathbf{p}_s$ refer to the same point P, they must therefore coincide throughout the movement when converted into the global reference frame. This yields the following cost function:

$$f(\mathbf{p}_t, \mathbf{p}_s) = \sum_{j=1}^{n} \| \, (\mathbf{R}^0_{T,j}\, \mathbf{p_t} + \mathbf{r}^0_{T,j}) - (\mathbf{R}^0_{S,j}\, \mathbf{p_s} + \mathbf{r}^0_{S,j}) \, \|^2 \tag{3.13}$$

where ($\mathbf{R}^0_T$,$\mathbf{r}^0_T$) and ($\mathbf{R}^0_S$,$\mathbf{r}^0_S$) are the transformations, i.e., rotation matrix and translation vector, that define the thigh and shank local frames in the global system of reference, respectively and n denotes the number of samples. Based on Eq. 3.13, the required CoR/AoR may be assessed by solving the linear least-square problem given below:

$$\mathbf{Y}\hat{\mathbf{p}} = \mathbf{z}$$

such as:

$$\begin{bmatrix} \mathbf{R}^0_{T,j=1} & -\mathbf{R}^0_{S,j=1} \\ \vdots & \vdots \\ \mathbf{R}^0_{T,j=n} & -\mathbf{R}^0_{S,j=n} \end{bmatrix} \begin{bmatrix} \hat{\mathbf{p}}_\mathbf{t} \\ \hat{\mathbf{p}}_\mathbf{s} \end{bmatrix} = \begin{bmatrix} \mathbf{r}^0_{S,j=1} & -\mathbf{r}^0_{T,j=1} \\ \vdots & \vdots \\ \mathbf{r}^0_{S,j=n} & -\mathbf{r}^0_{T,j=n} \end{bmatrix} \tag{3.14}$$

with $\hat{\mathbf{p}}(6\times 1) = \begin{bmatrix} \hat{\mathbf{p}}_\mathbf{t} & \hat{\mathbf{p}}_\mathbf{s} \end{bmatrix}^T$ consists of the local coordinates of P that satisfy Eq. 3.13. When $\hat{\mathbf{p}}$ represents the knee CoR, it can be calculated using the Moore Pseudo-inverse $\mathbf{Y}^+$ from Eq. 3.14. In the case of AoR estimation, $\hat{\mathbf{p}}$ referring to an arbitrary point located on the knee AoR, as well as its unit vector, can be obtained using the singular value decomposition $\mathbf{Y} = \mathbf{USV}^T$ as follows [192]:

$$\hat{\mathbf{p}} = \sum_{c=1}^{5} \frac{\mathbf{u}_c^T \mathbf{z} \mathbf{v}_c}{\sigma_c} \quad c = 1, ..., 6 \tag{3.15}$$

$$\mathbf{d}_t = \frac{\mathbf{v}_6(1:3)}{\| \mathbf{v}_6(1:3) \|} \quad \mathbf{d}_s = \frac{\mathbf{v}_6(4:6)}{\| \mathbf{v}_6(4:6) \|} \tag{3.16}$$

where $\mathbf{u}_c$ and $\mathbf{v}_c$ are the column vectors of index c of the $\mathbf{U}$ and $\mathbf{V}$ matrices, respectively. σ_c is the c^{th} singular value of the $\mathbf{S}$ matrix. $\mathbf{d_t}$ and $\mathbf{d_s}$ are the normalized direction vectors of the AoR relative to the thigh and shank local frames given by the last column of $\mathbf{V}$. Note that $\hat{\mathbf{p}}_\mathbf{t}$ and $\hat{\mathbf{p}}_\mathbf{s}$ must be orthogonalized w.r.t. $\mathbf{d_t}$ and $\mathbf{d_s}$ respectively in order to obtain a unique global and local representation of the required knee AoR in this case.

3.3 Biomechanical Model Identification

A biomechanical model requires the identification of its dynamic parameters (BSIPs) defined in section 2.2.2.2. How these parameters have been obtained in the literature were previously discussed in section 2.4.3. Following the works of Venture et al. [171, 113, 178, 175], an identification method has been developed in the current study using the linear property of the dynamic model w.r.t. the BSIPs to be identified. It requires joint kinematics and contact force measurements collected throughout exciting movements of the body segments of interest. The main aspects of this method are detailed hereafter. Section 3.3.1 reformulates the dynamic equations of motion into a linear identification model. Section 3.3.2 defines a minimal set of only identifiable parameters characterizing the dynamic model. Finally, the required full set of BSIPs is derived in section 3.3.3.

3.3.1 Linear Identification Model

Eq. 2.9, that expresses the inverse dynamics model of a floating base-system, may be represented as a linear function of the BSIPs to be identified [113], such as:

$$\begin{bmatrix} \mathbf{W}_w \\ \mathbf{W}_c \end{bmatrix} \mathbf{\Phi} = \begin{bmatrix} \mathbf{0} \\ \mathbf{\Gamma} \end{bmatrix} + \sum_{k=1}^{N_c} \begin{bmatrix} \mathbf{J}_{w_k}^T \\ \mathbf{J}_{c_k}^T \end{bmatrix} \mathbf{F}_k \tag{3.17}$$

where $\mathbf{W}_w$ ($6 \times 10N_L$) and $\mathbf{W}_c$ ($N_J \times 10N_L$) are known as the observation or regressor matrices of the base segment and of the N_L segments of the kinematic chains constituting the whole investigated system, respectively [113]. The vector of all standard inertial parameters $\mathbf{\Phi}$ ($10N_L \times 1$) gathers for each segment i the mass M_i, the 3D vector of the first moment of inertia $[MSX_i\ MSY_i\ MSZ_i]$ and the six components of the 3x3 inertia tensor $\mathbf{I}$=$[XX_i\ YY_i\ ZZ_i\ XY_i\ XZ_i\ YZ_i]$, respectively such that:

$$\begin{aligned} \mathbf{\Phi}_i &= \begin{bmatrix} M_i & MSX_i & MSY_i & MSZ_i & XX_i & YY_i & ZZ_i & XY_i & XZ_i & YZ_i \end{bmatrix}^T \\ \mathbf{\Phi} &= \begin{bmatrix} \mathbf{\Phi}_0^T & \mathbf{\Phi}_1^T & . & . & . & \mathbf{\Phi}_{N_L}^T \end{bmatrix}^T \end{aligned} \tag{3.18}$$

In the absence of joint torques measurements, such as in the case of the human body, only the upper part of Eq. 3.17, reformulated in Eq. 3.19, is considered in the identification process. Thus, the dynamometric measurements in Eq. 3.19 are the external wrenches $\mathbf{F}_k = \begin{bmatrix} F_{X_k} & F_{Y_k} & F_{Z_k} & M_{X_k} & M_{Y_k} & M_{Z_k} \end{bmatrix}^T$ measured at the contact points with the environment, of the model being investigated, and mapped into its base segment, as explained in Eq. 2.9, such as:

$$\mathbf{W}(\boldsymbol{\theta}_w, \dot{\boldsymbol{\theta}}_w, \ddot{\boldsymbol{\theta}}_w, \boldsymbol{\theta}, \dot{\boldsymbol{\theta}}, \ddot{\boldsymbol{\theta}}, \mathbf{L})\,\mathbf{\Phi} = \sum_{k=1}^{N_c} \mathbf{J}_{w_k}^T(\boldsymbol{\theta}) \mathbf{F}_k \tag{3.19}$$

The regressor matrix $\mathbf{W}$ is a non-linear function of the base and joint kinematics as well as geometrical parameters such as segments lengths. It can be obtained through the partial derivatives of the dynamometric measurements vector w.r.t. the standard inertial parameters vector. For each of the n measurements samples, $\mathbf{W}$ ($(N_F = 6n) \times 10N_L$) consists of six lines referring to the 3D measured forces and moments along the X, Y, and Z axes, respectively, as well as a column per each parameter of $\mathbf{\Phi}$. For instance, W_{ij} indicates how much the parameter j contributes to the dynamometric measurement i, such that:

$$\mathbf{W} = \begin{bmatrix} \frac{\partial F_{X_0}(1)}{\partial M_1} & \frac{\partial F_{X_0}(1)}{\partial MX_1} & \cdots & \frac{\partial F_{X_0}(1)}{\partial \Phi_{j=10N_L}} \\ \vdots & & & \vdots \\ \frac{\partial F_{X_0}(n)}{\partial M_1} & \frac{\partial F_{X_0}(n)}{\partial MX_1} & \cdots & \frac{\partial F_{X_0}(n)}{\partial \Phi_{j=10N_L}} \\ \vdots & & & \vdots \\ \frac{\partial M_{Z_0}(1)}{\partial M_1} & \frac{\partial M_{Z_0}(1)}{\partial MX_1} & \cdots & \frac{\partial M_{Z_0}(1)}{\partial \Phi_{j=10N_L}} \\ \vdots & & & \vdots \\ \frac{\partial M_{Z_0}(n)}{\partial M_1} & \frac{\partial M_{Z_0}(n)}{\partial MX_1} & \cdots & \frac{\partial M_{Z_0}(n)}{\partial \Phi_{j=10N_L}} \end{bmatrix} \tag{3.20}$$

In the current thesis, $\mathbf{W}$ is derived using Symoro+ (SYmbolic MOdelling of RObots) [67].

3.3.2 Minimal Base Parameters

Theoretically, for a full rank regressor matrix $\mathbf{W}$, Eq. 3.19 may be solved using a linear regression such as the least-square optimization. However, the dependencies of parameters in human/robot dynamic equations yield a defected rank of $\mathbf{W}$. This suggests some null columns and others that are linearly inter-dependent corresponding to standard inertial parameters with no or proportional effect on the dynamics, respectively. Even with using sufficiently exciting trajectories, not all of the $10N_L$ BSIPs gathered in $\mathbf{\Phi}$ contribute to the dynamics and consequently, not all of these parameters are identifiable using a simple least-square method [178]. To cope with this issue, a minimal set of linearly independent parameters, also known as base parameters, is derived from standard ones by eliminating those with no effect and by regrouping the other dependent ones. These are therefore the only identifiable parameters required to fully describe the dynamic model.

Particularly, base parameters are calculated by regrouping the linearly dependent columns of $\mathbf{W}$, which may be done numerically using a QR or a Singular Value Decomposition (SVD). Thus, Eq. 3.19 may be rewritten as follows:

$$\begin{bmatrix}\mathbf{W}_b & \mathbf{W}_d\end{bmatrix}\begin{bmatrix}\mathbf{\Phi}_b \\ \mathbf{\Phi}_d\end{bmatrix} = \sum_{k=1}^{N_c} \mathbf{J}_{w_k}^T(\mathbf{q})\mathbf{F}_k \qquad \mathbf{W}_d = \mathbf{W}_b\,\mathbf{C} \tag{3.21}$$

where $\mathbf{W}_b$ shows the regressor matrix formed by the linearly independent columns of $\mathbf{W}$ and $\mathbf{W}_d$ is formed by the remaining null and dependent ones, given that the sum of both matrices ranks is equal to the rank of $\mathbf{W}$. Similarly, the vectors $\mathbf{\Phi}_b$ $(N_B \times 1)$ and $\mathbf{\Phi}_d$ $((10N_L - N_B) \times 1)$ include standard parameters reordered according to the columns of $\mathbf{W}_b$ and $\mathbf{W}_d$, respectively. The combination of both vectors yields all standard parameters $\mathbf{\Phi}$ $(10N_L \times 1)$ to be identified at the end of the identification process. Given that $\mathbf{W}_b$ columns form a linearly independent base, $\mathbf{W}_d$ can be expressed linearly w.r.t. such base through a constant matrix $\mathbf{C}$. Thus, by replacing $\mathbf{W}_d$ in Eq. 3.21, a minimal identification model is obtained and is given by the Eq. 3.22 below. In the following, the vector of dynamometric measurements expressed in the base frame is denoted by $\bar{\mathbf{F}}$ $(N_F \times 1)$, such that:

$$\begin{aligned}\bar{\mathbf{F}} &= \mathbf{W}_b\mathbf{\Phi}_B + \rho \\ \mathbf{\Phi}_B &= \mathbf{\Phi}_b + \mathbf{C}\mathbf{\Phi}_d\end{aligned} \tag{3.22}$$

with $\mathbf{\Phi}_B$ $(N_B \times 1)$ is the vector of base parameters regrouping linearly the standard parameters and ρ $(N_F \times 1)$ is an error vector gathering the measurement noise and modelling errors. Note that $\mathbf{W}_b$, $\mathbf{W}_d$, and $\mathbf{C}$ matrices are not unique.

Assuming that the performed movements excite sufficiently all base parameters to be identified and yield a full rank regressor matrix $\mathbf{W}_b$, Eq. 3.22 may be solved using a standard least-square based method, such as:

$$\text{Find } \mathbf{\Phi}_B{}^* = \arg\min_{\mathbf{\Phi}_B} \| \bar{\mathbf{F}} - \mathbf{W}_b \mathbf{\Phi}_B \|_2^2 \tag{3.23}$$

However, due to ρ, the solution given by Eq. 3.27 might be biased. As shown by Gautier et al. [178], the quality of the base parameters estimation may be assessed through the calculation of the relative standard deviation for each identified parameter. Considering $\mathbf{W}_b$ to be deterministic and ρ to be a zero-mean Gaussian noise, the unbiased estimate of the standard deviation σ_ρ may be obtained as:

$$\sigma_\rho^2 = \frac{\| \bar{\mathbf{F}} - \mathbf{W}_b \mathbf{\Phi}_B \|^2}{N_F - N_B} \tag{3.24}$$

and the variance-covariance matrix of the least square estimation error is given by:

$$\mathbf{C}_{\mathbf{\Phi}_B} = \sigma_\rho^2 \, (\mathbf{W}_b^T \, \mathbf{W}_b)^{-1} \tag{3.25}$$

Thus, the standard deviation $\sigma_{\Phi_{Bi}}$ of the i^{th} base parameter as well as its relative standard deviation $\sigma_{\Phi_{Bi}}\%$ are calculated as follows:

$$\begin{aligned} \sigma_{\Phi_{Bi}} &= \sqrt{\mathbf{C}_{\mathbf{\Phi}_B}(i,i)} \\ \sigma_{\Phi_{Bi}}\% &= 100 \, \frac{\sigma_{\Phi_{Bi}}}{| \, \Phi_{Bi} \, |} \quad \text{for } | \, \Phi_{Bi} \, | \neq \, 0 \end{aligned} \tag{3.26}$$

Only identified parameters with a relative standard deviation lower than 10% are considered to be accurate enough. Since the external wrenches are expressed in different units and with different order of magnitude, it is recommended to use a weighted least-square method to improve the parameters estimation [178, 175]. A square weight matrix $\mathbf{M}$ is thus created by assigning to each component of $\bar{\mathbf{F}}$ a confidence factor inversely proportional to the associated standard deviation of the error calculated using Eq. 3.24. Doing so, $\mathbf{\Phi}_B$ may be calculated using a weighted Moore-Penrose pseudo-inverse, given as:

$$\begin{aligned} &\mathbf{\Phi}_B = \mathbf{W}_b^+ \bar{\mathbf{F}} \\ &\text{with} \\ &\mathbf{W}_b^+ = (\mathbf{W}_b^T \mathbf{M} \mathbf{W}_b)^{-1} \mathbf{M} \mathbf{W}_b^T \end{aligned} \tag{3.27}$$

3.3.3 Standard Parameters Identification

Not only the base parameters are required to be identified, but also the full vector of standard BSIPs $\mathbf{\Phi}$ that is needed to compute the forward dynamics as well as joint torques (see the lower parts of Eq. 2.9 and Eq. 3.17). However, some parameters fall in the null-space of the regressor matrix, which makes their identification not straightforward. Yet, several approaches have been proposed in the literature using a priori information as an initial guess to find parameters in the null-space, and to ensure their physical consistency [178, 193]. Indeed, due to either measurement noises or modelling errors, the identification methods may result in physically unfeasible solutions. BSIPs, however, represent physical quantities, which must always have meaningful values.

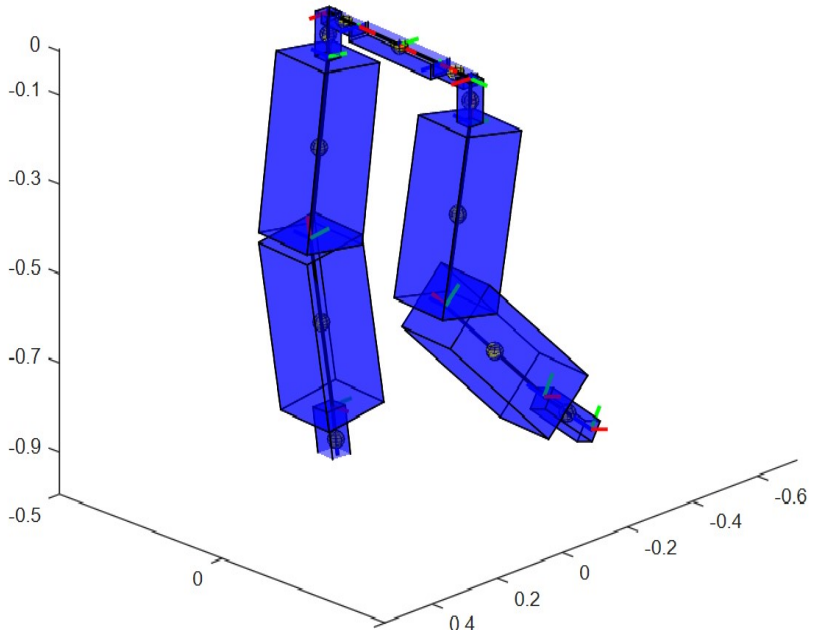

Fig. 3.8 Visual representation of a robot mechanical model with for each segment a specific oriented bounding box defined in its local frame, and the CoM position expressed in the global system of reference.

In this context, a constrained Quadratic Programming (QP) method together with a hybrid cost function allow a trade-off between the least-square fitting of the dynamometric measurements, and a feasible solution w.r.t. a user-supplied initial guess. In our case, the initial guess parameters are obtained from Dumas et al. [167] Anthropometric Tables (AT) for human and from the manufacturer Computer Aided Design (CAD) data for robot. The QP is thus formulated as:

$$\begin{aligned} \text{Find } \mathbf{\Phi}^* \in \quad & \min_{\mathbf{\Phi}} \| \bar{\mathbf{F}} - \bar{\mathbf{W}}\mathbf{\Phi} \|_2^2 + \| \mathbf{\Phi}_{CAD} - \mathbf{\Phi} \|_2^2 \\ \text{subject to} \quad & \\ & M_i \geq 0 \\ & CoM_{ij}^- \leq CoM_{ij} \leq CoM_{ij}^+ \\ & \mathbf{v}_j^T \mathbf{I}_i \mathbf{v}_j \geq \epsilon \\ & \text{with} \quad i = 1, ..., N_L \quad j = x, y, z \end{aligned} \tag{3.28}$$

where $\mathbf{\Phi}_{REF}$ $(10N_S \times 1)$ refers to the BSIPs values obtained from CAD or AT. This QP also guarantees the physical consistency of the identified BSIPs through additional constraints. Three primary constraints are implemented: segments masses to have positive values ($M_i \geq 0$), CoM to be inside realistic body segments volume, and segments inertia matrices $\mathbf{I}_i$ to be positive defined. The latter is used from [155, 175, 194], which results in the linear inequality given below:

$$\begin{bmatrix} v_{xj}^2 & 2v_{xj}v_{yj} & 2v_{xj}v_{zj} & v_{yj}^2 & 2v_{yj}v_{zj} & v_{zj}^2 \end{bmatrix} \begin{bmatrix} XX \\ XY \\ XZ \\ YY \\ YZ \\ ZZ \end{bmatrix} \geq \epsilon \tag{3.29}$$

where $\mathbf{v}_j$=$[v_{xj}\ v_{yj}\ v_{zj}]^T$ is a random vector supposed uniformly distributed over the unit sphere and ϵ is a positive tolerance set to 10^{-3}. To constrain the position of body segments CoMs inside a realistic given volume, CoM_{ij}^- and CoM_{ij}^+ are derived based on AT/CAD data and are assumed as the lower and upper bounds of a specific oriented bounding box attached to the i^{th} segment and defined in its local corresponding frame, respectively (see Fig. 3.8).

3.4 Joint Kinematics Estimation Using Affordable Sensors

For BSIPs identification, as well as for a wide range of applications (see section 2.1), the joint kinematics need to be estimated accurately. Despite the fact that the proposed system is affordable, light wight, easy to use and portable, several limitations should be taken into account. Although the AR markers data are drift-free and provide pose measurements that can be used to calibrate IMU sensors locations on body segments, these markers are sensitive to image blur and occlusion. Moreover, their accuracy might be affected by numerous factors such as marker's size, distance from the camera, camera calibration and properties,

i.e., brightness, exposure, etc. On the other hand, IMUs do not suffer from occlusion but have some limitations related to non-linear integrational drift and IMU-to-body calibration issues in the absence of pose data, but do not suffer from occlusion. To test the effect of IMU drift, data from one IMU sensor (MPU 6050) was statically recorded for a period of $t = 23s$. Fig. 3.9 depicts the sensor 3D pose, obtained by integrating and double integrating the measured angular velocities and linear accelerations, respectively. Within 23s only, the sensor's orientation and position highly drifted to -1.5rad around the Y-axis and 40cm along the X and Y-axes, respectively.

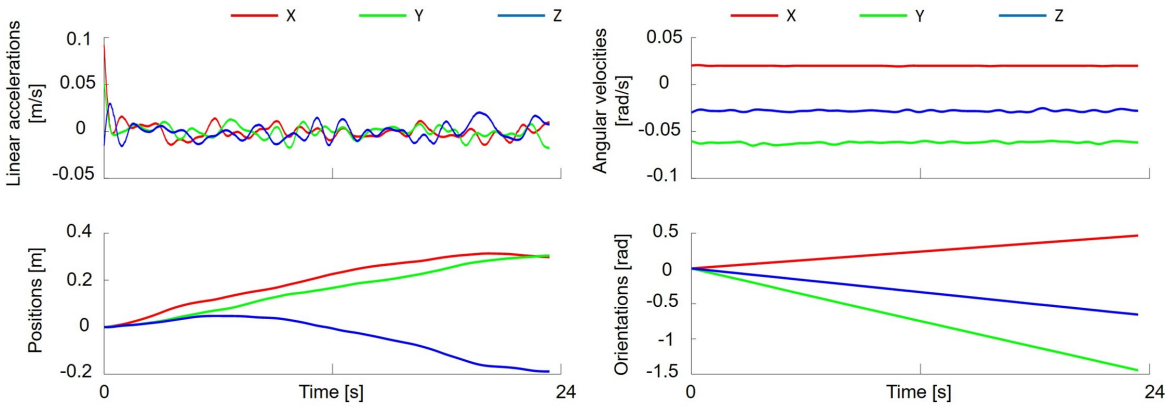

Fig. 3.9 Drifting orientations and drifting positions, when integrating the measurements of an IMU sensor placed in a static pose.

When dealing with such affordable sensors, adaptive filters, such as EKF and UKF, have shown in the literature their efficiency in reducing the sensor's noise influence (section 2.4.2). As mentioned in [153], UKF performs slightly better than EKF for human motion estimation application but at a large computational cost. Fusing all VIMUs redundant data using a CEKF, a biomechanical model of the human body, together with the appropriate tuning of the CEKF parameters referring to each measurement, will allow improving the tracking accuracy of the proposed system while estimating directly the required joint kinematics. Providing the sensors-specific (see section 3.1) and the subject-specific biomechanical model (see section 3.2) calibrations, the sensors calibrated data, body segments lengths, as well as the local pose of each sensor w.r.t. its corresponding segment anatomical frame, are required as inputs to the CEKF (see Fig. 3.1). Section 3.4.1 provides a brief theoretical insight into the CEKF formulation, whereas, the implementation referring to the different case studies is presented in the following chapters.

3.4.1 Constrained Extended Kalman Filter

In light of the above, a CEKF is used to estimate the human body joint kinematics. The CEKF is able to handle efficiently uncertainties in input measurements through an appropriate fusion of VIMUs data. It is worthy noting also that the CEKF has a relatively low computational cost, which makes it suitable for real-time applications. For a proper performance, the CEKF requires the input sensors to have a Gaussian noise distribution. It is the case of the IMU noise when the sensor is stationary, as demonstrated in several studies [195, 196]. For instance, the random noise of the retained IMU in this thesis, i.e., MPU 6050, has been shown to be a white Gaussian noise in [195, 197]. Although, further errors, not necessarily Gaussian distributed as assumed by the CEKF, may appear during dynamic motion [198], several studies have successfully tracked pose while approximating the IMU noise as white Gaussian [135, 199]. This section along with Fig. 3.10 highlight the flow of the proposed CEKF algorithm that has been used in this thesis.

3.4.1.1 The Filter Algorithm

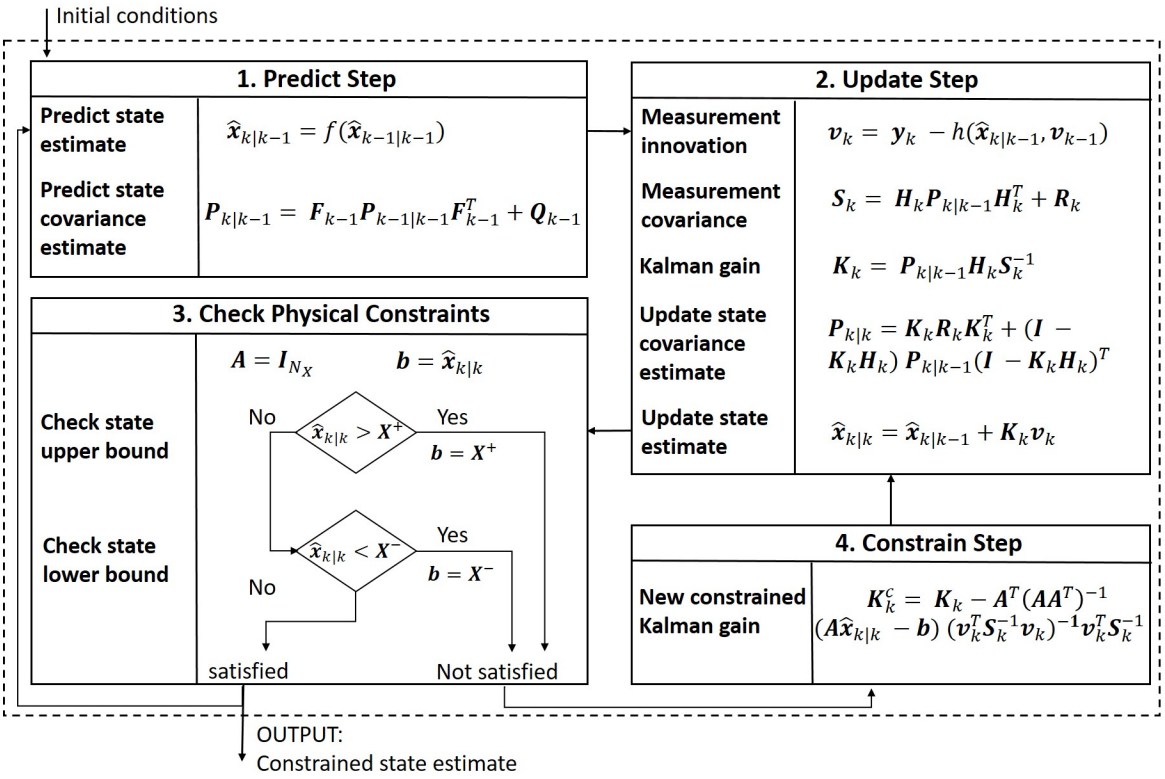

Fig. 3.10 The CEKF framework.

The EKF is a common recursive sensor fusion algorithm used to estimate a non-linear system's state given noisy measurements, where the noise is still assumed as zero-mean Gaussian. The non-linear system models are approximated through a first-order Taylor-series expansion that is evaluated at each time-step around the current state estimate. This suggests the system models to be differentiable or to be represented using a discrete approximation.

The goal of the EKF is to ensure the best estimate of the system's state that fits the measured data in a least-square sense. In this thesis, human motion kinematic analysis suggests the knowledge of state variables for each joint, including the position, velocity, and acceleration of each segment. The measurement vector is composed of all VIMUs data.

The current state $\mathbf{x}_k$ ($N_X \times 1$) and the measurement vector $\mathbf{y}_k$ ($N_Y \times 1$), at time-step k, are governed by two prediction and update steps given by the following equations:

$$\begin{aligned} \mathbf{x}_k &= f(\mathbf{x}_{k-1}) + \mathbf{w}_{k-1} \\ \mathbf{y}_k &= h(\mathbf{x}_k) + \mathbf{v}_k \end{aligned} \tag{3.30}$$

where f and h denote the non-linear process and measurement models, respectively. $\mathbf{w}$ and $\mathbf{v}$ represent the process and measurement noise, assumed as zero-mean Gaussian with known covariance matrices $\mathbf{Q}_k$ ($N_X \times N_X$) and $\mathbf{R}_k$ ($N_Y \times N_Y$), respectively. In the following, a discrete formalization of the EKF recursion is presented.

Prediction Phase The process model f, also known as the dynamic or evolution model, describes recursively the evolution of state dynamics. It allows predicting the state mean $\hat{\mathbf{x}}_{k|k-1}$ and error covariance matrix $\mathbf{P}_{k|k-1}$ at the current time step k from their previous estimates at time step $k-1$, such as:

$$\begin{aligned} \hat{\mathbf{x}}_{k|k-1} &= f(\hat{\mathbf{x}}_{k-1|k-1}) \\ \mathbf{P}_{k|k-1} &= \mathbf{F}_{k-1}\mathbf{P}_{k-1|k-1}\mathbf{F}_{k-1}^T + \mathbf{Q}_{k-1} \end{aligned} \tag{3.31}$$

where $\mathbf{F}$ is the process model Jacobian calculated symbolically relatively to the state vector.

Measurement Update h provides the measurement vector as a function of the state vector. Fusing all VIMUs data suggests that all measured quantities contribute to the state variables, i.e., joint trajectories, to be estimated. Given the predicted state, at each time step, a new measurement $\mathbf{y}_k$ can be used to calculate a weighted difference $\mathbf{v}_k$ between the measurement vector and the predicted one through the measurement model. The Kalman gain $\mathbf{K}_k$ and the

state vector are then updated at each time step as in Fig. 3.10 and Eq. 3.32, respectively:

$$\begin{aligned} \mathbf{v}_k &= \mathbf{y}_k - h(\hat{\mathbf{x}}_{k|k-1}, \mathbf{v}_{k-1}) \\ \mathbf{S}_k &= \mathbf{H}_k \mathbf{P}_{k|k-1} \mathbf{H}_k^T + \mathbf{R}_k \\ \mathbf{K}_k &= \mathbf{P}_{k|k-1} \mathbf{H}_k \\ \hat{\mathbf{x}}_{k|k} &= \hat{\mathbf{x}}_{k|k-1} + \mathbf{K}_k \mathbf{v}_k \end{aligned} \tag{3.32}$$

where **S** is the measurement covariance matrix, and **H** is the measurement model Jacobian calculated symbolically relatively to the state vector.

Satisfying Biomechanical Constraints Following the EKF prediction and measurement update steps, above, the body joints may have become dislocated, or joint angles expand beyond their feasible range [136]. In an attempt to reduce the drift effect and estimate accurate and realistic joint trajectories, biomechanical constraints are explicitly considered within the EKF.

First, the use of a kinematic model consisting in multiple rigid body segments of fixed lengths and joints constraints, i.e., hinge, spherical, allows to avoid joint dislocations that may considerably affect the joint angle estimates, as well as to reduce the influence of STA. For instance, a knee hinge joint with a single flexion/extension DoF prevents the drift from occurring along its 3D position, as well as about unfeasible abduction/adduction and internal/external rotation.

To further ensure a biomechanically-realistic RoM of human body joints, a method similar to the one presented by Gupta et al. [200] allows implementing the following constraints:

$$\mathbf{A}\hat{\mathbf{x}}_k = \mathbf{d} \tag{3.33}$$

where **A** $(s \times N_X)$ is a constant known matrix (i.e., identity matrix), $s \leq N_X$ is the number of given constraints, and **d** $(s \times N_X)$ is the constraints vector, i.e., upper or lower-limbs feasible RoM constraints, which must be satisfied by the updated state vector. At each time step, a Kalman gain and state update are computed based on Eq. 3.32. The elements of the updated state vector are checked to be within their constraint limits. Then, if one element of the state vector is not within its limits, a vector of constraints **d** is created by replacing the corresponding state variable with its appropriate upper or lower bound. Using the constraints vector and the updated state vector, a new optimal Kalman gain is then computed according to Eq. 3.34 [200]:

$$\mathbf{K}_k^c = \mathbf{K}_k - \mathbf{A}^T(\mathbf{A}\mathbf{A}^T)^{-1}(\mathbf{A}\hat{\mathbf{x}}_{k|k} - \mathbf{d})(\mathbf{v}_k^T \mathbf{S}_k^{-1} \mathbf{v}_k)^{-1} \mathbf{v}_k^T \mathbf{S}_k^{-1} \tag{3.34}$$

Finally, the new updated state estimate is re-calculated using the new Kalman gain and Eq. 3.32, such that it lies within its constrained range.

3.4.1.2 The CEKF Parameters Tuning

The use of CEKF requires optimal parameters tuning of the process noise covariance matrix **Q**, the measurement noise covariance matrix **R**, and the initial condition of the state covariance matrix **P** to ensure an appropriate fusion of the sensors data while maximizing stability and convergence rates over a given trial. The tuning of these matrices, however, is sensitive. In general, a large value indicates a lack of trust, whereas a small value indicates a good trust in the process or measurement parameter. For instance, a too small measurement noise suggests that the measurement model cannot adequately account for the amount of noise that is in the sensor data, causing integrational drift. If it is too large, motion data may be lost as it is being discarded by the CEKF as noise.

In general, the initial **P** is set to the identity matrix to give the same influence to all joints to be estimated. Whereas, **R** can be adjusted based on the error model of each sensor, i.e., IMU and AR markers. However, the process model is not directly observable and there is no real consensus in the literature on how to adjust the parameters of its noise covariance matrix **Q**.

In this study, the CEKF parameters tuning has been conducted either empirically (section 4.1) or automatically using an optimization process (section 4.2). Once adjusted, these parameters are kept constant throughout the studied application.

3.5 Reference Joint Kinematics Estimation

To validate the proposed affordable VIMUs-based system, the CEKF-based joint angles, derived based on the previous section, are compared with those obtained using a gold standard SS. The reference joint trajectories are calculated using stereophotogrammetric data together with a state-of-the-art MKO [65, 79].

MKO is an inverse kinematic solution targeting an optimal pose of a multi-body model that best fits the motion capture data. It requires a predefined kinematic model of the human body so that it simultaneously calculates all body segments poses while satisfying multi-joints constraints in a unique least-square optimization aiming at compensating for STA. Usually, a minimum of three retro-reflective markers is used to define the 3D pose of each body segment, although it was shown possible to reduce markers sets per segment [79]. MKO is then based on the minimization of the sum of squared distances between measured and model-derived skin-markers trajectories which are governed by some rigid body and kinematic constraints

[79]. Providing the body segments lengths and the local pose of each marker relative to its segment anatomical frame, joint angles may be calculated using a non-linear constrained optimization, such as the sequential quadratic programming algorithm [201].

3.6 Conclusion

This chapter introduces the fundamental bases used in the following chapters. It presents a new affordable, portable, and user-friendly MCS together with a dynamic identification pipeline for human/robot joint kinematics and BSIPs estimation, respectively. The kinematic data are collected using new VIMUs sensors measuring inertial data from IMUs sensors as well as visual information from AR markers and an affordable RGB camera. All data are fused into a CEKF taking into account the kinematic model of the human body and its limitation to estimate feasible and straightforward joint kinematics while reducing the effect of each sensor inaccuracies. The system is also making use of a new practical calibration method, which does not require any external equipment while remaining very affordable. The system detailed implementation and validation are described in the following chapters.

Chapter 4

Human Body Kinematics Assessment during Activities of Daily Living

Stroke, spinal cord injury, or age-related neurological deficiencies may considerably impair patients/elders active Range of Motion (RoM), thus restrict their mobility to perform Activities of Daily Living (ADL). Assessing human motion during ADL is therefore of great interest to characterize movement disorders. For instance, gait is considered as the most common ADL used in this context.

The Motion Capture System (MCS) framework introduced in chapter 3 is experimentally validated in this chapter. Two different prototypes of a VIMUs-based MCS have been developed and used to track upper and lower-limbs movements of multiple subjects performing several ADL movements. Experimental validation is then conducted by comparison of the obtained joint kinematics w.r.t. those obtained using a gold standard Stereophotogrammetric System (SS).

More specifically, the study developed in section 4.1 aims at quantifying upper-limbs joint kinematics using a setup similar to the one used during the clinical evaluation of post-stroke patients performing ADL [202]. Results of this study were recently published in the IEEE Transactions on Automation Science and Engineering [15]. Section 4.2 studies the possibility of tracking accurately full lower-limbs gait kinematics using a reduced sensors-count configuration [17].

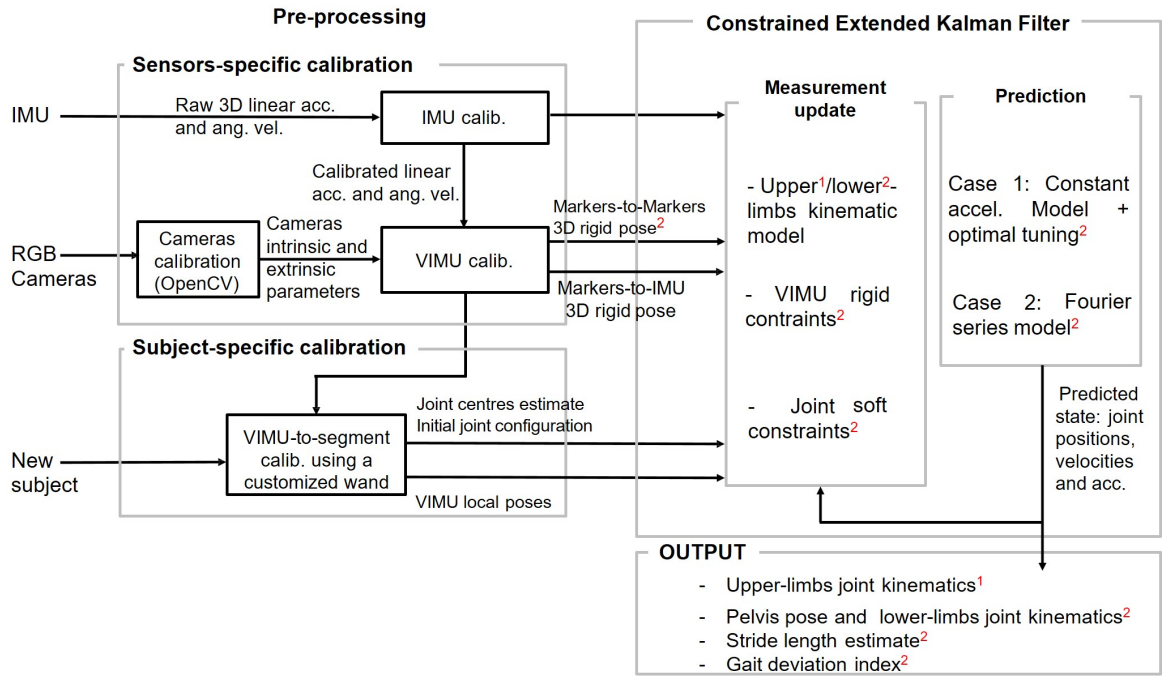

Fig. 4.1 An overview of the proposed system's framework used to estimate upper/lower-limbs joint kinematics with indexes 1 and 2, respectively.

4.1 Upper-Limbs Kinematics Estimation: Application to Rehabilitation Exercises

Upper-limbs physical and functional impairments following a stroke may directly affect patients' quality of life due to their inability to achieve primary ADL, such as eating, dressing and other tasks [3]. Upper-limbs mobility can be improved through repetitive rehabilitation exercises of the patients' affected limbs [203], [4]. To quantify the clinical progress during a rehabilitation program, a functional mobility assessment is usually conducted under the supervision of a therapist.

Several functional mobility assessment indexes, such as the Modified Frenchay Test (MFT) [202] (see section 4.1.1), have been proposed in the literature. They are usually targetting several ADL, which are visually observed and rated by one or more clinicians [202]. However, such assessment remains qualitative (refer to section 2.2.1), so that inter- and intra-clinician variability can be large and reproducibility can be challenging to achieve [4]. To this end, a MCS, such as the VIMUs-based system proposed in chapter 3, would help supporting clinicians diagnosis through a quantitative and objective assessment of the patients' motion [4].

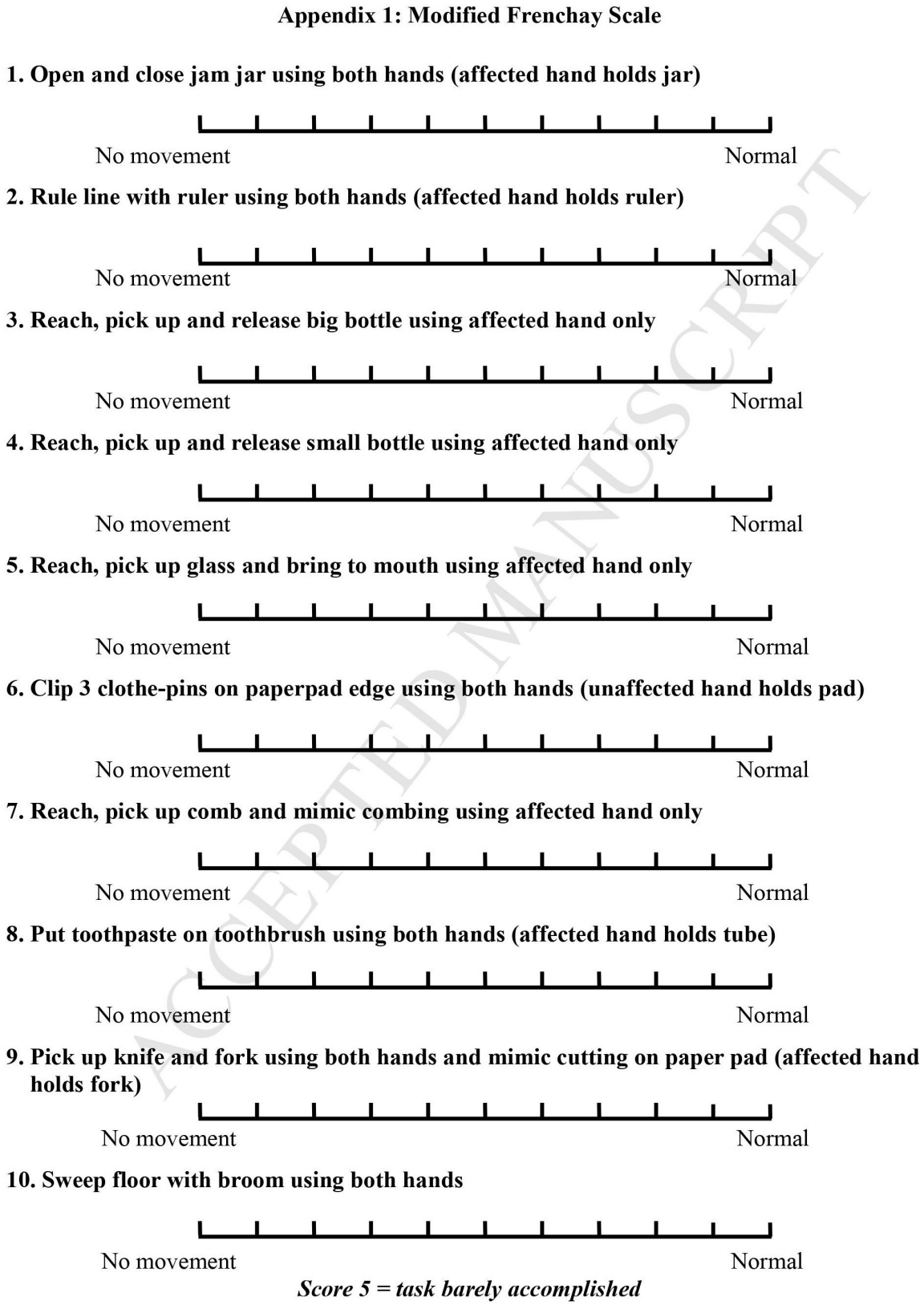

Fig. 4.2 The MFT scale from [202].

In this section, we propose:

- The development of a new and very affordable VIMUs-based MCS that estimates seven upper-limbs joint angles: shoulder/wrist flexion/extension, abduction/adduction, internal/external rotation, and elbow flexion/extension. It is based on the framework developed in chapter 3, including a practical and time-efficient system's calibration.
- The system's validation using a gold standard SS while tracking arm motions of nine healthy subjects during six daily rehabilitation tasks based on the MFT.

4.1.1 The Modified Frenchay Test

The MFT [202] is a modified version of the original Frenchay Arm Test [204] used to assess active upper-limbs function in hemiparetic patients. It consists in videotaping patients while performing ten upper-limbs ADL, such as opening and closing a jam jar, picking up a fork and a knife and mimicking cutting (see Fig. 4.2). Each task is visually rated from 0, i.e., no movement, to 10, i.e., normal movement, by one or more independent clinicians. Whereas rate 5 corresponds to a task that was barely achieved by the patient.

4.1.2 Upper-limbs Joint Kinematics Estimation Framework

This section uses the framework developed in chapter 3 and described in Fig. 4.1 for upper-limbs joint kinematics estimation. Prior to data recording, an independent and sensor-specific calibration is performed offline and only once for each of the affordable sensors (RGB camera, IMU sensors, and IMU-to-AR marker rigid transformation (VIMU calibration)). Then for each subject, a static wand-based calibration is conducted to locate each VIMU sensor on its corresponding segment. To compensate for each sensor inaccuracies, all measured data are fused using a CEKF and an upper-limbs mechanical model. This allows obtaining physiologically constrained estimates of the upper-limbs joint angles while improving the system's robustness w.r.t. drift.

4.1.2.1 Upper-Limbs Mechanical Model

The mechanical model, depicted in Fig. 4.3, relates the output of three VIMU sensors to the arm joint kinematics through the calculation of the Forward Kinematics Model (FKM). It consists of $N_L = 2$ rigid segments articulated with $N_J = 7$ revolute joints describing the shoulder (ball joint), the wrist (ball joint) and the elbow (hinge joint) motion. The FKM (Eq. 2.2), which is a function of the N_J joint angles, of the N_L segment lengths, and of each VIMU

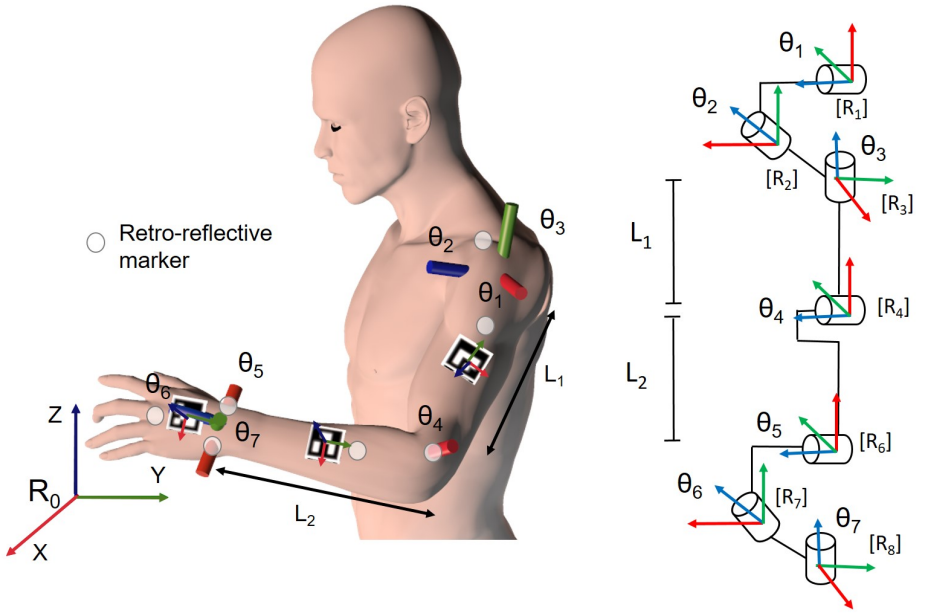

Fig. 4.3 Upper-limbs mechanical model composed of $N_L = 2$ segments and $N_J = 7$ DoFs.

local pose in its corresponding segment, is calculated using the Modified Denavit Hartenberg (MDH) convention (see section 2.2.2.1) [67]. It is used to estimate N_J joint angles simultaneously, making use of the intrinsic constraints of the retained upper-limbs kinematics structure.

Three local frames are used to represent the three VIMUs sensors assumed rigidly attached to the upper arm, forearm, and hand segments. The FKM allows obtaining the transformation matrices between the global system of reference R_0, expressed at the trunk level, and each of these frames. The VIMUs measured 3D poses expressed in R_0, $\mathbf{P}_s^0$, can thus be calculated based on these transformation matrices (see Eq. 2.1 and 2.2). $\mathbf{P}_s^0$ is composed of (3×1) position vector $\mathbf{r}_s^0$ and of (3×3) rotation matrix $\mathbf{R}_s^0$ representing the VIMUs tracked orientation in the global reference frame. To avoid gimbal lock and to use an efficient compact representation of 3D orientation, the matrices $\mathbf{R}_s^0$ are converted into the (4×1) quaternion vectors $\mathbf{q}_s^0$. For details on how to convert between rotation matrix and quaternion representations, the reader can refer to [205]. On the other hand, the FKM first (see Eq. 2.3) and second derivatives are calculated such that the VIMUs 3D angular velocities $\mathbf{\Omega}_s^s$ and 3D linear accelerations $\mathbf{a}_s^s$, measured in the sensors local frames, can be estimated:

$$\begin{aligned} \mathbf{P}_s^0 &= FKM(\boldsymbol{\theta}) \\ \mathbf{q}_s^0 &= fct(\mathbf{R}_s^0) \\ \begin{bmatrix} \mathbf{v}_s^s \\ \boldsymbol{\Omega}_s^s \end{bmatrix} &= (\mathbf{R}_s^0)^T \mathbf{J}(\boldsymbol{\theta})\dot{\boldsymbol{\theta}} \\ \begin{bmatrix} \mathbf{a}_s^s \\ \dot{\boldsymbol{\Omega}}_s^s \end{bmatrix} &= (\mathbf{R}_s^0)^T (\mathbf{J}(\boldsymbol{\theta})\ddot{\boldsymbol{\theta}} + \dot{\mathbf{J}}(\boldsymbol{\theta})\dot{\boldsymbol{\theta}}) + \begin{bmatrix} \mathbf{b}_a \\ \mathbf{0}_{3x1} \end{bmatrix} \end{aligned} \tag{4.1}$$

where $\boldsymbol{\theta}$, $\dot{\boldsymbol{\theta}}$, $\ddot{\boldsymbol{\theta}}$ refer to the $(N_J \times 1)$ joints positions, velocities and accelerations vectors, respectively. $\mathbf{J}$ (see Eq.) is the $(6 \times j)$ Jacobian matrix with $j \in \{3,4,7\}$ for shoulder, elbow and wrist sensors, respectively. $[\mathbf{v}_s^s \; \boldsymbol{\Omega}_s^s]^T$ is composed of (3×1) linear and angular velocity vectors and $[\mathbf{a}_s^s \; \dot{\boldsymbol{\Omega}}_s^s]^T$ is composed of (3×1) linear and angular acceleration vectors referring to each VIMU sensor. $\mathbf{b}_a$ denotes a (3×1) acceleration bias vector (see section 4.1.2.3). Eq. 4.1, providing all VIMUs measured data as a function of the joint kinematics to be estimated, is then used as the CEKF measurement model in section 4.1.2.3.

4.1.2.2 Pre-Calibration

The proposed framework requires two types of calibrations:

- Calibration of the sensors, which needs to be performed once. First, the IMUs and the camera are calibrated according to sections 3.1.1 and 3.1.2, respectively. Then, the marker-to-IMU rigid transformation, within each VIMU, is estimated from section 3.1.3.

- The local poses of all three upper arm, forearm, and hand sensors are calibrated w.r.t. their corresponding segments anatomical frames. This calibration is required to relate the sensors' measurements to the joint kinematics to be estimated. This calibration process is subject-specific and has to be performed once for each subject.

The latter was performed using the static wand-based method developed in section 3.2.1. Note that if the VIMUs sensors locations on their respective segments are modified, this calibration process has to be repeated. Starting from any upper-limbs static posture, anatomical landmarks were pin-pointed using the dedicated marker-based calibration wand (see section 3.2.1 and Fig. 4.4). Seven anatomical landmarks were pin-pointed: right and left AC, middle CLAV, MHE, LHE, US, and RS (see Fig. 2.5 for the definition of anatomical landmarks). The first three landmarks were used to compute the initial trunk's pose. Since no sensor was used to track its free movement, the trunk was assumed as a fixed reference segment during the rest of the experiment. The elbow and wrist joint centers positions were

determined using linear regression equations (see section 3.2.1). The shoulder joint center is supposed located vertically under the AC by an offset [206]. This offset is estimated as a percentage of the segment's length formed by the left and right AC positions [206]. Then, arm (L_1) and forearm (L_2) segment lengths were computed as the distance between the shoulder-elbow and the elbow-wrist joint centers positions, respectively. Based on these positions, the initial arm joint configuration could be calculated analytically from the inverse geometric model [67]. Meanwhile, the absolute 3D pose of each VIMU sensor was tracked synchronously in the global system of reference. Thus, its local pose w.r.t. its corresponding segment's frame could be computed.

All measurements were collected in the global system of reference R_0 defined by a dedicated AR marker (see section 3.1.2.1 and Fig. 4.5).

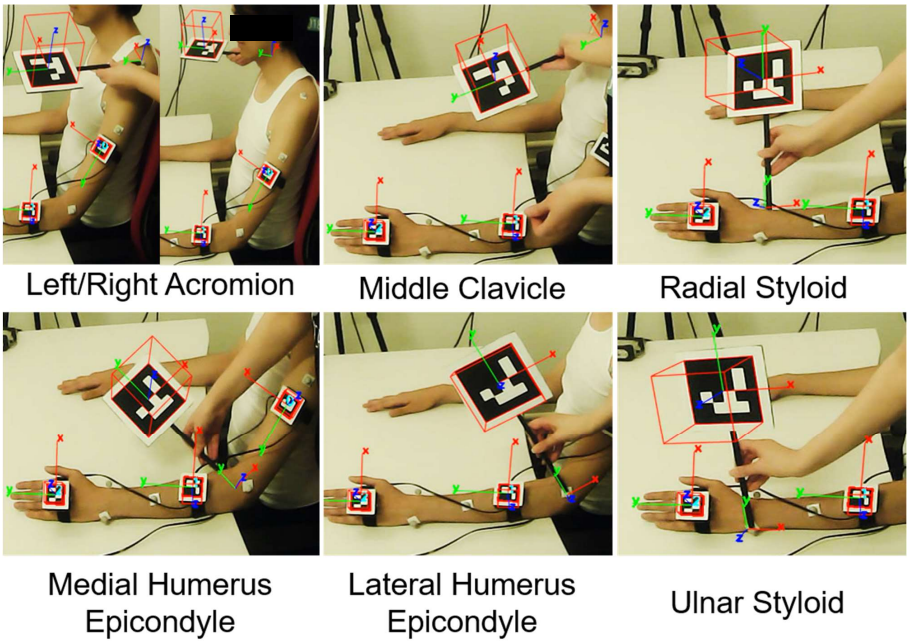

Fig. 4.4 Static wand-based calibration method consisting in pin-pointing seven anatomical landmarks of the upper-limbs.

4.1.2.3 Constrained Extended Kalman Filter

Once collected, all VIMUs data were fused using the CEKF framework described in section 3.4, along with the upper-limbs mechanical model described in section 4.1.2.1. As previously stated, the goal of the CEKF is to provide the best estimate of the state vector $\mathbf{x}_k$, at each time step k, by minimizing the least-square difference between VIMUs measurements and their model-based estimate. In the case of this study, $\mathbf{x}_k$ ($(N_X = 3N_J + 3N_S) \times 1$) gathers the

unknown position θ, velocity $\dot{\theta}$, and acceleration $\ddot{\theta}$ of each joint i (see Eq. 4.2). $\mathbf{b}_a\,(3N_S \times 1) = [b_{ix}\ b_{iy}\ b_{iz}]^T$, $i = 1,..,N_S$, refers to a vector of IMU random acceleration bias added to the measured accelerations (see Eq. 4.1) and N_S is the number of VIMUs sensors. The use of constant acceleration bias was shown to reduce the effect of drift and to increase the tracking accuracy [109]. We should note that the gyroscopes random drift was neglected due to the fact that in this particular case, it simply increased the state vector dimension without improving the accuracy of joint angle estimates.

$$\begin{aligned} \mathbf{x}_{i,k} = [\theta_{i,k} \quad \dot{\theta}_{i,k} \quad \ddot{\theta}_{i,k} \quad \mathbf{b}_{a,k}]^T \\ \text{with} \quad i = 1,...,N_J \end{aligned} \tag{4.2}$$

Process Model The process model f, introduced by Eq. 3.30, describes the evolution of each state variable. Theoretically, for the best performance of the CEKF, it is important to have an accurate and realistic model of the evolution of each state variable. Since it is not straightforward to model the evolution of upper-limbs joints accurately, f was assumed as a regular constant acceleration model, which is commonly used in the literature [207]. The joint positions and velocities are therefore assumed to be evolving linearly while the joint acceleration and the other parameters remain constant, such as:

$$\mathbf{x}_k = \begin{bmatrix} \begin{bmatrix} 1 & \Delta t & \frac{\Delta t^2}{2} \\ 0 & 1 & \Delta t \\ 0 & 0 & 1 \end{bmatrix}_{3N_J \times 3N_J} & \mathbf{0}_{3N_J \times 3N_S} \\ \mathbf{0}_{3N_S \times 3N_S} & \mathbf{I_d}_{3N_S \times 3N_S} \end{bmatrix} \mathbf{x}_{k-1} \tag{4.3}$$

where Δt is the sampling time, $\mathbf{0}$ and $\mathbf{I_d}$ are the null and identity matrices, respectively.

Measurement Model The measurement model h, introduced by Eq. 3.30, is calculated symbolically based on Eq. [67]. It allows estimating the measurement vector $\mathbf{y}_k$ $(N_Y \times 1)$ given the state vector value. When all of the sensors are included, the measurement vector at each time step k gathers the VIMUs 3D positions, linear accelerations, angular velocities, as well as quaternions, such as:

$$\mathbf{y}_k = [\mathbf{r}_s^0 \quad \mathbf{a}_s^s \quad \mathbf{\Omega}_s^s \quad \mathbf{q}_s^0]^T \tag{4.4}$$

with $N_Y = (3+3+3+4) \times N_S$.

Parameters Tuning According to section 3.4.1.2, the proposed CEKF requires the tuning of the following elements: the initial state vector value $\hat{\mathbf{x}}_0$, as well as the initial estimation of

the error covariance matrix $\mathbf{P}_0$, the process noise covariance matrix $\mathbf{Q}$ and the measurement noise covariance matrix $\mathbf{R}$. The values of $\hat{\mathbf{x}}_0$ and $\mathbf{P}_0$ have been shown to mainly affect the initial part of the estimation [208]. Thus, $\hat{\mathbf{x}}_0$ was set with the result of the inverse geometric model calculated from the AR markers data collected at the first sample of time. $\mathbf{P}_0$ was set equal to the identity matrix giving the same influence to all joints.

The parameters of the measurement noise covariance matrix $\mathbf{R}$ can be adjusted based on the error model of each sensor. The proposed CEKF is multi-modal, thus multiple measurement noise parameters are to be adjusted using each of the AR marker and IMU sensor's noise. Regarding IMU data, $\mathbf{R}$ parameters were set based on the standard deviation obtained when the sensor was in a static position for several minutes. For the AR markers, a dedicated test was conducted to compare the accuracy of AR markers w.r.t. retro-reflective markers poses. Thus, the accuracy of the 3D pose estimate of an AR marker located on the hand was assessed using a SS while performing the investigated tasks in this study (see Fig. 4.7). Three retro-reflective markers were placed on the side of the VIMU sensor to create a frame. To be able to compare this frame pose with the one provided by the AR marker, both systems global reference frames were first aligned by solving a least square problem as shown in [209]. A comparison of the estimated 3D position and orientation showed average RMSDs of 7±1.8mm and 2.8±1.5deg, respectively. Thus, the corresponding noise parameters in $\mathbf{R}$ were set with values of the same order of magnitude.

On the other hand, the tuning of $\mathbf{Q}$ is more challenging. As stated earlier, the process model is assumed as a constant acceleration model that is intrinsically inaccurate in human motion. The unmodelled changes in the joint velocities and accelerations would lead to estimation errors that are taken into account through the process noise. These errors are expected to be more significant at higher speeds. However, rehabilitation tasks are usually performed at slow to average speeds. Moreover, the method proposed by Cerveri et al. [207] was used, which consists in tuning the process noise as a function of the main frequency content of the human movement. In the particular case of the investigated tasks, the maximum frequency of the performed motion was arbitrarily set. As a result, and similarly to Cerveri et al. [207], $\mathbf{Q}$ elements related to the joint velocities and accelerations evolution were set constant to 10^3 for all joints. These values were selected to be large enough to indicate a lack of trust in the estimation of these variables due to the use of the linear assumption model.

Finally, the resulting parameters were held constant for all subjects and tasks.

4.1.3 Experimental Setup

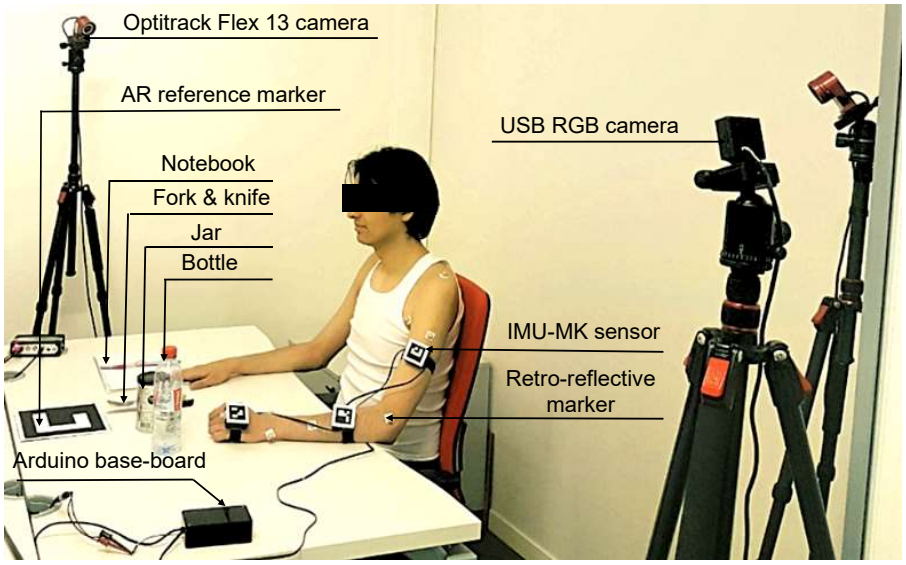

Fig. 4.5 Experimental setup used for the proposed system validation.

4.1.3.1 System Hardware Design

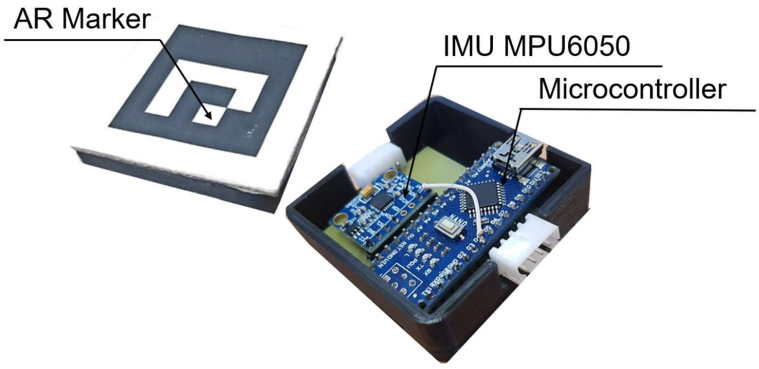

Fig. 4.6 A VIMU sensor first prototype.

The first prototype of VIMU-based MCS was designed to be compact, easy-to-use, and genuinely affordable with an overall price around 40€. It consists of three VIMUs sensors wired to each other, and to a master microcontroller that sends all three sensors inertial data to a host computer at a maximum rate of 150Hz. The proposed VIMU is based on one MPU-6050 (0.9€, Invensense) IMU embedding a 3D gyroscope and a 3D accelerometer.

Each IMU was associated with a microcontroller (Atmel ATmega328, 2.4€) collecting and transferring its data to the master one.

Besides, a 4x4cm square AR marker was fixed on the top of the 3D printed IMU enclosure, measuring 4x4x2cm and weighing 37g (see Fig. 4.6). AR markers data were detected using a standard 60Hz high-definition RGB USB camera (30€, ELP, USBFHD01) set up on a tripod to visualize the whole motion scene (see Fig. 4.5).

All VIMUs data were collected and recorded at a frequency of 54Hz using a custom software developed in C++.

4.1.3.2 Experiments

The proposed affordable system was validated w.r.t. a gold standard SS (7 flex 13 cameras, Optitrack). Three VIMUs sensors were attached to the upper arm, the forearm, and the hand segments, respectively (see Fig. 4.5). The estimation of upper-limbs joint kinematics was investigated in two cases: first, using all three VIMUs data; and second, using the data of the hand VIMU only (see Table. 4.1). On the other hand, nine retro-reflective markers were located on the upper-limbs at the following locations: right and left AC, middle CLAV, upper arm, MHE, LHE, forearm, RS, US, and hand (see Fig. 4.4 and Fig. 4.5, as well as Fig. 2.5 for the definition of anatomical landmarks points), and tracked at a frequency of 120Hz. Both systems were synchronized using a trigger signal generated by the Optitrack system. Stereophotogrammetric data were then re-sampled off-line to match the sampling rate of the VIMUs-based system.

Nine male subjects (age 29±4years, height 178±5cm and weight 72±12kg) participated in the experiments. First, the subjects were asked to place their left arm on the table in a static comfortable position that they could choose, provided that the AR markers need to be detected by the RGB camera. The static posture was maintained for less than a minute to pin-point the arm's anatomical landmarks of interest. The pin-pointed positions were recorded using both Optitrack and the wand-based calibration systems. From these positions, joint center locations, segment lengths, as well as VIMUs local positions, required as inputs to the upper-limbs FKM, were determined. Afterwards, a series of six daily rehabilitation tasks were performed by all subjects based on the MFT [202] (see section 4.1.1 and Fig. 4.7):

- Task 1: Pick up, move and release a small bottle.
- Task 2: Pick up an object using the left arm, move it at three different positions and release it.

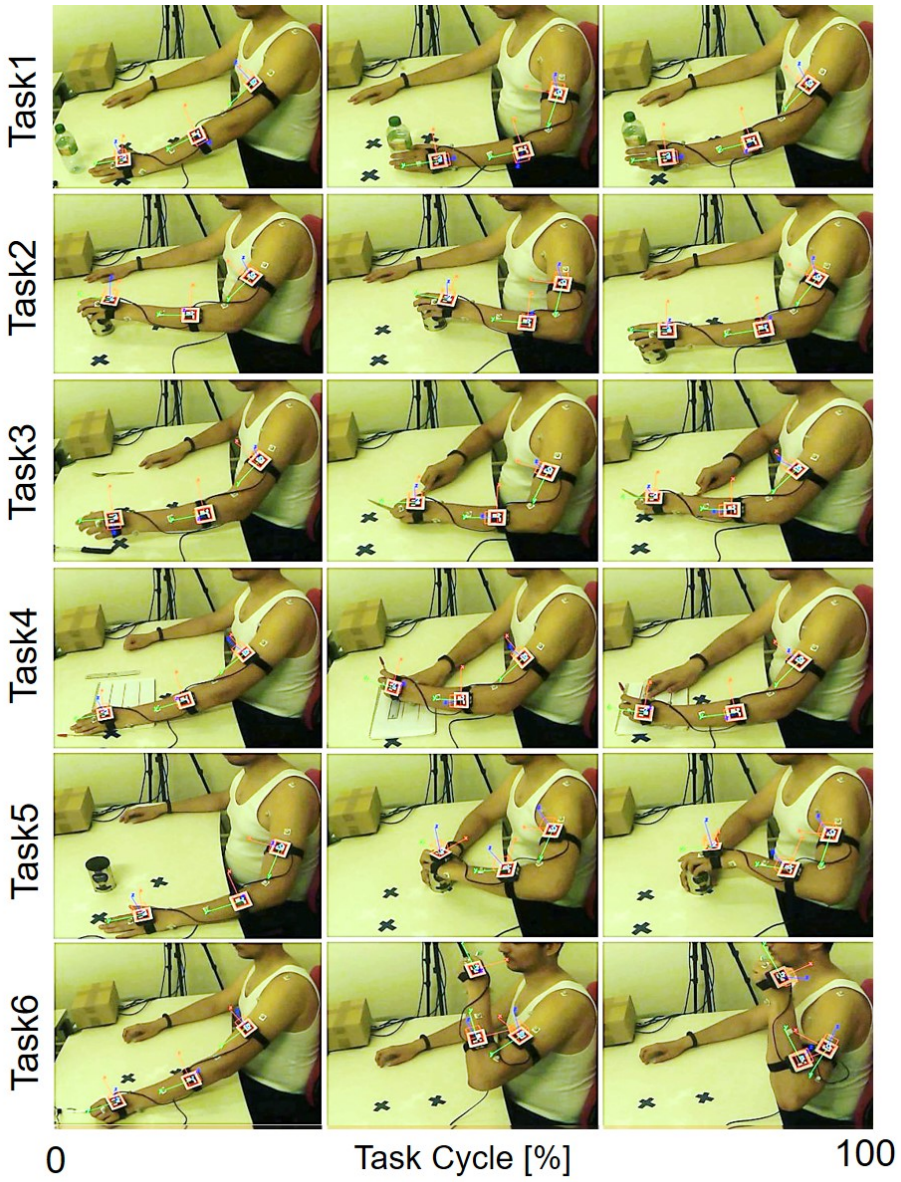

Fig. 4.7 Snapshot of the AR markers tracking taken during six MFT tasks. Task 1: Grasp, move and release a small bottle. Task 2: Pick and place an object between 3 points. Task 3: Pick up a fork and a knife and mimic cutting on the table. Task 4: Draw a line on a notebook. Task 5: Open and close a jam. Task 6: Pick up a toothbrush and mimic teeth brushing.

- Task 3: Pick up a fork and knife using both hands and mimic cutting on the table.
- Task 4: Pick up a pen and a ruler and draw a line using both hands.
- Task 5: Pick up a jam jar, open it and close it using both hands.
- Task 6: Pick up a toothbrush and mimic teeth brushing.

Three consecutive repetitions were performed for each task at comfortable speed. Based on the stereophotogrammetric data, the mechanical model described in Fig. 4.3, and the MKO [65] (see section 3.5), upper-limbs reference joint angles were estimated and used to validate the proposed system.

4.1.4 Results and Discussion

4.1.4.1 Validation of the IMU and VIMU Calibration

The validation of the proposed sensors calibration was performed twofold. First, the norm of the IMU measured accelerations was computed for static trials that were not included in Eq. 3.3. In general, the residue was very small with a value of $19e^{-3}$m.s^{-2}. Second, the calibrated accelerations were compared with those obtained during movement using the double derivation of the associated AR markers poses expressed in the IMU frame. Fig. 4.8 provides a comparison of both 3D accelerations of the forearm VIMU for one random trial with an average RMSD of 0.77m.s^{-2} before calibration, and of 0.22m.s^{-2} after calibration of the marker-to-IMU rigid transformation from section 3.1.3. This comparison was also performed over 45 trials with an average RMSD of 0.27m.s^{-2}.

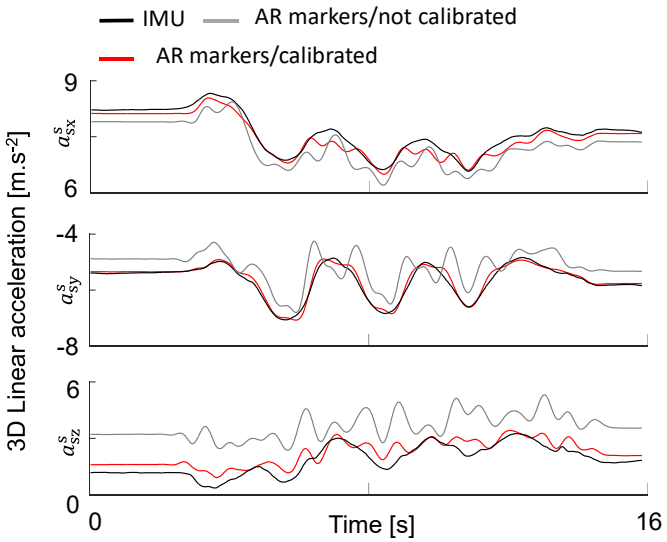

Fig. 4.8 Comparison of 3D linear acceleration obtained with both forearm IMU sensor (black) and double derivation of AR marker's position before (gray) and after (red) calibration of the marker-to-IMU rigid transformation during a randomly selected task.

4.1.4.2 Validation of the Static Wand-Based Calibration

The proposed wand-based calibration was indirectly validated w.r.t. stereophotogrammetric-based calibration. For this purpose, body segment lengths were calculated from joint center positions using both stereophotogrammetric and wand-based static calibration data. An excellent average RMSD of 2.9mm was observed between both systems for the upper arm and forearm segments lengths of all nine subjects. Obviously, another intrinsic and indirect validation of the calibration process lies in the validation of the joint kinematics estimates as discussed in the following.

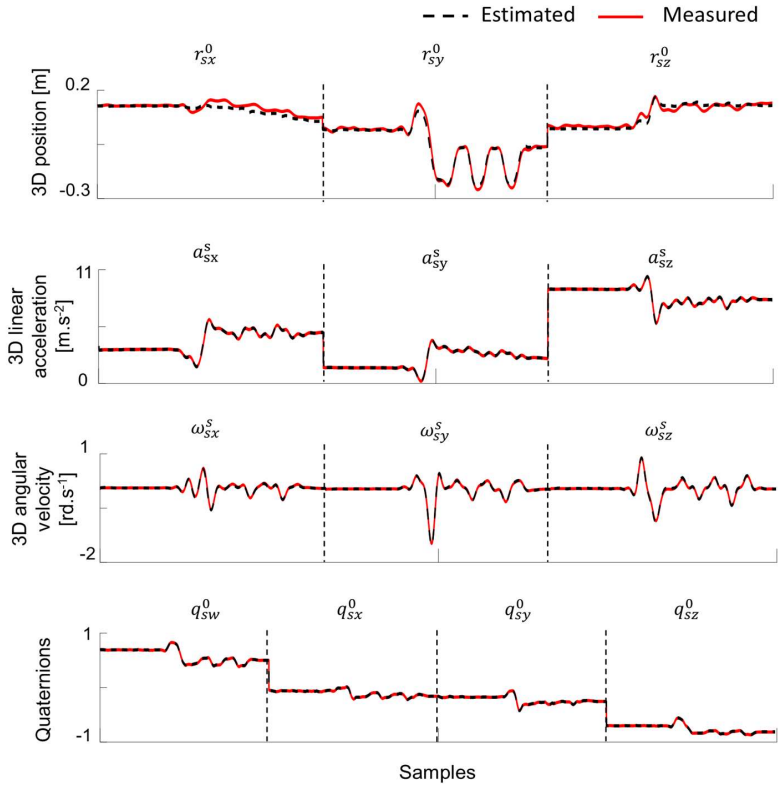

Fig. 4.9 Comparison between the sensors measured (red) and the CEKF estimated (black) 3D position, 3D linear acceleration, 3D angular velocity and quaternions for the VIMU attached to the hand while drawing three lines (task 4).

4.1.4.3 CEKF-Based vs Optitrack-Based Joint Angles Estimates

The VIMUs calibrated data were introduced as inputs to the CEKF. Fig. 4.9 shows the input data collected from the hand VIMU while drawing three lines, i.e., task 4, and their tracking using the proposed CEKF. The tracking of all measured data was very satisfactory

with average RMSDs of 18mm, 0.017m.s^{-2}, 0.029rad.s^{-1}, and 2.2e^{-2} for 3D positions, 3D accelerations, 3D velocities and 4D quaternions, respectively.

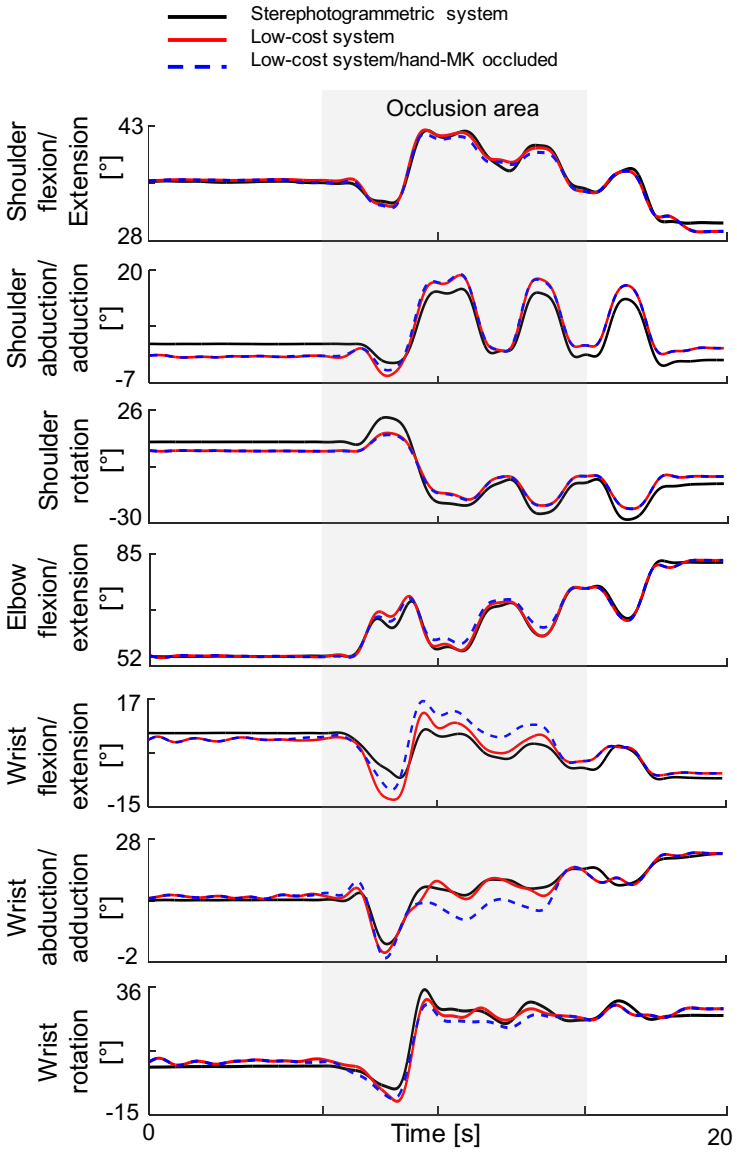

Fig. 4.10 Representative comparison of arm joint angles estimated using the proposed affordable (red) and the stereophotogrammetric (black) systems. The blue-dashed line represents the estimate of the same joint angles obtained when the hand's AR marker was occluded. The occlusion area is highlighted in gray.

The ability of the proposed VIMUs-based system to accurately estimate upper-limbs joint angles was assessed through a direct comparison with those obtained from the reference SS and Multi-body Kinematics Optimization (MKO) [65]. The VIMUs sensors were mounted in the middle of each segment, whereas the retro-reflective markers were placed on the body

anatomical landmarks following the literature recommendations [78]. This was done to minimize the influence of the Soft Tissue Artifacts (STA) on the calculated reference joint angles. Furthermore, by placing retro-reflective markers on the human body, i.e., rather than on the sensors, both affordable and reference systems were under comparable effects of the STA. It means that the influence of the relative STA on the joint angles difference from both systems was not compensated throughout the movement. As previously stated in section 2.3.1.1, fluoroscopic systems are generally used to assess the influence of STA. However, these are costly, usually limited to a single joint, and they may induce radiation to the patient, this is why they are rarely used to validate other MCSs.

Table 4.1 Results of the comparison between the joint angles obtained using the proposed affordable system and the stereophotogrammetric system. Results have been reported as mean ± SD over all the analyzed trials.

		θ_1	θ_2	θ_3	θ_4	θ_5	θ_6	θ_7
Task1	RMSD [deg]	1.1±0.3	2.2±1.0	4.7±2.2	2.3±0.9	3.5±1.2	3.3±1.3	4.9±1.4
	CC	0.98±0.01	0.82±0.20	0.67±0.30	0.98±0.02	0.90±0.07	0.73±0.26	0.88±0.15
Task2	RMSD [deg]	1.3±0.6	2.0±0.8	4.2±2.0	2.0±1.3	2.3±1.4	3.1±1.6	4.4±2.2
	CC	0.97±0.02	0.93±0.07	0.87±0.12	0.98±0.02	0.72±0.27	0.74±0.22	0.73±0.28
Task3	RMSD [deg]	1.3±1.1	1.5±0.6	2.5±1.6	1.8±1.6	3.2±1.9	2.6±2.0	3.3±1.5
	CC	0.91±0.11	0.89±0.09	0.81±0.13	0.96±0.06	0.83±0.28	0.92±0.10	0.77±0.24
Task4	RMSD [deg]	0.9±0.3	1.6±0.8	3.0±1.2	1.3±0.3	2.2±0.9	2.6±1.7	3.6±1.7
	CC	0.92±0.12	0.97±0.01	0.97±0.03	0.905±0.16	0.88±0.10	0.89±0.12	0.84±0.25
Task5	RMSD [deg]	1.3±0.9	1.8±1.0	3.2±1.9	3.0±2.5	3.5±1.4	4.8±3.0	5.4±2.6
	CC	0.89±0.13	0.74±0.30	0.92±0.06	0.97±0.02	0.96±0.02	0.85±0.27	0.71±0.23
Task6	RMSD [deg]	0.7±0.2	1.8±1.1	2.5±1.1	3.1±1.7	2.9±2.1	3.0±1.4	3.0±2.0
	CC	0.98±0.02	0.90±0.11	0.95±0.06	0.97±0.07	0.87±0.26	0.98±0.01	0.97±0.02
Mean	RMSD [deg]	1.1±0.2	1.8±0.3	3.3±0.9	2.2±0.7	2.9±0.6	3.2±0.8	4.1±1.0
	CC	0.94±0.04	0.87±0.08	0.86±0.11	0.96±0.03	0.86±0.08	0.85±0.09	0.81±0.09
				Single VIMU Assessment				
Mean	RMSD [deg]	1.8±0.9	2.7±0.8	8.3±1.5	6.9±2.8	6.9±1.1	6.1±1.1	10.8±1.7
	CC	0.70±0.13	0.85±0.08	0.50±0.08	0.77±0.16	0.40±0.20	0.52±0.15	0.50±0.19

Seven joints of the model defined in section 4.1.2.1 were estimated using both affordable and reference systems. Average RMSD and the Pearson Correlation Coefficient (CC) were calculated for each joint during all trials. Fig. 4.10 shows a representative comparison of the joint angles evolution for a randomly chosen subject while performing task 4. The

corresponding average RMSD and CC were of 2deg and 0.96, respectively. Results are reported separately for each task in Table 4.1. For all observed tasks, shoulder and wrist flexion/extension, abduction/adduction and internal/external rotation together with elbow flexion/extension were estimated with average RMSD and CC of 2.7deg and 0.87, respectively. Note that Fig. 3.9 shows the drift error in pose estimate obtained statically when integrating the IMU data over a similar period of time as the performed tasks in this study. This emphasizes how the proposed system tackles both IMU integrational drift and AR markers occlusion.

Interestingly, the best estimate was reported for the shoulder flexion/extension and abduction/adduction, and for the elbow joint with a mean RMSD lower than 2deg and a mean CC greater than 0.9. This result overcomes shoulder and elbow joint angles estimation accuracy based on either IMU or visual tracking-based systems. For instance in [103], a visual tracker based on only RGB camera and custom markers showed an average RMSD of 3.9deg for the considered angles but for much simpler tasks. The elbow flexion/extension was measured while mimicking invasive surgical tasks in [210] using an IMU-based system with an error up to 8.2deg when compared to a gold standard SS. El Gohary et al. [109], using solely IMU sensors, reported an average RMSD within the same range as the proposed VIMUs-based system for both shoulder and elbow flexion/extension angles. However, the validation was performed with an industrial arm robot, i.e. without STA and with a perfect model definition.

The shoulder internal/external rotation angle estimate was less accurate but remains within the range of a SS ability to estimate shoulder joint angle. The shoulder is a complex joint, with the internal/external rotation being highly sensitive to STA [211]. This might explain why the accuracy of θ_3 varied largely with the different motion situations. A recent study of the typical errors for the model derived glenohumeral rotations [79] showed that errors for internal/external rotation can be superior to 20deg, which is largely more significant than the one obtained in this study (maximal RMSD of 4.7deg). The larger differences were reported for wrist joints and more particularly for the internal/external rotation angle where a mean RMSD of 4.1deg and a mean CC of 0.81 were observed. This is due to the fact that the wrist exhibits large motions, in particular θ_7 for tasks 1, 2 and 5. Moreover, the wrist is the last joint of the kinematic chain where the influence of all estimation errors, including STA and calibration errors, may accumulate. We should note that all joint angles, including those represented in Fig. 4.10, were estimated within the feasible range of motion of the arm model being investigated.

Finally, since the subject's comfort is a major concern, a preliminary investigation shows that when only the hand VIMU is used, it is possible to estimate all the seven joint angles

of the human arm with an accuracy of 6.2deg. This is 2.3 times larger than when taking into account all three VIMUs sensors into the EKF. However, having a single sensor could obviously be of great advantage for the ease of donning and doffing. Using a single sensor is possible thanks to the prior sensor-to-body calibration and to the use of the AR marker 3D pose in the CEKF. Interestingly, despite the fact that the retained mechanical model has seven DoFs, making the system redundant, it was possible for the investigated tasks to estimate all joint angles with just a slight decrease in accuracy. In theory, for a redundant system, there is an infinite number of joint configurations for a given hand pose. In this study, the CEKF takes into account the history of the system (i.e. the previous joint configuration). This somehow acts like a weighed inverse kinematics process choosing the closest solution from the previous one among an infinity while satisfying joints constraints. However, it is important to note that the investigated tasks take place far from singular configurations, and this might also explain why no joint reconfiguration was observed.

Robustness to Occlusion Analysis As previously stated, the AR markers are subject to occlusion. In particular, the time and occurrences of AR markers occlusions may differ according to the task that is performed by the subject. To test the robustness of the proposed method to occlusions, we proposed to virtually impose a long occlusion on the AR marker of the hand. This assumption was investigated during an extended period of time of 9.25s (46% of the total task duration). When an occlusion is detected, the corresponding parameters in the measurement noise covariance matrix $\mathbf{R}$, were given a large value ($> 1e^3$), indicating a lack of trust in these measurements. Thus, IMU data were considered to be much more reliable by the EKF. The gray area of Fig. 4.10 shows the relatively satisfactory estimation of arm joint angles when the hand-marker data have been ignored. When relying only on IMU data, the average RMSD and CC were of 2.56deg and 0.93, respectively. Although θ_5 and θ_6 estimation makes this result slightly worse than the one obtained with no occlusion, the EKF was able to accurately reconstruct the arm joint trajectories.

4.2 Affordable Full Lower-Limbs Gait Analysis Using a Reduced Sensors-Count Configuration

3D gait analysis provides quantitative information about joints kinematics and spatio-temporal parameters (e.g., speed, stride length), which constitute valuable clinical observations in the case of several pathologies. Among comprehensive clinical measures of gait performance, the Gait Deviation Index (GDI) has been recently developed [212] as a single parameter used to quantify the gait pattern. It is computed by using nine kinematic parameters

collected from patients (pelvis and hip joints angles in three planes, knee flexion/extension, ankle dorsi/plantarflexion, and foot progression), and comparing them to a healthy control group. The absolute distance between healthy strides and patient's strides is then calculated, providing a measure with good statistical properties from which the degree of gait pathology can be estimated.

To estimate lower-limbs gait kinematics, a new prototype of a VIMUs-based MCS has been developed in this study with a dedicated design aiming at compensating for markers occlusion. The new system is wireless and consists of a reduced number of sensors, such that it can be used in daily routine while ensuring the user comfort and reducing the setup time and cost. Reducing the number of sensors, however, intrinsically reduces the available kinematic information used to for the inverse kinematics process [136].

4.2.1 Lower-Limbs Joint Kinematics Estimation Framework

This section makes use of two variations of the calibration processes presented in section 4.1: IMU and VIMU calibration, which is performed once with a given set of sensors; and VIMU-to-body calibration, which should be performed once for each new subject. The new VIMUs sensors proposed in this study require an additional marker-to-marker rigid transformation calibration relating all three AR markers local frames within the same VIMU. The relative pose between each two markers is introduced as a rigid body constraint in the CEKF. It is also used to reconstruct markers poses in the case of occlusion. Besides, the lower-limbs mechanical model and the novelty in the CEKF implementation for full gait kinematics estimation are also presented.

4.2.1.1 Lower-Limbs Mechanical Model

A mechanical model was used to estimate the lower-limbs joint kinematics from the output of only three VIMUs sensors attached to the sacrum, left, and right heels segments (see Fig. 4.11.a). It consists of $N_L = 7$ segments connected through $N_J = 18$ DoFs, including twelve revolute joints describing the hip (three DoFs), knee (one DoF), and ankle (two DoFs) motion, respectively. The model floating base is described through three revolute and three prismatic joints w.r.t. the global system of reference R_0.

The new VIMU sensor prototype is composed of a single IMU covered at its top with three AR markers mounted in a bracelet form (see Fig. 4.11.b and Fig. 4.12). It provides the absolute 3D pose of each AR marker w.r.t. R_0, as well as the 3D linear acceleration $\mathbf{a}_s^s$ and 3D angular velocity $\mathbf{\Omega}_s^s$ w.r.t. the sensor local frame. Three local frames were used to

represent the VIMU (see Fig. 4.12).a: a local frame corresponding to both IMU and central AR marker, as well as two others representing the left and right markers. Note that the IMU frame could be assumed aligned with that of the central marker thanks to the pre-calibration of the marker-to-IMU rigid transformation from section 3.1.3.

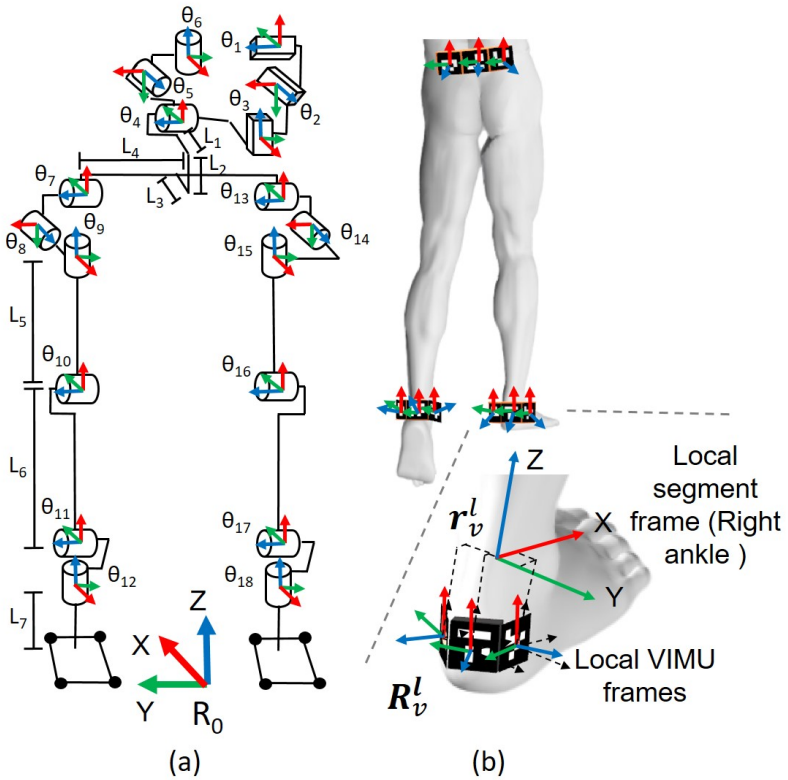

Fig. 4.11 (a) Lower-limbs mechanical model composed of $N_L = 7$ segments, and of $N_J = 18$ DoFs. (b) Set up of three affordable VIMUs attached to the sacrum, left, and right heels in a bracelet form. $(\mathbf{R}_v^l, \mathbf{r}_v^l)$ with $v = m_l, m_r, s$ are the relative poses of the local frames associated with the left and right AR markers, and the (IMU sensor-central AR marker) of each VIMU module w.r.t. its corresponding segment anatomical frame, respectively.

4.2.1.2 Pre-Calibration

Besides the IMU and marker-to-IMU calibration from sections 3.1.1 and 3.1.3, the new VIMU sensors present another rigid transformation to be calibrated, for only once, between each two AR markers. Once calibrated, this transformation is constant for each sensor. Indeed, the sensors design, shown in Fig. 4.12, is intended to reduce the problem of AR markers occlusion. This suggests that at least one of the three markers appears in front of the camera during movements that include complex rotations. Based on this marker detected pose, the occluded markers poses may be reconstructed since all three markers local frames are linked together using the follwoing Eq. 4.5:

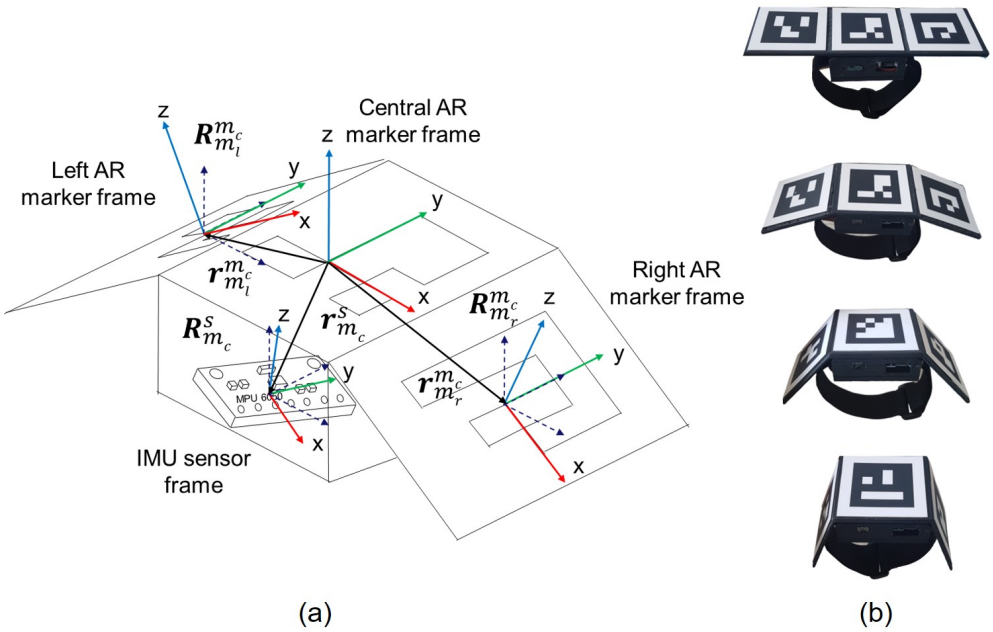

Fig. 4.12 (a) Representative description of a VIMU calibration. The IMU sensor, left, and right AR markers local frames are all aligned w.r.t. the one of the central marker, given that s, m_l, m_c, and m_r refer to the IMU sensor, left, central, and right markers, respectively. (b) The VIMUs new sensors prototype with four different configurations.

$$\begin{aligned} \mathbf{R}_{m_{j_i}}^{m_{ci}} &= (\mathbf{R}_{m_{ci}}^{0})^T \mathbf{R}_{m_{j_i}}^{0} \\ \mathbf{r}_{m_{j_i}}^{m_{ci}} &= (\mathbf{R}_{m_{ci}}^{0})^T (\mathbf{r}_{m_{j_i}}^{0} - \mathbf{r}_{m_{ci}}^{0}) \\ \text{with} \quad & j = l, r \quad i = 1, ..., N_P \end{aligned} \tag{4.5}$$

where ($\mathbf{R}_{m_{j_i}}^{m_{ci}}$ (3×3), $\mathbf{r}_{m_{j_i}}^{m_{ci}}$ (3×1)), with $j = l, r$, is the relative pose from the local frame of the VIMU central marker to the ones located at the left and right, respectively and i is the static pose of the sensor. Note that the rotation matrices were converted into quaternions $\mathbf{q}_{m_{j_i}}^{m_{ci}}$ (4×1). Both relative poses, i.e., central-left and central-right, were then normalized over $N_P \simeq 50$ static poses of the sensor (see Fig. 4.13) and used as additional constraints into the CEKF (see section 4.2.1.3).

Once the VIMUs were fully calibrated, their locations on their corresponding lower-limbs segments were calibrated using the wand-based method (see section 4.1.2.2). Fig. 4.11 exemplifies for the right ankle the local pose $(\mathbf{R}_s^l, \mathbf{r}_s^l)$ describing the VIMU pose in its corresponding segment. For all three coordinate frames, there are three local poses to be determined for each sensor. Eleven lower-limbs anatomical landmarks were pinpointed in this context: midpoint between the right and left PSIS, and ASIS, LFE, MFE,

LM, and MM of both left and right sides (see Fig. 2.5 for the definition of anatomical landmarks). Subsequently, joint centers positions, N_L segment lengths, initial lower-limbs joint configuration, as well as VIMUs-to-body segment's local poses were calculated and used as inputs in the FKM-based measurement model of the CEKF.

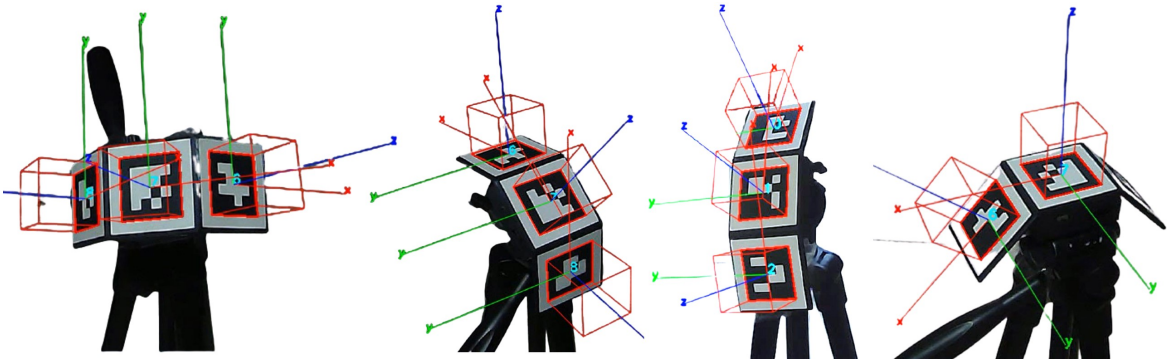

Fig. 4.13 VIMUs sensors are pre-calibrated only once over N_P different static poses.

4.2.1.3 Constrained Extended Kalman Filter

Similarly to the study developed in section 4.1, a CEKF was developed to fuse the VIMUs calibrated data. Besides, IMU bias, lower-limbs kinematic model, as well as physiological joint limitations, Joint Soft Constraints (JSCs), and VIMUs rigid-body constraints were implemented within the CEKF to improve the accuracy and ensure the feasibility of the output joint kinematics estimates.

Process Model Two formulations of the process model f were investigated in this study. First, a regular constant acceleration model was used similarly to Eq. 4.3. Second, lower-limbs joint trajectories were modelled using a Fourier series expansion, taking advantage of the gait periodic motion. In the following, both formulations are denoted as CEKF-CA and CEKF-FS, respectively.

Thus, within the CEKF-FS, joints trajectories are modelled as:

$$\theta_i(t) = \mathbf{a}_{i0} + \sum_{n=1}^{N_H} (\mathbf{a}_{in} cos(n\omega t) + \mathbf{b}_{in} sin(n\omega t)) \tag{4.6}$$

where $i = 1,..,N_J$ is the number of joint, ω is the main frequency of the movement, and $n = 1,..,N_H$ is the number of harmonics selected as a trade-off between accuracy and computation time. $\dot{\boldsymbol{\theta}}_i(t)$ and $\ddot{\boldsymbol{\theta}}_i(t)$ are obtained through the differentiation of Eq. 4.6 w.r.t. the time. The

state vector defined in Eq. 4.2 is hence modified by substituting the joint trajectories with their associated Fourier coefficients, as follows:

$$\begin{aligned} \mathbf{x}_{i,k(FS)} = [\mathbf{a}_{i0} \quad \mathbf{a}_{in} \quad \mathbf{b}_{in} \quad \mathbf{b}_{a,k}]^T \\ \text{with} \quad i = 1,...,N_J \\ n = 1,...,N_H \end{aligned} \tag{4.7}$$

such that the new state vector dimension becomes $N_{X(FS)} = ((1+2N_H)N_J + 3N_S) \times 1)$. Also, the new process model was set as a simple identity model to represent the new state vector evolution, such as:

$$\mathbf{x}_{k+1} = \mathbf{I}_{\mathbf{d}N_{X(FS)}} \mathbf{x}_k \tag{4.8}$$

This was assumed as the Fourier series coefficients are expected to converge towards constant values. Despite that, note that any change in $\mathbf{x}_k$ would be taken into account in the process noise covariance matrix denoted as $\mathbf{Q}_{FS}(N_{X(FS)} \times N_{X(FS)})$.

Measurement Model The measurement model is primarily based on Eq. 4.1, and is calculated together with its Jacobian using CasADi an open-source automatic-differentiation library in C++ [213]. Given the sacrum, left, and right back-feet VIMUs, the new measurement vector dimension is $N_Y = (3\times3+3+3+4\times3)\times(N_S = 3)$, including the absolute 3D pose and the (4×1) quaternions of three AR markers, as well as the 3D linear acceleration and 3D angular velocity of each sensor.

In addition to the fusion of both markers and IMU redundant measurements, two types of constraints were introduced as virtual measurements into the CEKF to further mitigate the effect of IMU drift. First, hip, knee, and ankle JSCs were enforced using the Eq. 4.9 below:

$$\begin{aligned} \theta_{i\,sc} = (\theta_i - \theta_{iM})^2 \\ \text{with} \quad i = 7,...,N_J \end{aligned} \tag{4.9}$$

where θ_i, with $i = 7,..,N_J$, is the joint angle of the hip, knee, or ankle to be estimated by the CEKF (see Fig. 4.11), $\theta_{i\,sc}$ is the soft constraint referring to joint θ_i, and θ_{iM} is a constant mean value assigned to θ_i. Since the VIMUs count is reduced, multiple kinematics solutions may exist and lead to the same VIMUs measurements in the Cartesian space. To constrain the solution space, we proposed to push the joint solution toward the average joint angle value, θ_M, reported for walking in the literature: 13deg, 8deg, 11deg, 16deg, 1deg, 6deg for θ_7, θ_8, θ_9, θ_{10}, θ_{11}, θ_{12} angles of the left leg and, symmetrically for the right leg, respectively. In the context of the CEKF, this was done by adding N_J pseudo-measurements in the measurement model h aiming at minimizing the squared difference with θ_M at each sample of time by

setting the corresponding measurements in **y** to zero. Second, rigid-body constraints between the three AR markers of the same VIMU were incorporated into the measurement vector as accurate pseudo-measurements. Therefore, the pose of the right and left AR markers w.r.t. the central AR maker should match their values obtained during the VIMU calibration from section 4.2.1.2.

As a result, all three Eq. 4.1, 4.5, and 4.9 formed the CEKF measurement model used to estimate lower-limbs gait kinematics. Moreover, the new measurement vector dimension becomes $N_Y = (3\times3+3+3+4\times3)\times(N_S=3)+(3+4)\times2\times(N_S=3)+N_{JC}$, further including the (3×1) position and the (4×1) quaternion of both central-left and central-right markers rigid transformations of each sensor, whereas N_{JC} is the number of joints with implemented soft constraints.

Parameters Tuning Two different tunings of both CEKF-CA and CEKF-FS parameters, i.e., the process and the measurement noise covariance matrices, were investigated. Particularly, the CEKF-CA parameters were adjusted using optimization, whereas those of the CEKF-FS were set empirically taking advantage of the gait quasi-periodicity. This was considered as the latter includes larger dimensions of both state and measurement vectors, which suggests an increased computational cost. Furthermore, optimization might have to be re-conducted in the case of different motions or settings, which may be challenging and time-consuming for end-users. With such tuning we intended to achieve an acceptable accuracy within both CEKF formulations. Also we aimed to prove better, or at least similar, accuracy when using the CEKF-FS even without using any cumbersome optimization.

Optimization was done using COBYLA algorithm [214] in C++ as provided by the open source library NLopt [215]. It aimed at minimizing the squared difference between the reference and the CEKF-CA-based joint angles obtained throughout the entire movement of a given trial subject. Overall, thirteen parameters were optimized and are gathered in the vector $\mathbf{V} = [Q_\theta \;\; Q_{\dot\theta} \;\; Q_{\ddot\theta} \;\; R_p \;\; R_q \;\; R_a \;\; R_\Omega \;\; \mathbf{R}_\theta]^T$ (13×1). **V** includes three parameters Q_θ, $Q_{\dot\theta}$, $Q_{\ddot\theta}$ in **Q** matrix referring respectively to the joint angles, velocities, and accelerations, and ten others associated with the VIMUs measurements and the JSCs in **R** matrix, i.e., positions R_p, accelerations R_a, velocities R_Ω, quaternions R_q, as well as six parameters referring to the soft constraints of the six joints $\mathbf{R}_\theta = R_{\theta_i}$ with $i = 7...N_J$ (assuming left and right symmetry). The problem of **V** optimal tuning can then be formulated as follows:

$$\begin{aligned} &\text{Find} \;\; \mathbf{V}^* \in \min_{\mathbf{V}\in\mathbb{R}^{13}} \sum_{j=1}^{N_{JC}} \sum_{k=1}^{N} (\theta_{SS_{jk}} - \theta_{jk})^2 \\ &\text{subject to} \quad \mathbf{V}^- \leq \mathbf{V} \leq \mathbf{V}^+ \end{aligned} \tag{4.10}$$

where N is the number of samples of the trial test being considered. $\mathbf{V}^-$ and $\mathbf{V}^+$ represent the upper and lower boundaries, respectively. θ_{SS} (18×1) is the vector of the reference joint angles estimated using the SS and MKO (see section 3.5).

In the case of CEKF-FS, it is important to determine the number of harmonics N_H required to accurately estimate the joint trajectories. This was done by solving a priori the following fitting problem for different values of N_H:

$$\begin{aligned}\text{Find } \mathbf{a}^*,\mathbf{b}^*,\omega^* \in & \min_{\mathbf{a}^*,\mathbf{b}^*,\omega^*\in\mathbb{R}^{2N_H+N_J+1}} \sum_{j=1}^{N_J}\sum_{k=1}^{N}(\theta_{SS\,jk}-\theta_{jk})^2 \\ \text{s.t.} \quad & 0\leq\omega\end{aligned} \tag{4.11}$$

Based on Eq. 4.11, N_H was selected as a trade-off between the number of parameters being used and the accuracy of the joint trajectories estimates. The parameters tuning is then based on a priori knowledge of the biomechanics of the task being investigated. Thus, the diagonal elements in $\mathbf{Q}$ were set to a small value (0.01) to enforce their convergence to pseudo-constant values [216]. The elements of $\mathbf{R}$ related to the measurements were empirically set based on section 4.1.2.3. Whereas, those related to the JSCs obtained as the difference between estimated and average joint angles, were set accordingly to the joint angle amplitude tipically observed in gait such that $\mathbf{R}_\theta = [1\ \ 1\ \ 1\ \ 10\ \ 1\ \ 10]$.

Regarding the tuning of the VIMUs rigid body constraints parameters in $\mathbf{R}$ matrix, it was the same for both CEKF formulations. These were set to a small value ($1e^{-3}$) reflecting relatively accurate pseudo-measurements. Thanks to the VIMU bracelet design and to the use of VIMU rigid body constraints, AR markers occlusions was greatly limited. Despite that, AR markers remain sensitive to occlusions based on the motion phase. Fortunately, these occlusions are easily detectable. Thus, if the loss of all three markers data was detected, the corresponding elements of the measurement noise covariance matrix $\mathbf{R}$ will be automatically updated to reflect the new state of input data. Consequently, two $\mathbf{R}$ matrices were considered: the one corresponding to the whole markers trajectories when no occlusion of at least one marker has occurred and another one when all AR markers were occluded. In the second case, the missing markers poses were replaced by their previous values and their associated $\mathbf{R}$ elements were given a large value ($1e^3$) indicating a lack of trust in these measurements.

4.2.2 Experimental Setup

4.2.2.1 System Hardware Design

The price of the new system proposed in the present study was also considered in any aspect of its conception. Compared to the first VIMU prototype (see Fig. 4.6), the new proposed

sensor, shown in Fig. 4.12, is able to communicate wireless IMU data using an HC-06 Bluetooth module. Once connected, the data recording may last for eight consecutive hours thanks to a lithium battery. Instead of a single AR marker, three markers were mounted on the top of the IMU enclosure with three different configurations. Several markers configurations were considered in a 3D printed bracelet form that fits multiple subjects/segments (see Fig. 4.12.b). The markers poses were tracked using two RGB cameras visualizing the whole scene from two different positions (see Fig. 4.14). The data recording program was also updated in C++ to record all connected VIMUs data synchronously at a frequency of 60Hz.

4.2.2.2 Experiments

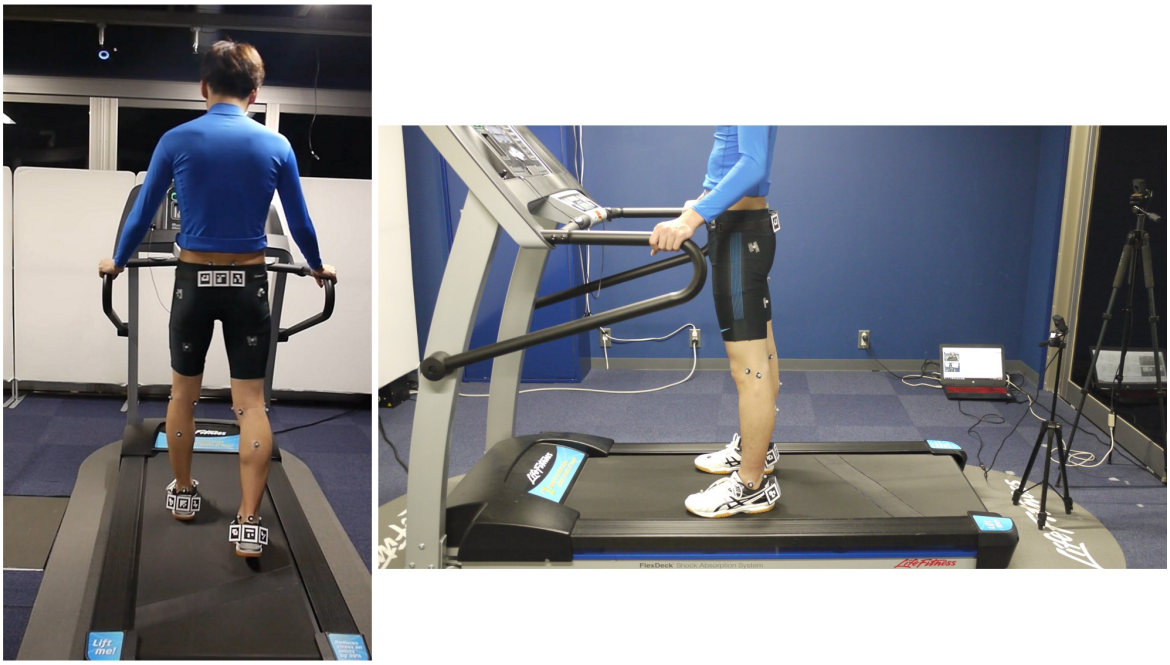

Fig. 4.14 Side and back views of the experimental setup used during treadmill gait motion.

The proposed system accuracy was assessed w.r.t. the Optitrack SS. Twenty-two retro-reflective markers were located on lower-limbs anatomical landmarks, and tracked at 100Hz using five Prime cameras [83]. On the other hand, three VIMUs sensors were attached to the sacrum and to the heels (see Fig. 4.14). Their pose was tracked using two RGB cameras set up on tripods to capture the entire subject's movement (see Fig. 4.14).

Five young, healthy male volunteers (age 23.6±3.7years old, weight 64.0±3.9Kg, height 1.7±0.03m) participated in the experiments. Prior to data collection, each subject received a brief explanation of the study and gave their informed consent. Both wand-based and stereophotogrammetric-based calibrations were performed synchronously with the subject

standing still for less than 1min at a self-selected comfortable posture that allows detecting AR markers with the RGB cameras. After the calibration trial, subjects performed treadmill walking, first for a familiarization time of a few seconds, and then for a recording time between 30 and 120s at 0.5Km/h.

4.2.3 Results and Discussion

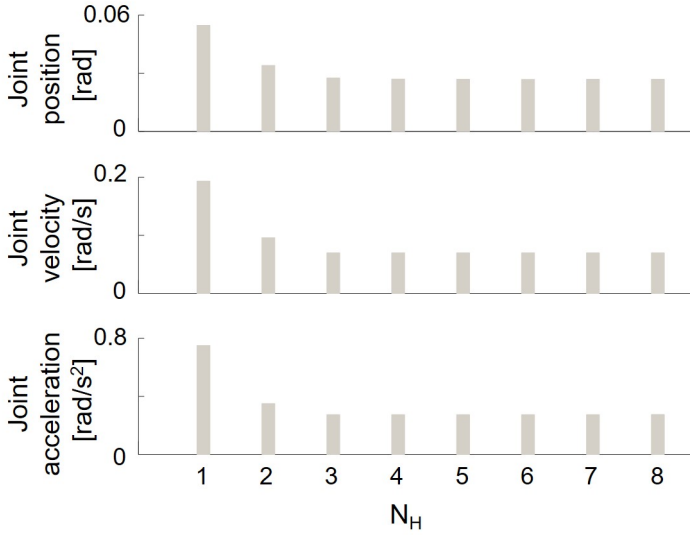

Fig. 4.15 Mean RMSD between the joint positions, velocities and accelerations estimated using Fourier series expansion and those obtained using the SS as a function of the number of harmonics N_H.

Fig. 4.15 depicts the mean RMSDs of the joint positions, velocities and accelerations calculated using Fourier series representation and those obtained using the SS as a function of the number of harmonics N_H for a randomly selected subject. Accordingly, the number of harmonics was set to $N_H = 4$ to minimize the RMSD of the joint trajectories.

Based on section 4.2.1.3, besides the VIMUs calibrated data, the two vectors composed of the VIMUs rigid body constraints, calibrated in section 4.2.1.2, and of the JSCs, set to zero (see Eq. 4.9), were constant for all subjects and introduced as input pseudo-measurements into the CEKF. Fig. 4.16 displays the input data from the left back-heel VIMU of a randomly selected subject, including the JSCs and the VIMU position, as well as their CEKF-based tracking while walking on the treadmill. The large peaks that can be observed in Fig. 4.16.a were due to the fact that depending on the motion phases, the complete occlusion of all three AR markers could not be entirely avoided. More specifically, the AR markers were not detected just after toe-off phases where all three markers of the VIMUs attached to the

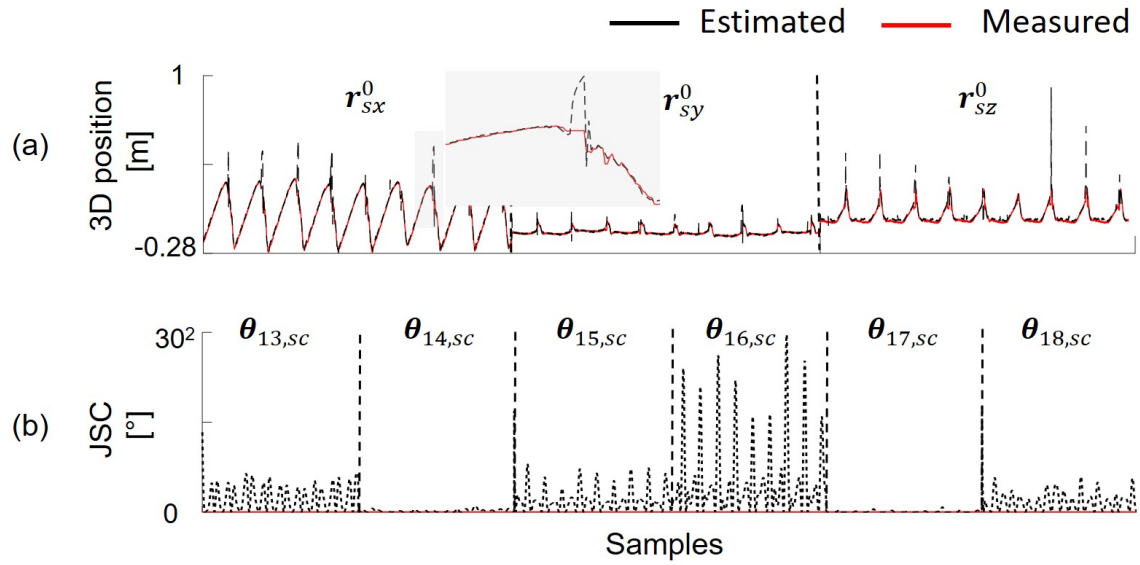

Fig. 4.16 Comparison between the input raw data (red) and those estimated by the CEKF (black) exemplified for (a) the VIMU 3D position attached to the left back-shoe and (b) the left hip, knee, and ankle JSCs during treadmill gait.

back-heels could be positioned nearly perpendicularly to the cameras. This is shown in the zoomed capture of Fig. 4.16.a where one can note that the CEKF is not tracking inconsistent visual data. Yet, the CEKF was able to cope with such occlusion and to estimate accurately the lower-limbs joint angles by relying more on IMU data thanks to the online update of the measurement covariance matrix **R** with the appropriate parameters tuning. Moreover, the JSCs integrated in the CEKF measurement model have the effects of joint springs pushing the joint angles toward mean values. This was motivated by the fact that a reduced sensors-count configuration was used, which may lead to different joint configurations, possibly within the joint limits, even for the same VIMU tracking data.

The eighteen joints of the model described in Fig. 4.11 were estimated using both VIMUs-based and Optitrack systems. These were the 3D position of the pelvis base segment, θ_1, θ_2, and θ_3 along the Y, X, and Z-axes respectively, as well as the angles of the pelvic tilt (θ_4), obliquity (θ_5), and rotation (θ_6), the hips flexion/extension (θ_7 and θ_{13}), abduction/adduction (θ_8 and θ_{14}), internal/external rotation (θ_9 and θ_{15}), the knees flexion/extension (θ_{10} and θ_{16}), the ankles dorsi/plantarflexion (θ_{11} and θ_{17}), and inversion/eversion (θ_{12} and θ_{18}), of both right and left sides, respectively. For both CEKF-CA and CEKF-FS state vector formulations, Fig. 4.17 presents a representative comparison of all joints estimates of a randomly selected subject. Accordingly, the pelvis motion was accurately estimated with mean RMSDs and CCs of (0.4±0.0cm, 0.86±0.2) and (0.4±0.0cm, 0.80±0.3) for 3D position estimates, and of

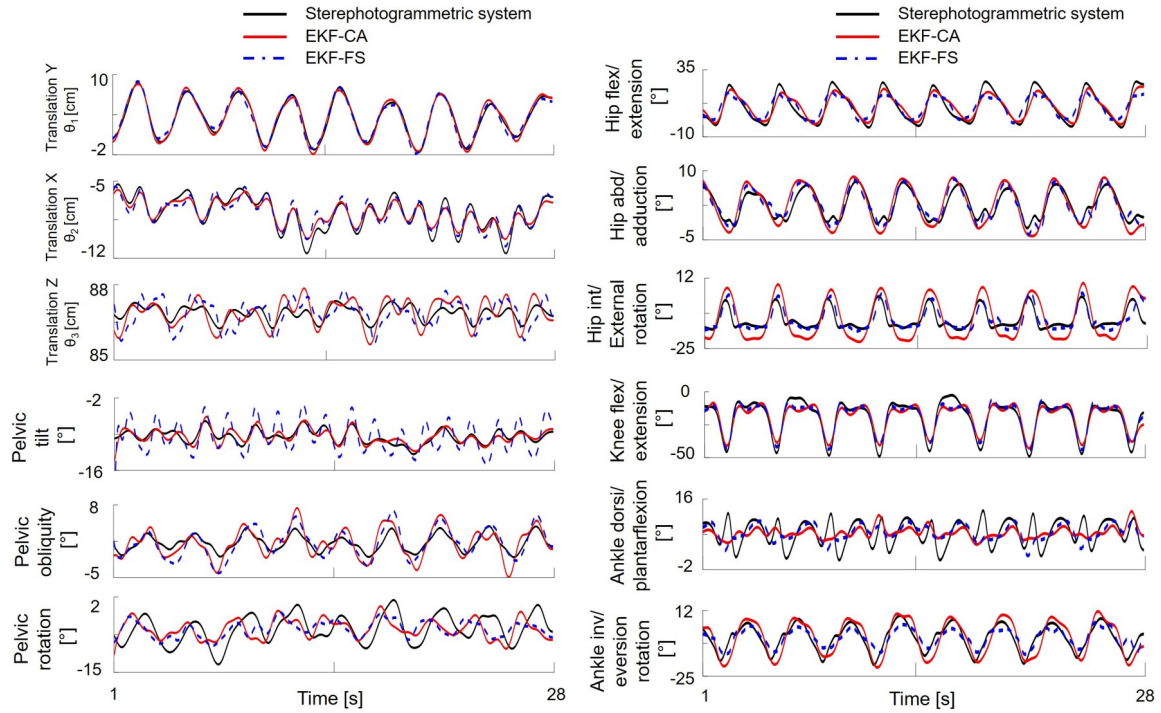

Fig. 4.17 Representative comparison of (a) the pelvis joint trajectories and (b) of the left leg joint angles obtained for a random selected subject while walking on a treadmill using the SS (black) and the proposed approach based either on a constant acceleration model (red) or on Fourier series expansion (dashed blue).

(1.6±0.94deg, 0.76±0.16) and (2.17±0.76deg, 0.66±0.25) for joint angles estimates when using the EKF-CA and EKF-FS, respectively. The corresponding lower-limbs joint angles, normalized between the left and right sides, were estimated with mean RMSDs and CCs of 3.7±1.5deg and 0.76±0.26 using the CEKF-CA and of 3.6±1.2deg and 0.76±0.20 using the CEKF-FS, respectively. Table. 4.2 summarizes the comparison results for all joints and subjects. In general, results were comparable between both CEKF formulations with mean RMSDs lower than 0.7cm, 2.1deg, and 4.2deg and mean CCs greater than 0.80, 0.60, and 0.71 for the estimates of the pelvis 3D position, the pelvis joint angles, and the lower-limbs joint angles, respectively. In the sagittal plane, average RMSD and CC of 3.4deg and 0.70 were reported for the pelvic tilt and the hip, knee, and ankle flexion/extension angles. Especially, the hip and knee joint angles in the sagittal plane had very good accuracy with a mean RMSD lower than 4.4deg and a mean CC greater than 0.91. In contrast, the pelvic obliquity and rotation and the ankle dorsi/plantar flexion estimates had the poorest CCs of 0.56 and 0.4 but with satisfactory RMSDs of 3.3deg and 1.4deg, respectively. This might be expounded by the small RoM of these joints while walking on the treadmill. Note that the tracking error is

not equitably distributed between all joint trajectories due to JSCs and to different parameters values in the covariance matrix **R**. When compared to reference invasive kinematics (bone pins or fluoroscopy), a systematic review reported errors between 1 and 22deg of the knee joint estimate tracked using retro-reflective markers placed on both thigh and shank segments [79]. The proposed method outperforms related studies dealing with a reduced sensors-count configuration [136], or using solely IMU sensors [154], or very large occlusion-prone AR markers [69, 98] located on each segment, while relying on magnetometer data or on a tedious set of calibration postures/movements [136, 217], as well as w.r.t. qualitative visual observation (RMSD 9deg [154]), which is currently often used by clinicians. We should also note that in both CEKF formulations, including the study developed in section 4.1 and using the CEKF-CA formulation, further reasons to the difference in joint angles estimates might be due to the constant body segment lengths, computed statically as the distance between consecutive joint centre positions, as well as to the VIMUs-to-segments translational and rotational offsets. These latter may occur due to uncertainties in AR markers measurements at initial static calibration, the assumption of sensors-to-segments rigid connection, and STA. In such case, both segments lengths and VIMUs local poses could be modelled in the CEKF but at the cost of increasing the state vector dimensions. Moreover, stride lengths and GDI results were calculated based on the methods proposed in [218], [219], [212], and are gathered in Table. 4.3. Stride lengths were calculated using VIMUs raw data, as well as both CEKF-CA and CEKF-FS estimated data, and were compared w.r.t. the SS. To do so, the occurrences of heel strikes and toe-offs were first determined [218] while walking on the treadmill, and then used to estimate the corresponding step lengths based on the estimated pelvis and feet positions [219]. In general, the use of the CEKF led to mean RMSD lower than 1.5cm or 2.3% when normalized by the total stride length, which improved the stride length estimate by up to 50% compared to when using the raw data (RMSD = 2.8cm, NRMSD = 4.3). This result is of the same order of magnitude compared to previous studies [220]. For instance, [221] reported an accuracy up to 3% for step length estimate. Despite its ease-of-use, their approach is limited to normal walking due to signal features dependency. Indeed, it relies directly on the IMU signal to detect heel strikes and assumes a support leg in full extension. Recently, [222] compares different spatio-temporal parameters in normal and pathological gait and reported average stride length up to 1.05m and 1.24m in healthy and amputee patients, respectively. This difference is significantly greater than the proposed system accuracy, which could easily distinguish between the different walking modes.

Table 4.2 Results of the comparison between eighteen lower-limbs joint trajectories obtained using the proposed affordable system and the SS. Results have been reported as mean ± SD over all subjects. Hip, knee, and ankle joints have been normalized between left and right sides.

	CEKF-CA		**CEKF-FS**	
Pelvic Translations	**RMSD [cm]**	**CC**	**RMSD [cm]**	**CC**
Translation Y θ_1	0.7±0.2	0.96±0.03	0.8±0.3	0.94±0.06
Translation X θ_2	0.8±0.2	0.96±0.02	0.7±0.2	0.96±0.02
Translation Z θ_3	0.4±0.2	0.64±0.17	0.6±0.2	0.47±0.34
Mean	0.6±0.2	0.85±0.08	0.7±0.1	0.79±0.27
Joint Angles	**RMSD [deg]**	**CC**	**RMSD [deg]**	**CC**
Pelvic Tilt	1.4±0.6	0.56±0.26	2.1±0.5	0.52±0.22
Pelvic Obliquity	1.9±0.8	0.56±0.17	1.7±0.5	0.71±0.16
Pelvic Rotation	2.3±0.7	0.67±0.08	2.4±1.0	0.54±0.35
Hip Flex/Extension	3.6±1.1	0.94±0.03	4.0±1.0	0.92±0.03
Hip Abd/Adduction	2.9±1.4	0.63±0.15	2.5±1.1	0.66±0.27
Hip Int/External Rotation	4.4±1.4	0.78±0.24	3.9±1.0	0.67±0.30
Knee Flex/Extension	5.3±1.2	0.89±0.07	4.6±0.8	0.92±0.05
Ankle Dorsi/ Plantarflexion	3.3±0.4	0.40±0.26	2.9±1.1	0.50±0.19
Ankle Inv/Eversion	5.5±1.8	0.66±0.27	4.6±1.5	0.60±0.32
Mean	3.4±1.4	0.68±0.17	3.2±1.1	0.67±0.16

Table 4.3 Comparison between the stride lengths and Gait Deviation Index (GDI) obtained using the affordable raw data and the ones estimated by the CEKF over all subjects and strides.

	Raw data		**CEKF-CA**		**CEKF-FS**	
	RMSD [cm]	**NRMSD [%]**	**RMSD [cm]**	**NRMSD [%]**	**RMSD [cm]**	**NRMSD [%]**
Right	2.8±1.4	4.3±2.2	1.5±0.1	2.3±0.5	1.3±0.1	1.9±0.2
Left	2.8±1.2	4.2±2.1	1.4±0.3	2.1±0.6	1.3±0.2	1.9±0.4
	SS Data		**CEKF-CA**		**CEKF-FS**	
GDI	102.56		117.77		116.02	

Subsequently, the GDI [212] was calculated using the estimated stride lengths and joint angles, and compared with the ones obtained using the reference SS data. Although the results presented in Table. 4.3 show some differences between the GDIs obtained from SS and CEKF, but it is important to note that all the GDIs (the reference and the estimated ones) were greater than 100. By definition, a GDI $\geq$ 100 indicates that the strides being investigated are close enough to healthy strides so they can be classified as normal ones. Thus, the obtained GDIs suggest that the joint angles and step lengths estimated using the proposed approach have the potential to provide clinically useful indicators.

4.3 Conclusion

This chapter has conducted the experimental validation of the MCS framework proposed in chapter 3 w.r.t. a gold standard SS. For this purpose, two prototypes of affordable, portable, and user-friendly VIMUs-based MCSs have been developed and used to estimate upper and lower-limbs 3D joint kinematics of several healthy subjects performing different ADL movements.

In a first study, upper-limbs joint kinematics were estimated using a wired VIMUs-based MCS prototype and a one sensor per segment configuration during daily rehabilitation tasks based on the MFT. Prior to the joint kinematics estimation, two types of affordable and practical calibrations were used: a sensor-specific VIMUs calibration without using any external equipment, and a subject-specific VIMUs-to-segments local poses calibration taking advantage of the AR markers poses with no need to a predefined set of calibration postures/movements. The calibrated data were fused using a CEKF taking into account the physiological RoM of the joints to be estimated, which allows handling the inaccuracies due

to affordable sensors, particularly the IMUs drift and AR markers occlusion. The accuracy of the proposed affordable MCS obtained for seven upper-limbs joint angles estimates showed a low average RMSD below 3deg along with a high CC greater than 0.87. Results also showed the robustness of the proposed system to extended AR markers occlusion.

To improve the usability of the proposed MCS, the objective of the second study was to estimate gait kinematics based on a reduced count of newly designed wireless VIMUs sensors. Thanks to the VIMUs three-markers-bracelet design, AR markers occlusion was greatly limited. Besides, new constraints were implemented into the CEKF. Among these, VIMUs rigid body constraints were used as accurate and constant pseudo-measurements in the CEKF, which allows reconstructing a marker loss based on its non-occluded partners within the same VIMU. This was possible as the rigid transformation between each two VIMU markers was priory calibrated. To solve kinematics indetermination due to the reduced sensors-count configuration while further reducing the effect of IMU drift, joint soft constraints were also incorporated into the CEKF. Moreover, two formulations of the proposed state vector were studied and compared: a classical constant acceleration model associated with an optimal tuning process of the CEKF parameters, and a model based on a Fourier series expansion, which allows a simple tuning of the CEKF parameters based on a priori knowledge. Eighteen lower-limbs joint kinematics, as well as stride lengths and GDI, were estimated and compared to the SS. Results showed the ability of the proposed affordable VIMUs-based MCS to provide relevant kinematic information that might be of great benefit to the clinical community.

Final validation of the proposed system has to be performed with patients in a clinical environment. Final validation of the proposed system has to be performed with patients in a clinical environment. Moreover, given that the proposed calibration method is off-line, an automatic VIMUs-to-segments calibration would be of great interest to estimate online joint kinematics while compensating the effect of STA.

Chapter 5

Kinematics and Kinetics Assessment of a Human Augmented Motion

Exoskeletons are redundant structures inspired from human morphology and often require model-based controllers to assist the wearers achieving daily live activites. Physical interaction between the robot and the human should be transparent and smooth. Hence, an accurate human-exoskeleton model, which relies in part on an accurate knowledge of both kinematic and BSIPs, is of great importance to ensure reliable and robust performances of such controllers. It is also required to estimate human joint torques, which are widely used to infer the wearer's motion intention, and/or to calculate the needed assistive torques that should be provided by the exoskeleton to correctly achieve a given task.

As stated in section 2.5, human-robot joint misalignment is among the open challenges hindering a complete kinematic symbiosis between the exoskeleton and the wearer. Being inevitable in practice, this misalignment is often not taken into account in the literature, which may cause partial loss of the input assistive torque that could be transferred to the wearer's joints, and even in some cases such joint misalignment could result in undesired generated torques that could hinder the wearer's movement. [185].

In this context, this chapter investigates two different aspects of a human-robot interaction scheme. Section 5.1 presents a further experimental validation of the previous Motion Capture System (MCS) for BSIPs identification of the human body wearing a full lower-limbs exoskeleton robot. This study was published in the IEEE International Conference on Robotics and Automation (ICRA) 2018 [18]. Whereas, section 5.2 proposes an assessment framework of the kinematic and dynamic inaccuracies within a human-orthosis dynamic model for knee joint flexion/extension movements. The goal of such a framework is to provide the best trade-off between accuracy and simplicity of modelling of the human-orthosis system.

This study was published in the IEEE International Conference for Biomedical Robotics and Biomechatronics (BioRob) 2020 [19].

5.1 Human-Exoskeleton System Dynamics Identification Using Affordable Sensors

Within the same context of using affordable and portable sensors, this study presents the experimental results of affordable dynamic identification obtained with a subject wearing the Exoskeletal Robotic Orthotics for Walking Assistance (E-ROWA) exoskeleton that has been developed in the LISSI lab of the University of Paris-Est Créteil. In the following, we will present the human-exoskeleton mechanical and identification models, as well as joint kinematics estimation based on AR markers only. We will present as well the experimental setup and the corresponding results.

5.1.1 Method

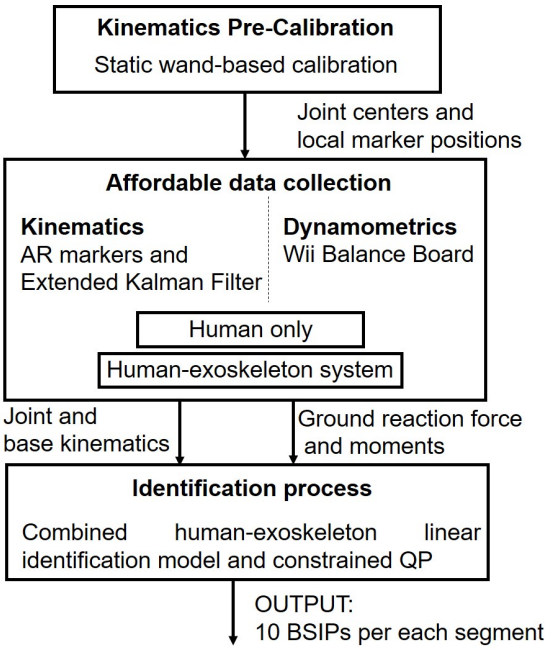

Fig. 5.1 System overview including both motion capture and identification pipelines.

The proposed method (Fig. 5.1) aims at identifying the BSIPs of the human-exoskeleton lower-limbs system using affordable sensors. Both base and joint kinematics were first estimated based on AR markers 3D Cartesian positions, tracked with a single affordable

RGB camera, together with the CEKF framework described in section 3.4 and based on the lower-limbs kinematic model. Kinematic data, together with the Ground Reaction forces and Moments (GRFM) data recorded using an affordable Wii Balance Board (WBB), were then introduced into a linear identification pipeline based on section 3.3. All data were collected for exciting motions performed in two cases: by the human alone and while wearing the exoskeleton.

5.1.1.1 Human-Exoskeleton Lower-Limbs Mechanical Models

Two models, of the E-ROWA exoskeleton (Fig. 5.2.a) and of the human lower-limbs (Fig. 5.2.b), were devised. They consist of $N_J = 20$ DoFs, and of $N_{LE} = 11$ and $N_{LH} = 7$ rigid segments, respectively. The E-ROWA is largely non-actuated with sixteen out of the twenty DoFs, i.e., except for both hips and knees flexion/extension, being passive. As it regards the human model, the head, arms, and trunk considered as one single segment for sake of simplicity as the upper body limbs were not assisted by the robot. The Modified Denavit Hartenberg notation was used to calculate the Forward Kinematic Model (FKM) (Eq. 2.2) and dynamic model (Eq. 2.9) [67]. The FKM allowed calculating the 3D pose of five frames attached to the model and used to represent the measured AR markers poses (see Fig. 5.2 and section 5.1.2).

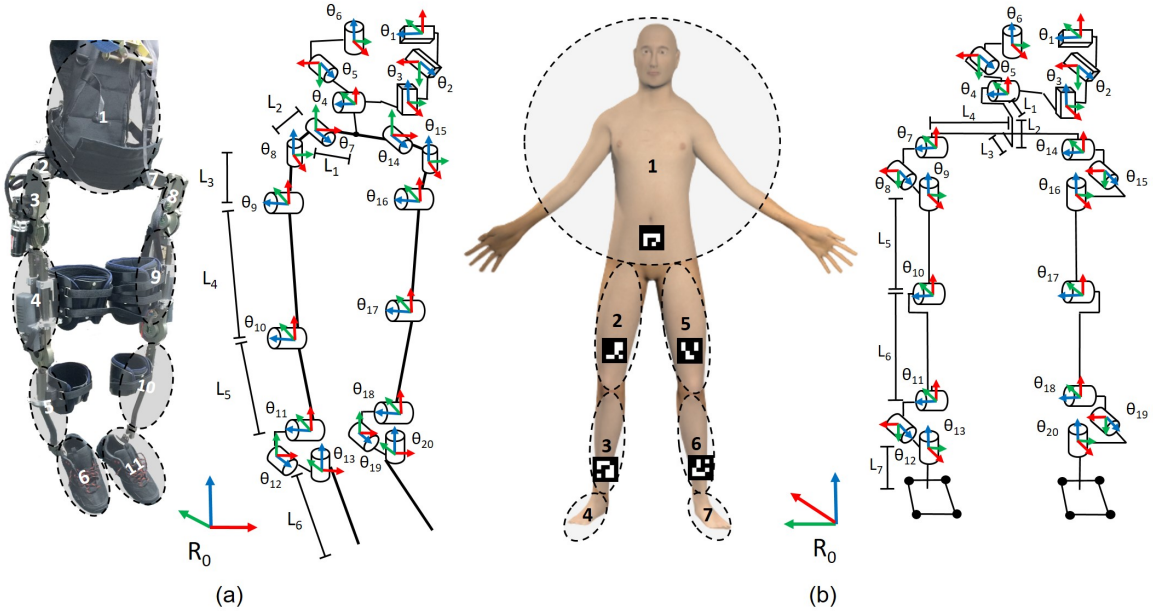

Fig. 5.2 Mechanical models of (a) the E-ROWA exoskeleton ($N_J = 20$, $N_{LE} = 11$) and (b) the human lower-limbs ($N_J = 20$, $N_{LH} = 7$).

5.1.1.2 Human-Exoskeleton Identification Model

Based on Eq. 3.19, the inverse dynamic model of a floating base system can be represented as a linear function of the BSIPs to be identified. In the case of this study, two different sets of dynamics equations for both human body and exoskeleton could be separately formulated, as follows:

$$\mathbf{W}_H \mathbf{\Phi}_H = \sum_{k=1}^{N_c} \mathbf{J}_{Hw_k}^T \mathbf{F}_k \tag{5.1}$$

$$\mathbf{W}_E \mathbf{\Phi}_E = \sum_{k=1}^{N_c} \mathbf{J}_{Ew_k}^T \mathbf{F}_k \tag{5.2}$$

where the indexes H and E denote the human and the exoskeleton, respectively. Unlike the human body, the E-ROWA exoskeleton could not support its own weight to perform exciting motions. As a result, the identification of its full set of standard BSIPs $\mathbf{\Phi}_E$ cannot be done alone. To cope with this issue, an augmented regressor matrix was proposed to identify the BSIPs of the whole system consisting in the human wearing the exoskeleton, and is given below:

$$\mathbf{W}_{HE} \mathbf{\Phi}_{HE} = \begin{bmatrix} \mathbf{W}_H & \mathbf{0} \\ \mathbf{W}_H & \mathbf{W}_E \end{bmatrix} \mathbf{\Phi}_{HE} = \sum_{k=1}^{N_c} \mathbf{J}_{HEw_k}^T \mathbf{F}_k \tag{5.3}$$

where $\mathbf{W}_{HE}$ and $\mathbf{J}_{HE} = [\mathbf{J}_H \quad [\mathbf{J}_H \mathbf{J}_E]]$ are the human-exoskeleton regressor and Jacobian matrices, respectively. $\mathbf{\Phi}_{HE} = [\mathbf{\Phi}_H \quad \mathbf{\Phi}_E]$ includes all $((10N_{LE} + 10N_{LH}) \times 1)$ standard BSIPs of both human and exoskeleton models.

Since $\mathbf{W}_{HE}$ is not of full rank, $\mathbf{\Phi}_{HE}$ was identified using the constrained Quadratic Programming (QP) method based on Eq. 3.28 [155]. Note that $\mathbf{\Phi}_{REF}$ $((10N_{LE} + 10N_{LH}) \times 1)$ in this study refers to the BSIPs values obtained from Dumas et al. [167] Anthropometric Tables (AT) for human and from the manufacturer Computer Aided Design (CAD) data for the E-ROWA exoskeleton. The exoskeleton CAD files, however, were not fully provided with only partial information available. This emphasized that the reference CAD data from the exoskeleton suffered from inaccuracies and they should not be trusted in practice.

5.1.1.3 Lower-Limbs Kinematics Estimation

The identification process requires as inputs the kinematics of the base segment and the joint kinematics of both human and exoskeleton models. One AR marker per segment configuration (see Fig. 5.3) was therefore used to estimate these measures, provided that each marker's 3D pose was tracked using a single RGB camera together with the ArUco

algorithm [94]. Note that the exoskeleton's and the wearer's body segments were considered rigidly connected. The movement of the human-exoskeleton system was therefore measured by tracking the pose of the markers associated to the wearer's body.

Prior to data collection, the lower-limbs mechanical model was first calibrated. Thus, the static wand-based calibration was used to estimate the position of the human joint centers, in the global system of reference, the segments lengths, and the local position of AR markers in their corresponding segment frames. These parameters were also used to estimate joint angles and in the calculation of the regressor matrix.

Based on the measured 3D positions of AR markers and the lower-limbs mechanical model, a CEKF was implemented as shown in section 4.1. Thus, the state vector provided the required lower-limbs joint trajectories to be estimated, whereas the measurement vector consisted in AR markers 3D positions, as follows:

$$\begin{aligned} \mathbf{x}_{i,k} &= [\theta_{i,k} \quad \dot{\theta}_{i,k} \quad \ddot{\theta}_{i,k}]^T \\ \mathbf{y}_k &= [\mathbf{r}_s^0] \\ \text{with} \quad & i = 1, ..., N_J \end{aligned} \tag{5.4}$$

The FKM-based measurement model provided the position of each marker as a function of the state vector, while the process model was assumed as a constant acceleration model as shown in Eq. 4.3. Lower-limbs joint constraints were incorporated into the CEKF, and tuning of $\mathbf{Q}$ and $\mathbf{R}$ parameters tuning was empirically conducted.

5.1.2 Experimental Protocol

The proposed framework, depicted in Fig. 5.1, was used to identify the BSIPs of a subject (weight=51Kg, height=1.65m) wearing the E-ROWA exoskeleton.

The accuracy of a WBB, used to collect dynamometric data, has been analyzed and shows an RMS error of 10N [186], which is relatively small compared to the weight of the subject-exoskeleton system (inferior to 1.5% of the total weight). However, as mentioned previously (see section 2.3.3), a WBB measures only the vertical ground reaction force. Thus, only the vertical force and two moments of force are provided, such that the vector of dynamometric measurements becomes $\mathbf{F}_k = [F_{Zk} \quad M_{Xk} \quad M_{Yk}]^T$.

As it regards the kinematics, five (8cm×8cm) AR markers were attached to the waist, and to the right and left thigh and shank segments, as shown in Fig. 5.3. Their 3D poses were obtained from ArUco library [94] in the camera frame, and transformed into the global system of reference frame using the estimated pose from another AR marker located between the subject feet (see Fig. 5.3). The two feet were assumed to be fixed to the ground, such

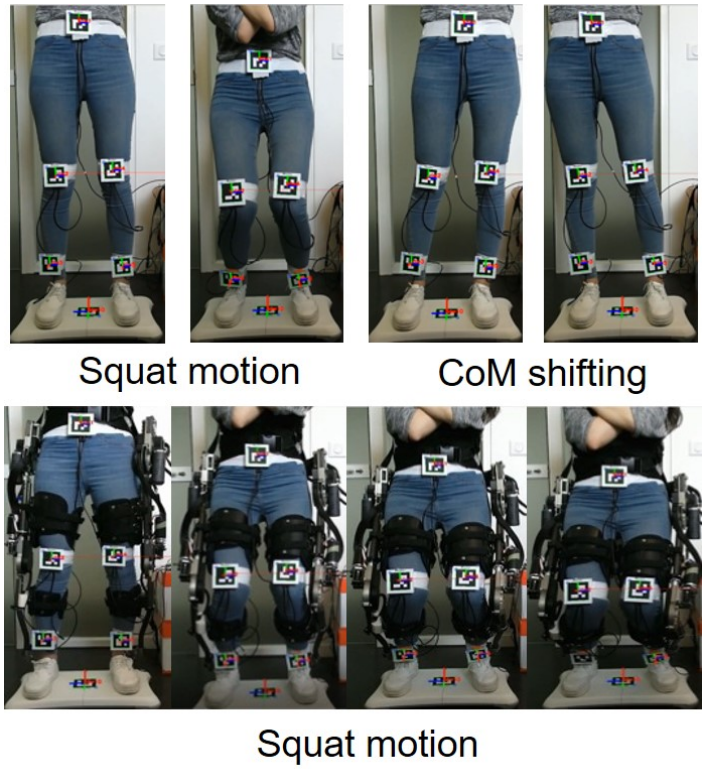

Fig. 5.3 Typical excitation motions performed first without and then with the exoskeleton.

that their positions in the global system of reference were supposed known and constant throughout the experiments. This was motivated by the fact that it was challenging to perform exciting motions on the reduced base of support created by the WBB. Note that the static feet assumption suggests that their inertias would not be identifiable. Nevertheless, Futamure et al. [223] showed that the feet inertial parameters have insignificant influence during walking.

The calibration phase was first conducted by pin-pointing each of the lower-limbs joints anatomical landmarks. The kinematics and dynamometric data were then collected synchronously at a sampling frequency of 27Hz and used to perform the identification of the subject first and then, of the subject wearing the E-ROWA exoskeleton. The subject was trained to conduct a set of specific motions that sufficiently excite the required BSIPs. These are displayed in Fig. 5.3 and consisted in a series of squats, CoM shifting under each foot, and postural and trunk oscillations. During each motion, the subject was asked to keep her arms around her chest, since the arms were not taken into account in the model. Such motions were inspired from the previous work of Bonnet et al. [175] on the generation of optimal exciting motions and showed good ability of providing rich kinematic information for the BSIPs estimation.

5.1.3 Results and Discussion

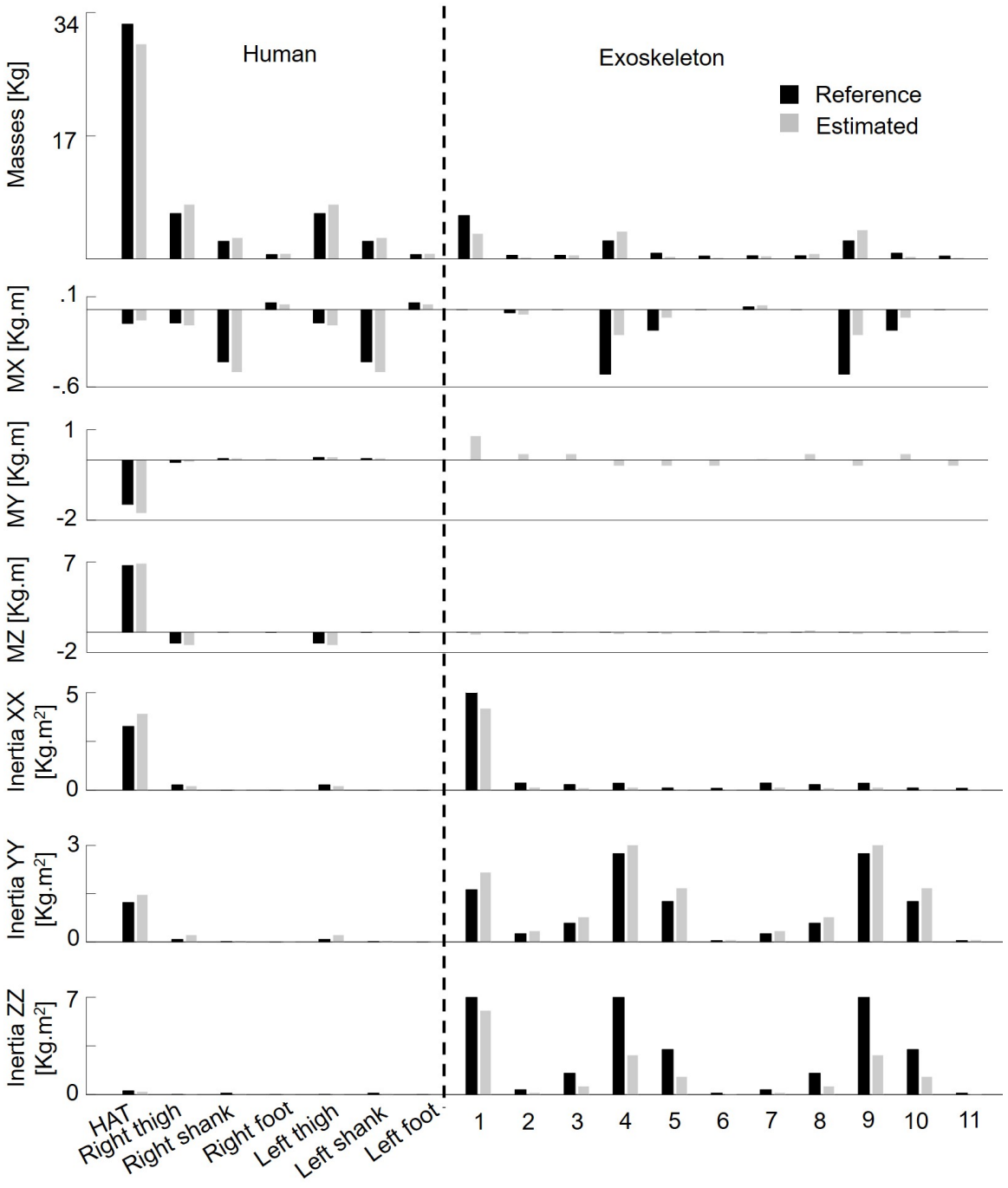

Fig. 5.4 Comparison between the estimated mass, CoM 3D position and inertia matrix elements for each segment of both human and exoskeleton models with their corresponding reference values from either AT or CAD data.

Fig. 5.5 shows the comparison between the measured GRFM collected during both experiments carried out with the human only (left side) and with the human-exoskeleton (right side), and their estimate using the identified model. Since the measured GRFM were used in the least-square based identification process (see Eq. 3.28), the fitting is expected to be satisfactory. The fitting accuracy was assessed by calculating the RMSD, the Normalized RMSD (NRMSD) and the CC between measured and estimated GRFM. The obtained results are summarized in Table 5.1 for both human and human-exoskeleton systems. Given the WBB accuracy of 10N, these estimates can be considered as satisfactory. The corresponding BSIPs, obtained based on Eq. 3.28, are depicted in Fig. 5.4 for both models and compared with their corresponding reference ones form either AT or CAD data. The subject estimated parameters and AT-based parameters were relatively close to each other as shown in Fig. 5.4 with the same order of magnitude. However, as it regards the exoskeleton, the CAD values could not be sufficiently trusted due to their inaccuracy. For instance, a very large difference up to 58% of the first segment's mass was reported. Similarly, most of the CoM, i.e., first moment of inertia, along X and Y-axes were associated with significant differences since they were not provided by the manufacturer.

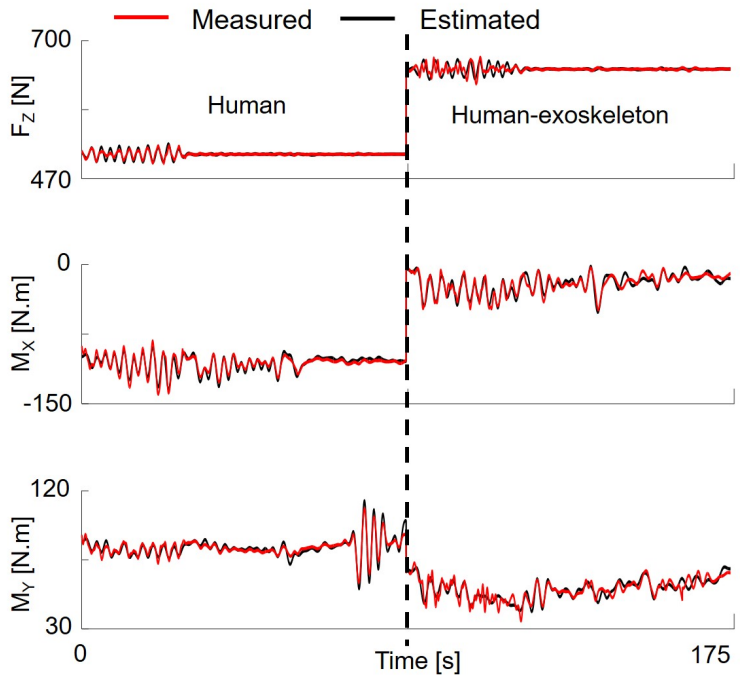

Fig. 5.5 Vertical ground reaction force and moments measured (black) during the identification motion and their estimate (red) from the identified model.

To evaluate the performance of the identified model, a cross validation, including motions that were not used during the identification process of the human-exoskeleton system, was

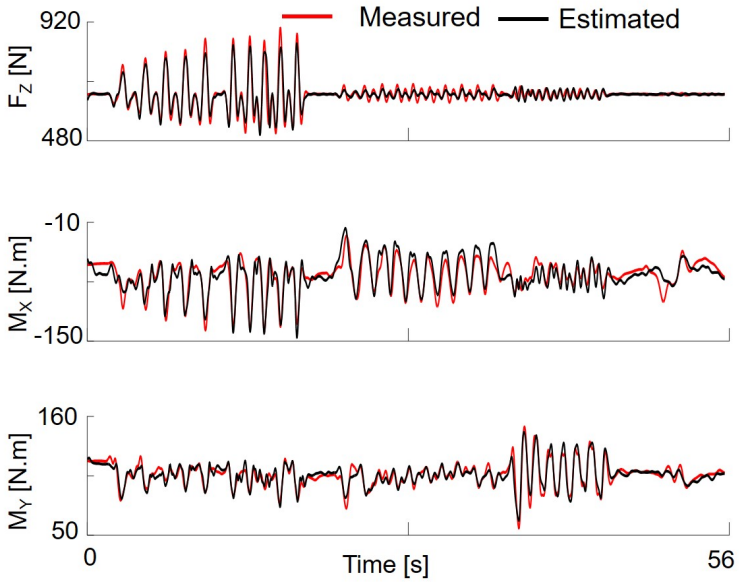

Fig. 5.6 Cross validation of the external vertical force and moments estimation involving additional motions not performed during the identification process of the human-exoskeleton system.

done. As shown in Fig. 5.6, the identified model was able to provide reliable estimates of the GRFM. The corresponding RMSD and NRMSD values, summarized in table 5.2, present relatively larger differences along $\mathbf{F}_Z$ (11.2N, 2.2%) and $\mathbf{M}_X$ (7.9N.m). However, considering the WBB accuracy, this difference remains reasonable. A similar comparison was not conducted w.r.t. the CAD data because of the incomplete set provided by the manufacturer. We note that the average NRMSD was only of 5.7% with the most significant difference observed for the moment around the X-axis (11.2%).

Table 5.1 Comparison between the measured and estimated GRFM collected during the identification motions.

	Human			Human-Exoskeleton		
	RMSD	NRMSD %	CC	RMSD	NRMSD %	CC
Fz	2.2 N	0.43	0.88	5.4 N	0.8	0.49
Mx	3.3 N.m	3.1	0.92	4.2 N.m	18.3	0.91
My	2.1 N.m	2.5	0.95	3.1 N.m	5.6	0.88

As a result, both the visual tracker system as well as the proposed identification method were experimentally validated to identify the full set of the human-exoskeleton BSIPs.

Table 5.2 Comparison between the measured and estimated GRFM collected during cross validation motions.

	Human-Exoskeleton		
	RMSD	NRMSD (%)	CC
Fz	11.2 N	2.2	0.94
Mx	7.9 N.m	11.2	0.88
My	4.2 N.m	3.9	0.92

5.2 Dynamics Assessment and Minimal Model of an Orthosis-Assisted Knee Motion

In the previous study, both exoskeleton and wearer's limbs were assumed rigidly connected for BSIPs identification, which is commonly used in the literature [48]. For further simplification, human joint torque is usually investigated based on a planar model of the human-robot system [14, 224, 225]. The goal of the present study is to analyze how such assumptions may affect the accuracy of joint torque estimation.

In this context, an assessment framework has been proposed, and preliminary exemplified in the case of a knee joint orthosis during movement of flexion/extension. It aims at selecting the minimal dynamic model, while allowing relative accurate joint torque estimation, of an orthosis-assisted motion through:

- quantification of the human-orthosis misalignment during the motion,
- quantification of misalignment influence over joint torque estimate,
- selection of the best trade-off between accuracy and simplicity of the dynamic model.

The methodology used to answer to these questions may be generalized to any orthosis or exoskeleton robot. However, the present study focuses on knee joint misalignment and torque. In the following, we present the proposed analysis method, including human/orthosis mechanical models, joint axes misalignment, and the influence of both kinematic and dynamic parameters inaccuracies. Experimental results are presented as well and discussed.

5.2.1 Method

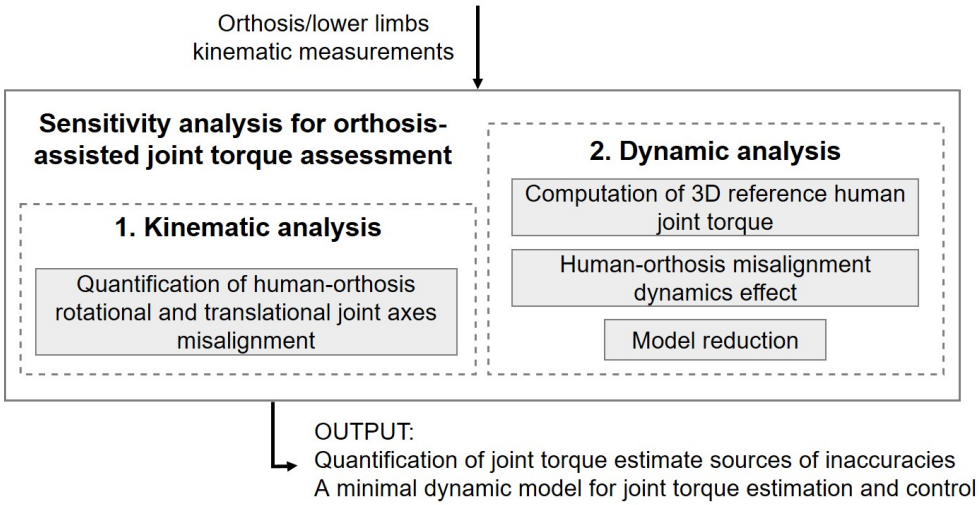

Fig. 5.7 Overview of the proposed framework including kinematic and dynamic sensitivity analyses.

The overall principle of the proposed framework is summarized in Fig. 5.7. It consists of a two-fold assessment study aiming at quantifying the sources of inaccuracies that may affect joint torque estimation. First, a kinematic analysis aims at quantifying the human-orthosis joint axes misalignment during a knee flexion/extension motion. The effect of this misalignment, as well as the independent contribution of both kinematic and dynamic parameters to joint torque estimate, are then assessed through a two-step dynamic sensitivity analysis. Finally, a dynamic model resulting from the best trade-off between accuracy and simplicity can be selected.

5.2.1.1 Human/Orthosis Lower-Limbs Mechanical Models

The proposed framework was exemplified using the knee joint orthosis EICOSI (Exoskeleton Intelligently COmmunicating and Sensitive to Intention designed at the LISSI lab of the University of Paris-Est Créteil.), and two different models of the human lower-limbs performing sitting knee flexion/extension motion. The EICOSI orthosis consists of two segments, attached at the thigh and at the shank levels, articulated with one active DoF at the knee joint level. It is connected to the wearer's limb through braces, and it weighs about 3Kg (see Fig. 5.8.a).

Two mechanical models were used to represent the human-orthosis system: (1) a planar model with $N_J = 1$ DoF describing the flexion/extension movement of the shank segment ($N_L = 1$) w.r.t. a fixed base frame located at the knee (see Fig. 5.8.b). (2) A 3D reference

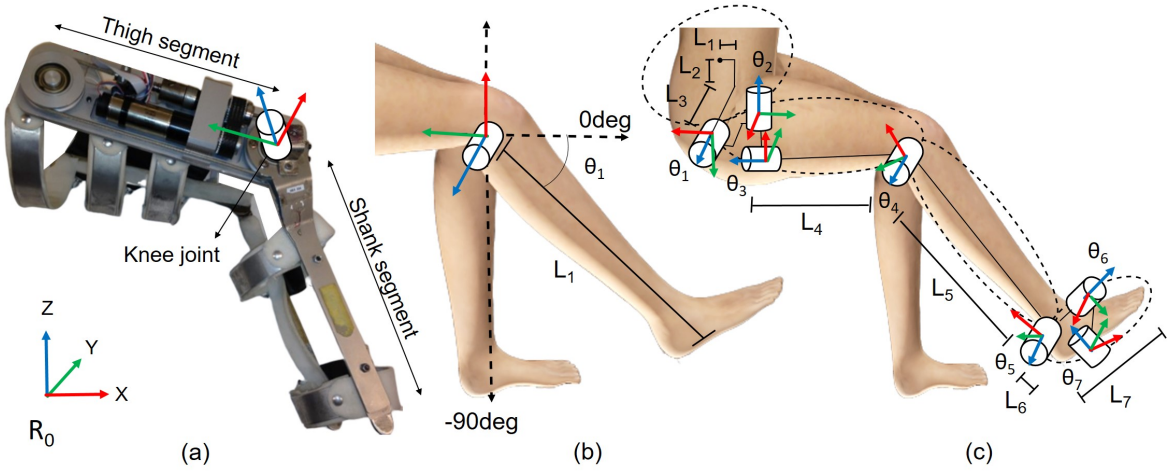

Fig. 5.8 (a) Mechanical model of the EICOSI knee joint orthosis. (b) Lower-limb 2D model composed of $N_L = 1$ shank-foot segment and $N_J = 1$ knee flexion/extension joint. (c) Lower-limbs 3D reference model with $N_L = 4$ segments and $N_J = 7$ joint angles.

model describing the entire lower-limb motion, and composed of $N_L = 4$ rigid segments, i.e., pelvis, thigh, shank, and foot, connected through $N_J = 7$ DoFs, i.e., two spherical joints at the hip and ankle joints and one hinge joint at the knee joint level (see Fig. 5.8.c). The Modified Denavit Hartenberg notation, together with SYMORO+ software [67], were used to calculate the dynamic equations of motion. The human BSIPs were set using AT [167].

The resulting system corresponds to a standard serial robotic chain composed of N_L rigid segments and N_J joints and thus its inverse dynamics is typically given as [67]:

$$\mathbf{\Gamma} = \mathbf{M}(\boldsymbol{\theta})\ddot{\boldsymbol{\theta}} + \mathbf{C}(\boldsymbol{\theta}, \dot{\boldsymbol{\theta}})\dot{\boldsymbol{\theta}} + \mathbf{G}(\boldsymbol{\theta}) \tag{5.5}$$

where $\mathbf{M}(\boldsymbol{\theta})$ is the $(N_J \times N_J)$ chain segments inertia matrix; $\mathbf{C}(\boldsymbol{\theta}, \dot{\boldsymbol{\theta}})$ is the $(N_J \times N_J)$ matrix of Coriolis and centrifugal torques; and $\mathbf{G}(\boldsymbol{\theta})$ is the $(N_J \times 1)$ vector of gravitational torques. As it regards the planar model, the gravity vector was assumed constant and vertical throughout the movement, whereas for the 3D model, it was projected according to the moving base frame located at the pelvis. The kinematic misalignment between the wearer and the orthosis joints will be evaluated in the next section.

5.2.1.2 Kinematic Analysis Method

The kinematic analysis in this study aims at quantifying the joint axes misalignment that might be observed despite a careful initial adjustment between the orthosis and the body of the subject. Thus, both orthosis and wearer knee joint AoR were individually estimated

using SARA [192] (see section 3.2.2), together with the stereophotogrammetric data used as reference system and recorded during knee flexion/extension movement.

Knee Joint Axes Misalignment Using SARA, the direction vectors of the AoR of the human ($\mathbf{d}_H^0$) and of the orthosis ($\mathbf{d}_O^0$) can be estimated and expressed in the global coordinate system (see Eq. 3.15). The orthosis-wearer joint misalignment can therefore be evaluated as the rotation matrix that aligns these two vectors, such as:

$$\mathbf{d}_H^0 = \mathbf{R}_H^O \, \mathbf{d}_O^0 \tag{5.6}$$

where $\mathbf{R}_H^O$ is the rotation matrix going from $\mathbf{d}_O^0$ to $\mathbf{d}_H^0$ as shown in Fig. 5.9. $\mathbf{R}_H^O$ has infinite solutions, though one possible solution may be calculated as [162]:

$$\mathbf{R}_H^O = \mathbf{I_d} + \mathbf{E} + \mathbf{E}^2 \frac{(1 - \mathbf{d}_O^0 \,.\, \mathbf{d}_H^0)}{\| \mathbf{d}_O^0 \times \mathbf{d}_H^0 \|^2} \tag{5.7}$$

with $\mathbf{E}$ referring to the skew matrix corresponding to the cross product of both $\mathbf{d}_O^0$ and $\mathbf{d}_H^0$ vectors.
To better understand the misalignment effect, the above analysis was performed as a function of the knee active RoM.

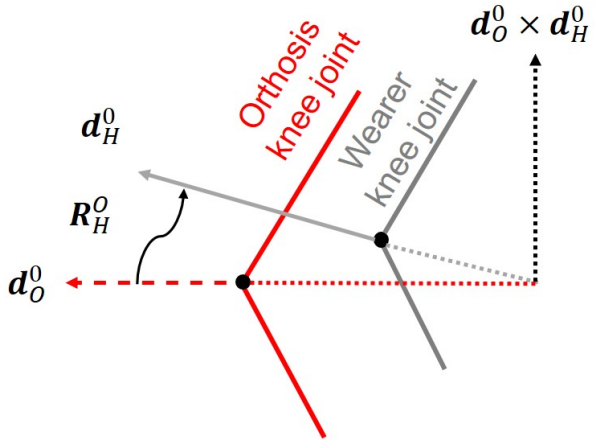

Fig. 5.9 Representation of the misalignment between the direction vectors of both orthosis and wearer AoR expressed in the global coordinate system through the rotation matrix $\mathbf{R}_H^O$.

5.2.1.3 Dynamic Analysis Method

Misalignment Effect Considering the rotation matrix $\mathbf{R}_H^O$, representing the misalignment between the wearer and the orthosis AoR, the effect of this misalignment may be straightforwardly assessed. This can be done by computing the residual torques, that are supposed to represent the components of the assisted torques that are not aligned with the wearer AoR, as follows:

$$\mathbf{\Gamma}_H = \mathbf{R}_H^O \begin{bmatrix} 0 \\ 0 \\ \tau_A \end{bmatrix} \tag{5.8}$$

where $\mathbf{\Gamma}_H$ is the vector of residual torques, i.e, about the X (internal/external rotation) and Y (adduction/abduction rotation) axes projected according to $\mathbf{R}_H^O$, and τ_A is an input assistive torque generated about the orthosis joint axis.

Sensitivity Analysis and Model Reduction The goal of this section is to analyze how each of the joint kinematics and BSIPs contribute to the 3D knee joint torque estimate. To this end, a two-step sensitivity analysis was conducted, such that the minimal set of parameters required to ensure the best trade-off between an accurate and minimal dynamic model can be selected. First, the influence of each element of the joints angles vector $\boldsymbol{\theta}$ (see Fig. 5.8.c) was individually assessed. Particularly, those associated with hip and ankle motion were forced to zero. Then for each case, the corresponding knee joint torque was compared with the one obtained from the 3D computation without any alteration of the human-orthosis model. In a second step, the contribution of each BSIP Φ_i to the joint torque estimation was evaluated, thanks to the linear property of the dynamic model w.r.t. these parameters (see Eq. 3.19), such as:

$$\mathbf{W}\Phi_i = \Gamma_i \quad i = 1, .., 10 \times N_L \tag{5.9}$$

As shown in [223], Eq. 5.9 yields a normalized sensitivity index, given as:

$$S_{\Gamma_i} = \sum \frac{|\, \mathbf{W}\Phi_i \,|}{|\, \mathbf{\Gamma} \,|} \quad i = 1, .., 10 \times N_L \tag{5.10}$$

5.2.2 Experimental Protocol

Experiments were carried out to assess the proposed framework in the case of the human-orthosis model while performing standardized sitting knee flexion/extension movements. Throughout the experiments, the EICOSI knee joint orthosis operated in passive mode, i.e., no assistive torque was transferred to the wearer's knee joint. The orthosis and wearers

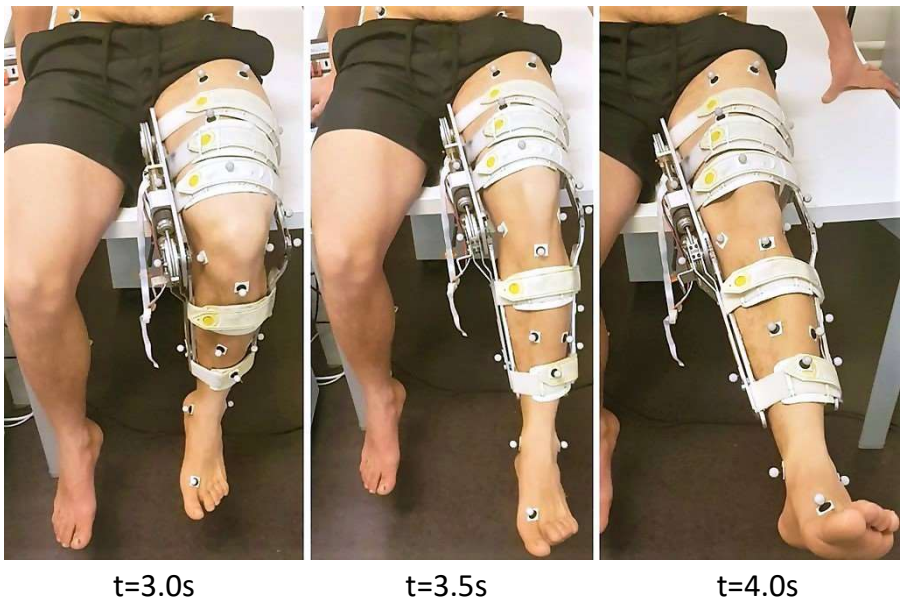

Fig. 5.10 Knee flexion/extension while wearing the knee joint orthosis EICOSI. Retro-reflective markers are placed on both orthosis and subject left lower-limbs.

motions were captured at a frequency rate of 120Hz using a standard SS (7 Flex 13 cameras, Optitrack). A total of twenty-four retro-reflective markers, i.e., with at least three markers per segment, were used to define each segment's 3D position of both orthosis and wearers left leg (see Fig. 5.10). The pelvis pose was calculated from markers placed on the right-left ASIS and PSIS anatomical points (see Fig. 2.5.b). The Hip Joint Center (HJC) position was priorly estimated using the SCoRE method [191] from section 3.2.2, together with star-arc motions [226]. The knee and ankle joint centers were considered as the mid-points between LFE-MFE and LM-MM (see Fig. 2.5.b), respectively. From these positions, the average segment lengths were calculated over the whole motion.

Eight healthy male subjects (age 24.6 ± 5years, weight 67.6 ± 4Kg and height 1.74 ± 0.4m) participated in the study. The orthosis was carefully attached to the subjects left leg through adjustable straps without hindering their comfort throughout the knee joint flexion/extension movements. First, both orthosis and the wearers knee joint centers positions were manually aligned. Then, subjects were asked to perform ten standard knee flexion/extension movements while sitting. For each subject, two trials were recorded at slow and natural (1Hz) speeds.

Both orthosis and the wearers knee AoR were estimated using SARA with the 3D positions of the thigh and shank markers considered as inputs (see Eq. 3.14). In other terms, these segments transformation matrices, used in Eq. 3.14, were computed based on the three markers placed on each segment. This was done over the slow movement trials with the aim

to reduce the Soft Tissue Artifact (STA) effect due to muscle contractions. The STA due to skin stretching, however, is inevitable in practice and cannot be entirely avoided.

Afterwards, the human lower-limbs and the orthosis joint angles, describing the biomechanical models depicted in Fig. 5.8, were estimated using MKO [65] (section 3.5).

5.2.3 Results and Discussion

5.2.3.1 Human-Orthosis Knee Joint Misalignment

First, the AoR estimation was tested with the orthosis alone, i.e., without being worn by a subject. The EICOSI orthosis was therefore firmly attached to a table and the flexion/extension movements were executed. As a result, the mean variation of the AoR orientation estimate was very small (< 0.5deg), which is expected since the orthosis AoR, unlike the human one, does not vary while moving.

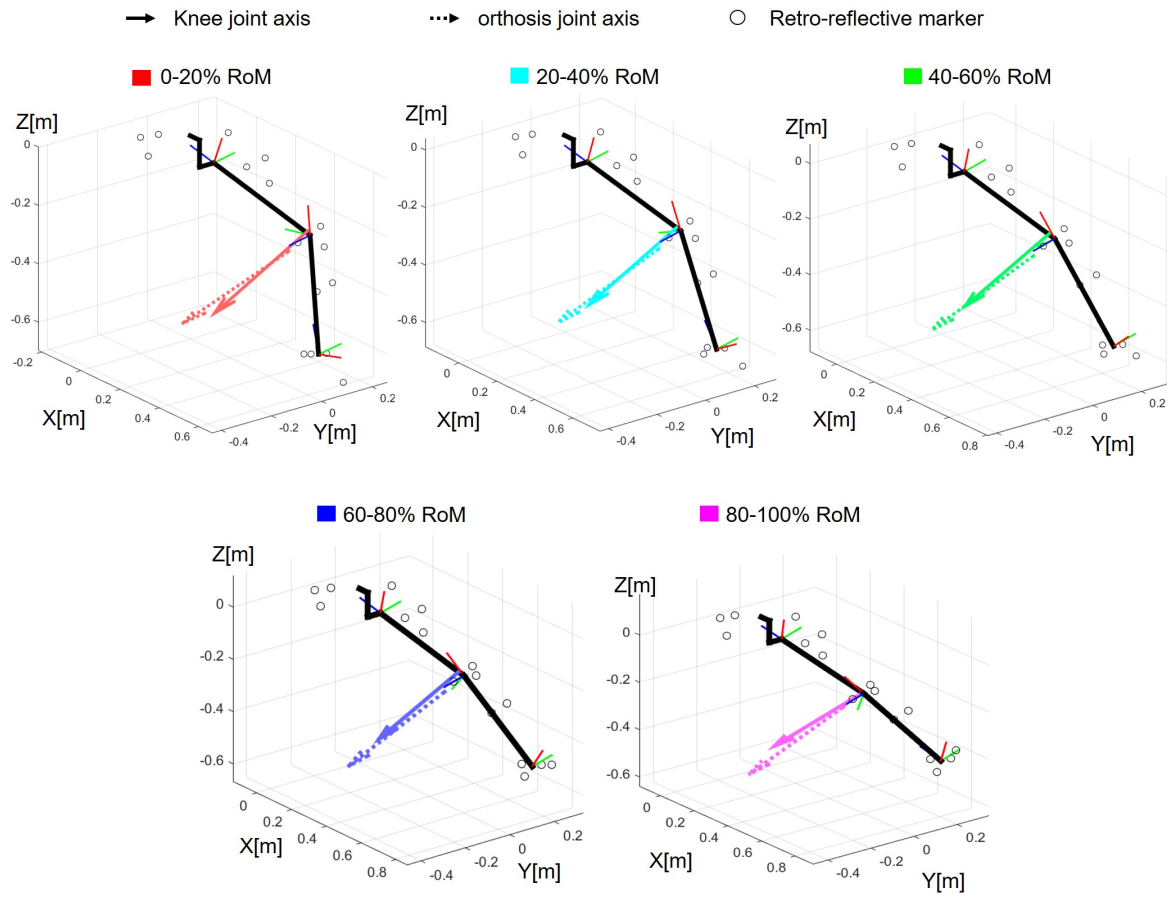

Fig. 5.11 Mean AoR of both knee (continuous arrow) and orthosis (dotted arrow) joints determined using the SARA as a function of the knee RoM of a random selected subject.

All subjects' knee movement ranged between -85 and 0deg, with 0 being the fully extended position (Fig. 5.8.b). The misalignment between each wearer's knee and the orthosis joint was evaluated over sub-intervals of 20% of their RoM. The 20% division was selected as a trade-off to sufficiently excite the SARA's estimate (Eq. 3.14), on the one hand, and to better understand the misalignment variation and effect throughout the movement, on the other hand. Fig. 5.11 displays a typical estimate of both knee and orthosis AoR through all sub-intervals (0% to 100%). As expected, variations in the AoR orientation were observed. The mean 3D deviations reported for all subjects in each sub-interval are presented in Fig. 5.12.a. In general, the AoR misalignment increased with the percentage of RoM. This is consistent with the literature where an increase up to 15deg of the knee AoR was reported using *in vivo* imaging techniques [227], [228]. The maximal deviation angle was of 11.43±2.9deg in the sub-interval 60 to 100%. As stated previously, the orthosis AoR, theoretically, remains invariant. Therefore, the variations in the orientation of the wearers AoR might be due to both the fact that the human knee is not a pure hinge joint, and to the fact that the relative movement of the skin and muscles may induce a motion of the orthosis w.r.t. the wearer's skeleton limb. Although the estimated AoR of both orthosis and the wearers were not aligned, the similar variation in the AoR orientation, with and without orthosis, suggests that the orthosis had limited effect on the subjects' natural motion pattern.

Besides the rotational misalignment, above, the misalignment translational component was also assessed by computing the relative mean distance between subjects' HJC and the Orthosis Joint Center (OJC) for each 20% sub-interval of the whole RoM, as shown in Fig. 5.12.b. These points were selected as they were assumed to be less sensitive to STA. The HJC-OJC distance was normalized w.r.t. its average value obtained statically. In general, it decreased from 101.1 ± 1.9 to 100.6 ± 1.3%, referring to a small displacement between 4.2 ± 7.5mm and 2.5 ± 5.2mm. This emphasizes that the orthosis was carefully attached to the subjects' limbs, such that the misalignment translational component due to STA could be compensated. In the literature, this component was assessed as the translation of a cluster of markers located at the thigh during different motor activities [229]. For instance, the translation due to STA was evaluated to $5-21$mm [230] with a high correlation with the knee flexion/extension angle during treadmill walking [229]. Despite the small-displacement values observed in the current study, it has been shown that undesired forces could arise at the thigh and shank attachment levels. Akiyama et al. [185] reported a force up to 30N beneath the thigh attachments for a relative longitudinal displacement of 20mm during sitting motions. With these measurements, they identified a "spring-damper and attitude" model to predict the interaction forces as a function of the robot-wearer relative displacement, as well as the knee flexion/extension angle. Based on their model, for a maximal current displacement of

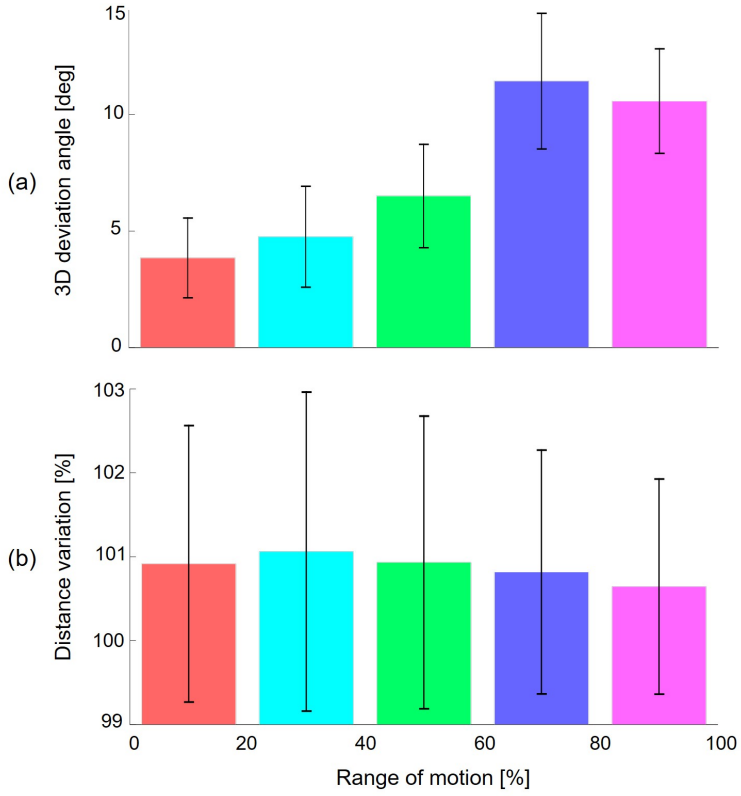

Fig. 5.12 (a) 3D deviation angle between both knee and the orthosis mean AoR as a function of the knee RoM for all eight subjects. (b) Mean distance variation from the wearer HJC to the robotic knee joint center as a function of the knee RoM.

11.7mm, corresponding to this study, we might expect a maximal force up to 20N along the thigh attachment point. Such forces, even if below any pain threshold, have been shown to have direct impact on the human skin morphology, especially in aged skin, when applied for an extended period of time [231].

To illustrate the effect of rotational AoR misalignment on knee joint torque estimate, a simulated assistive torque τ_A was assumed generated by the orthosis. Based on Eq. 5.6, Eq. 5.8, and the angular deviations depicted in Fig. 5.12.a, the residual torques about the X and Y-axes were estimated. The resulting torques are normalized and presented in Fig. 5.13 as functions of the percentage of knee RoM.

As expected, residual torques increased with the subject-orthosis AoR deviation. Although, 98±0.01% of the input assistive torque was transferred about the Z-axis, i.e., the knee joint axis, residual and undesired torques up to 6±0.03% and 17±0.04% were generated about the X and Y-axes, respectively. This suggests that for an assistive torque of 10N.m generated about the orthosis joint axis, undesired residual torque up to 1.7N.m might be expected the Y-axis (abduction/adduction rotation) of the wearer's joint.

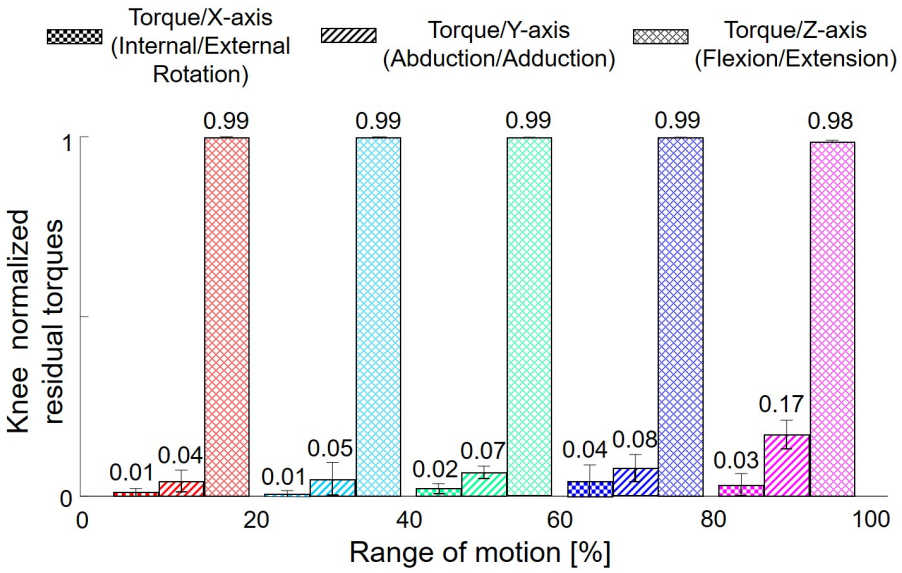

Fig. 5.13 Mean 3D residual torques expressed at the subjects knee joint as a function of the RoM.

In fact, the residual torques, together with the resultant interaction forces, assist in inferring the wearer's true intention, i.e., set of forces and torques that the wearer receives and generates, for a given motion. Hassani et al. [232] have shown the relevance of using such residual torques in generating a desired trajectory, instead of applying a predefined one, within an impedance-based control law. The latter aims at ensuring an adaptation to the orthosis-wearer interaction, and at the same time guaranteeing the system stability and robustness w.r.t. external disturbances and model uncertainties. Recently, Huo et al. [14] have modelled the residual error between both orthosis and wearer's joints positions. They used this error in an impedance reduction control scheme aiming at reducing the wearer interaction effort through active impedance assistance. However, the visco-elastic properties of each wearer's soft tissues would have to be priory calibrated based on force sensors measurements.

Thus, the orthosis-wearer time-varying rotational misalignment results in an inaccurate joint torque estimate during knee joint flexion/extension movements. Due to STA, it should be noted that the true knee flexion/extension axis could not be identified based on stereophotogrammetric data, thus remains unknown in this study. As shown in Fig. 5.12, the orthosis-wearer misalignment increased with the knee extension angle. These observations could be generalized to fit a polynomial-like model able to predict misalignment in a general model-based controller. Although being linear, such model has been proposed in the literature

[233], [234] to compensate for the effect of STA on thigh or shank skin marker positions, or the knee joint kinematics.

5.2.3.2 Kinematics and Dynamics Sensitivity Analyses for Model Reduction

This section presents the results of the sensitivity analysis studying the influence of both kinematics and dynamics parameters on the knee joint torque estimate. First, the independent contribution of the ankle and hip joint angles was assessed. Particularly, the variables θ_5, θ_6, and θ_7, referring to the ankle joints (see Fig. 5.8.c), were held to their initial values while comparing the value of the resulting torque estimate to the 3D reference one (see Fig. 5.14). Doing so, their influence was negligible as they alter the knee joint torque only by 0.01N.m. This suggests that these variables and their derivatives may be eliminated from Eq. 5.5 in the case of the sitting flexion/extension movements.

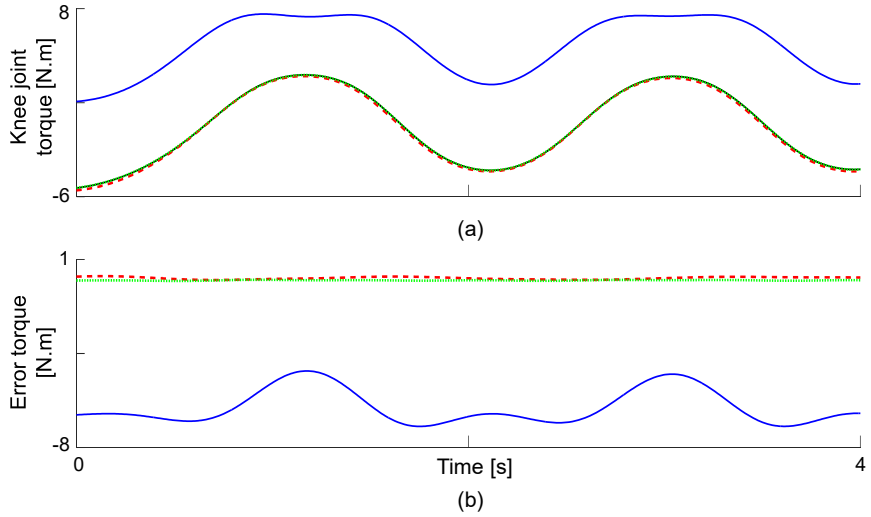

Fig. 5.14 (a) Comparison (b) Error torque between the knee joint 3D reference torque (black), the 3D torque without considering any ankle motion (dotted green), the 2D torques with (dashed red) and without (blue) gravity projection according to the thigh motion.

The hip joints influence was assessed by estimating the knee joint torque using the 2D lower-limb model (see Fig. 5.8.b) in two cases: without any motion of the hip and by projecting the gravity vector according to the hip motion. Fig. 5.14 provides a typical comparison between the resulting torques. Indeed, the influence of the thigh orientation was highly significant with a large RMSD of 6.1N.m between the reference knee joint torque and the 2D torque computed based on a constant and vertical gravity vector. When the gravity was projected according to the hip motion, a RMSD of only 0.12N.m was reported. For all subjects, RMSDs were of 0.10±0.01N.m and 6.15±0.73N.m, with and without considering

the hip motion, respectively. This yields the following findings: First, a lower-limb planar model can be used to obtain an accurate estimate of the knee joint torque. Second, the thigh absolute orientation must be measured and used to project the gravity vector accordingly.

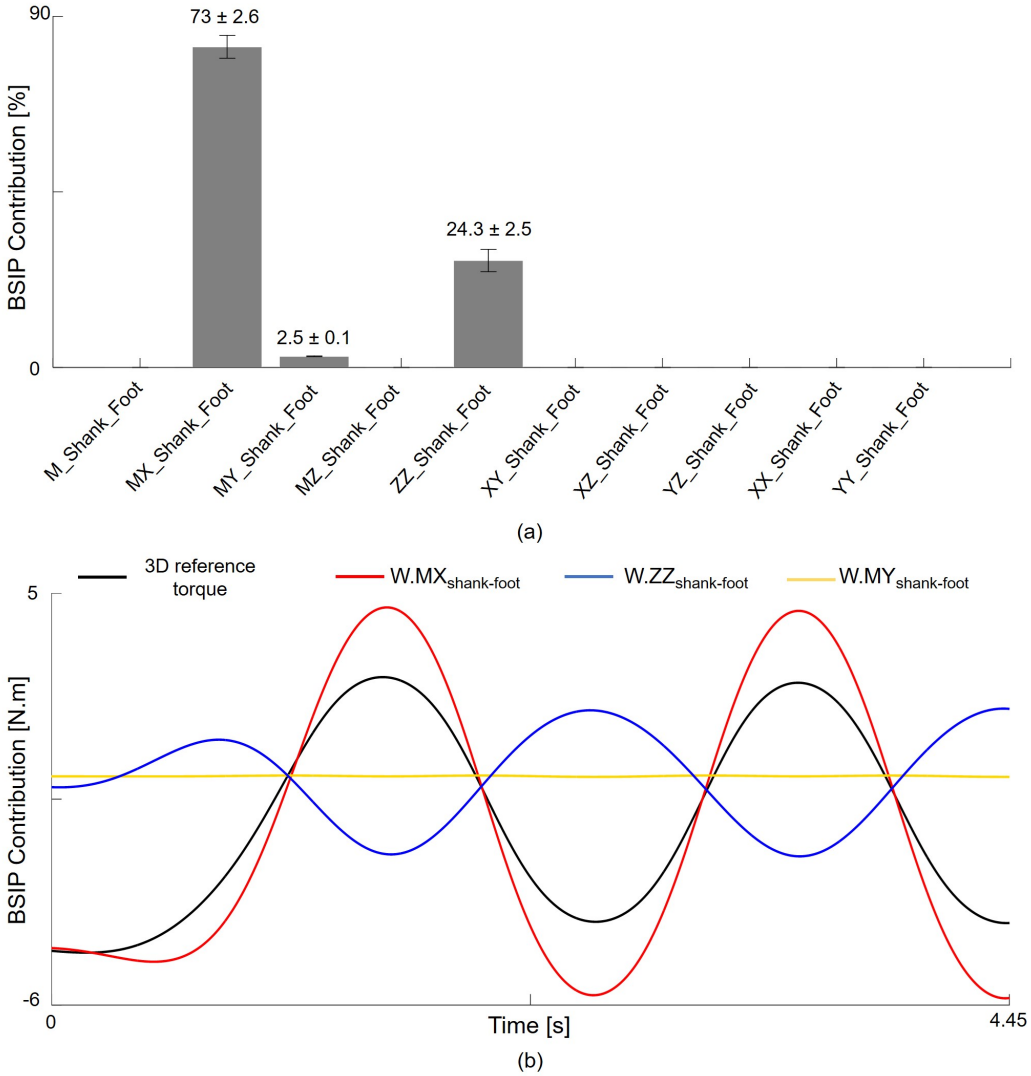

Fig. 5.15 (a) Mean contribution of each of the BSIPs to the knee joint torque estimate. (b) Reconstruction of the knee joint torque of a randomly selected subject based on the influential BSIPs of the combined shank-foot segment: MX (red), MY (yellow), and ZZ (blue).

In summary, for the investigated task, there is no need to use retro-reflective markers or any motion sensor at the ankle level. The markers associated with the pelvis can also be removed. On the other hand, the thigh orientation needs to be measured and used to project the gravity vector correctly. This can be achieved by adding three markers at the thigh in

addition to those placed at the shank. Also, low-cost sensors such as IMUs, AR markers, or a fusion of the two sensors presented in the previous chapter could be used.

In a second step, each BSIP influence was examined to further reduce the model's dimension. As the ankle motion was shown insignificant, the shank and foot segments were assumed as a single rigid segment. The BSIPs contributions to the knee joint torque estimate are depicted in Fig.2 for this segment. Note that the sum of the different joint torques shown in Fig.5.15.b is equivalent to the 3D reference torque represented by the black line.

Fig. 5.15.a presents the mean sensitivity index of each BSIP computed based on Eq. 5.10. Accordingly, the first moment of inertia in the sagittal plane and the moment of inertia about the knee AoR were the only parameters used to reconstruct the knee torque. As expected, most of the torque was due to the first moment of inertia, i.e., gravity-based parameters, with a total contribution of 75.5±2.7%. This confirms the large influence of the gravity projection demonstrated above. Among this contribution, the first moment of inertia along the X-axis constitutes 73±2.6%. Therefore, the moment along the Y-axis may also be neglected. Based on Fig. 5.15, it is therefore possible to state that the planar model hypothesis is valid in this particular case of flexion/extension movements without interaction with the ground. and that most of the BSIPs have a little influence on the joint torque estimate. Solely two out of forty parameters are sufficient to estimate 97.5% of the total knee torque.

Consequently, the 3D reference model (see Fig. 5.8.c), consisting in a total number of parameters of $3 \times N_J = 7$ for joint trajectories, i.e., joint angles, velocities, and accelerations, respectively, and of $10 \times N_L = 4$ for BSIPs, may be minimized to $3 \times N_J = 1$ and $2 \times N_L = 1$ parameters only. This minimal model, leading to the following equation, can reproduce 97.5% of the total knee joint torque estimate:

$$\Gamma = ZZ\,\ddot{\theta} + MX\,g_p \tag{5.11}$$

with Γ is the torque about the knee AoR. MX and ZZ are the first moment of inertia along the longitudinal axis of the shank-foot segment and the inertia moment about the knee AoR, respectively, and g_p is the projected gravity according to the thigh 3D orientation.

5.3 Conclusion

In this chapter, two different case studies of a human-robot motion have been conducted. First, a practical identification method has been presented and experimentally validated to identify the BSIPs of a human-exoskeleton system using affordable and easy-to-use sensors. Particularly, it uses kinematic and dynamometric data from a visual tracker system, that consists of camera-tracked AR markers, CEKF, and an affordable WBB. The fact of using

low-cost sensors does not jeopardize the accuracy of the identification process and the resultant inverse dynamics estimation. Indeed, the GRFM were estimated with less than 6% of difference when compared to the WBB's measurements. Although the resulting joint kinematics must be compared with those obtained using a reference laboratory SS, the consistent results obtained with inverse dynamics suggests that the proposed visual motion capture system shows satisfactory accuracy. Nevertheless, further validations need to be conducted with more subjects and patients. Moreover, the VIMUs-based MCS, presented in chapter 4, could be used to improve kinematics estimation while handling AR markers eventual occlusion in the case of more complex motions. Instead of the fixed feet assumption, the subject's base of support may also be modified by using forces sensors, such as FSR embedded in the shoes insoles.

In a second study, we have analyzed the possibility of reducing the human-robot dynamic model without considerably affecting the accuracy of the resulting joint torque estimate during knee joint flexion/extension movements. An assessment framework has been therefore developed to quantify human-robot joint axes misalignment during motion, as well as the independent contribution of kinematics and BSIPs to joint torque estimation. The proposed framework has been preliminarily exemplified in the case of healthy subjects wearing the EICOSI knee joint orthosis and performing standard sitting knee flexion/extension movements. According to the results, the wearer-orthosis joint axes misalignment increased with the knee RoM and reached an average maximal value up to 12deg at large extension angles. Also, a minimal dynamic model, of only two parameters, was sufficient to reconstruct 97.5% of the reference knee joint torque, computed based on the 3D reference model. Thus, to estimate and control the knee joint torque for flexion/extension movements with the best trade-off between accuracy and simplicity, we propose the following:

- Model the orthosis-wearer system as a single shank-foot segment moving through a single DoF at the knee joint level.
- Monitor the shank's 3D orientation based on the thigh 3D orientation measured in the global system of reference.
- Consider the first moment of inertia along the longitudinal axis of the shank-foot segment as well as the inertia moment about the knee AoR for knee joint torque estimation.

Chapter 6

General Conclusion

Quantifying and monitoring human motion is of crucial importance in numerous applications such as functional rehabilitation, orthopaedics, sports, assistive robotics or industrial ergonomics. For a rehabilitation process, in particular, measurements ensuring the correct execution of a prescribed exercise and quantifying the progress toward the patient recovery would be a great benefit for developing new tailored patient-specific treatment. Human motion can be characterized thanks to kinematics and kinetics measurements that are usually used together with a biomechanical model of the human body. The reference equipment commonly used to collect these quantities consist of expensive and complex Stereophotogrammetric Systems (SSs) and laboratory-grade force-plates. These are hardly usable outside of the laboratory. For widespread of human motion analysis, wearable and/or portable sensors have recently been the target of substantial research efforts. Despite their increased accessibility, thanks to their mass-market production motivated by the entertainment industry, these sensors suffer from limited accuracy, reliability, and usability. For instance, IMUs and RGB/RGB-D cameras-based MCSs have been widely used in the last years for human kinematics estimation. However, IMUs drift or cameras occlusion reduce significantly the accuracy of the kinematics estimate built from these sensors outputs. As developed in chapter 2 of this thesis, that presented the state of the art in human motion analysis, recent works in vision- and/or IMUs-based MCSs have considered to improve the accuracy of such systems through model-based and/or multi-sensors fusion approaches. This was the starting point of this work. Moreover, the challenge of developing truly affordable, user-friendly, and accurate MCSs that can be used out-side of the laboratory is yet to be achieved.

In light of the above considerations, we proposed in chapter 3 a new affordable, portable, and simple-to-use Visual Inertial Measurement Units-based MCS, capable of providing human 3D joint kinematics estimates. The proposed system consists of a new design of low-cost,

portable, and light-weight VIMUs sensors, including visual AR markers, tracked using an affordable RGB camera(s) and off-the-shelf open-source libraries, as well as affordable IMUs incorporating 3D accelerometers and 3D gyroscopes sensors. They provide synchronous 3D pose, 3D linear acceleration, and 3D angular velocity measurements. Being low-cost, VIMUs raw data are very inaccurate. New methods to cope with these inaccuracies are proposed. First a practical and equipment-free calibration method,that have to be performed only once, is proposed. Second, since each VIMU is assumed rigidly attached to the body segment it is monitoring, a practical sensors-to-segments calibration method has been developed. This is done by simply pin-pointing subjects anatomical landmarks of interest using a custom calibration wand. Doing so, no specific calibration movements, that might be challenging for a patient to perform, are required.

Then, to estimate physically-consistent 3D joint kinematics based on VIMUs data a new Constrained Extended Kalman Filter (CEKF) was developed. It makes use of the inherent constraints of a mechanical model of the human body to filter out physiologically unfeasible solutions. The sensor fusion in the CEKF also reduces the effect of each sensor's inaccuracies, especially allowing to handle markers occlusions and IMUs drift.

In chapter 4, two prototypes of the proposed VIMUs-based system were presented. The two systems were validated in two different studies for upper/lower-limbs kinematics estimation during daily rehabilitation tasks of the Modified Frenchay Test (MFT) and treadmill gait. The CEKF included a new measurement model based on the upper/lower-limbs forward kinematics and its derivatives to estimate each body segment VIMU measured data. Moreover, the IMUs random bias, physiological, soft, and/or rigid constraints were incorporated into the estimation process to ensure feasible joint angles estimation while further reducing the effect of the IMUs drift. Overall the accuracy of joint angles estimates was below 4deg when compared to a gold standard SS. This was also the case when a reduced number of VIMUs sensors was used. These results are very promising and, as discussed in chapter 4, are better than the current state-of-the art [136, 124, 109, 210].

Based on the excellent kinematics estimates provided by the proposed system, chapter 5 investigated, first, a practical method for Body Segments Inertial Parameters (BSIPs) identification of a human-exoskeleton system. In other words, the estimated joint and base kinematics were used in a dynamic identification pipeline together with the Ground Reaction Forces and Moments (GRFM) collected with an affordable force-plate. Beside the use of affordable sensors, the novelty here lies with the so-called augmented regressor matrix. It allows identifying separately each segment BSIPs of both human and exoskeleton. The

proposed method was experimentally validated with a subject wearing a full lower-limbs exoskeleton and was able to accurately estimate GRFM during a cross validation trial. In a second study, a new dynamics assessment framework has been developed to identify the best trade-off between an accurate and minimal human-exoskeleton dynamic model for joint torque estimation. It quantifies the contribution of kinematics and of BSIPs to the joint torque estimate, as well as the human-robot joint axes misalignment during motion. With this analysis, we proposed a reduced model of an orthosis-wearer system during standardized sitting knee/flexion movements. It was shown that using only two BSIPs for this model, namely the first moment of inertia along the longitudinal shank-foot segment axis and the inertia moment about the knee joint axis, was sufficient to estimate 97.5% of the total knee joint torque. At contrary, it was crucial to monitor the thigh 3D orientation to correctly project the gravity on the shank. Also, despite inter- and intra- subjects variability, knee joint axes misalignment was shown increasing with the knee RoM, in compliance with the knee joint anatomy, and reached a maximal average value up to 12deg at large extension angles. This will have implications for the future development of the control law for the orthosis.

According to McGinley et al. [235], in most common clinical situations, a RMSD up to 2deg may be considered excellent, and between 2 and 5deg is acceptable. Given that statement and the presented results, it is clear that the proposed motion capture system is very promising for the assessment of human motion outside of the laboratory. Because it is truly affordable and portable, we believe that its use can spread trough the clinical community. However, before commercialisation, several points would have to be improved. First of all, the system's ability to estimate human motion will have to be validated with patients with neurological pathologies in a real clinical environment. In hospital or in-home, the time available for donning and doffing the sensors is very limited. Thus, wearability, i.e., the mechanical design and attachment system, of the proposed VIMUs sensors will have to be improved. For the same reason, it would be a great improvement if the segment-to-sensor calibration could be done as the subject is moving for few seconds. For this, a modification of the methods proposed in [140, 142, 130] using kinematics constraints between multi body segments along with an online optimization process could be used. We believe that it would be possible to select only the collected samples that are meaning-full to identify the local VIMU pose. To do so methods, inspired from robotics calibration field based on a criterion related to the excitability of these parameters such as the condition number [236] could be used. Moreover, the fixed trunk condition assumed in chapter 4 might not be valid with patients. Indeed, hemiparetic patients might attempt to compensate their reduced arm mobility with trunk's motions to achieve a specific task. An additional VIMU, mounted at the

chest level, could track the patient's trunk movement. Adding sensors is always possible but comes at the cost of reducing the ease-of-use. Fortunately, we have shown that the proposed method is able to estimate accurately joint kinematics even with a reduced set of VIMUs sensors. The kinematics indeterminations coming from a sparse set of data were tackled by implementing knowledge models, constraints, state vector evolution model, etc, of the biomechanics of the task directly into the CEKF. This has been done before using a sparse set of retro-reflective markers and a MKO approach [79] but not in real-time. To further reduce the number of sensors and to be in line with the so-called minimum-input-measurement model [237], aiming at alleviating the experimental apparatus while maximizing the output information, a new trend is to use non-linear biomechanical cost functions and constraints to cope with sensors limitations/lack of information. Usually this is formulated as an optimal control problem aiming at tracking the available sensors data while minimizing a given physiological cost function [30]. This is a new field of research and so far it has been used only with relatively simple planar model. However, it is very promising and fascinating as it proposes to measure motion but also analyze and understand the neuro-muscular behavior of human.

The real-time capabilities of the CEKF implementation allows us to imagine using the joint kinematics estimates with a visual biofeedback system that could guide the patient in performing the investigated task in the most *normal* way. The *normal* way could be motion re-scaled from non-pathological subjects or could be predicted using a biomechanical cost function.

Real-time human joint kinematics estimates together with the joint misalignment results presented in chapter 5 could also help for the control of exoskeleton/orthosis. Indeed, a clear trend depending on the joint amplitude was observed and thus it could be modelled to predict misalignment between the orthosis and the wearer in a future model-based controller. However, before developing a new controller one would like also to investigate the interaction wrenches by instrumenting the contact between the orthosis and the wearer. Of course, it would also be interesting to extend the proposed dynamics assessment framework of chapter 5 to the full lower-limbs exoskeleton in both active and passive modes.

Having a correct estimation of joint kinematics and kinetics quantities pave the way to quantitatively build clinical score for the Modified Frenchay Test and develop a method for interpreting its numerical outcomes. This needs to be done with real patients and clinicians by comparing their qualitative analysis with the the proposed method output.

Moreover, being affordable, light-weight and simple-to-use, the proposed system allows targeting numerous applications, including sport, industrial ergonomics or further rehabilitation exercises. For industrial ergonomics, the fact that a VIMU does not rely on magnetometer

would be a real advantage to quantify a worker's motion directly on the factory floor. For the same reasons, the proposed VIMUs could be positioned on the human body and on a robotic assistive device

Finally, further developments of the existing system using additional types of sensors, such as force sensors embedded in the shoe, infrared, or RGB-D sensors to improve the tracking accuracy, may be investigated.

Bibliography

[1] Department of Economic United Nations and Social Affairs. World population ageing 2019: Highlights. ST/ESA/SER. A/430, 2019.

[2] Mira Katan and Andreas Luft. Global burden of stroke. In Seminars in neurology, volume 38, pages 208–211. Georg Thieme Verlag, 2018.

[3] Shane Xie et al. Advanced robotics for medical rehabilitation. Springer tracts in advanced robotics, 108(1):357, 2016.

[4] Erienne V Olesh, Sergiy Yakovenko, and Valeriya Gritsenko. Automated assessment of upper extremity movement impairment due to stroke. PloS one, 9(8):e104487, 2014.

[5] Charence Wong, Zhi-Qiang Zhang, Benny Lo, and Guang-Zhong Yang. Wearable sensing for solid biomechanics: A review. IEEE Sensors Journal, 15(5):2747–2760, 2015.

[6] Franchino Porciuncula, Anna Virginia Roto, Deepak Kumar, Irene Davis, Serge Roy, Conor J Walsh, and Louis N Awad. Wearable movement sensors for rehabilitation: a focused review of technological and clinical advances. PM&R, 10(9):S220–S232, 2018.

[7] Gabriele Bleser, Bertram Taetz, Markus Miezal, Corinna A Christmann, Daniel Steffen, and Katja Regenspurger. Development of an inertial motion capture system for clinical application: Potentials and challenges from the technology and application perspectives. i-com, 16(2):113–129, 2017.

[8] Bojan Milosevic, Alberto Leardini, and Elisabetta Farella. Kinect and wearable inertial sensors for motor rehabilitation programs at home: state of the art and an experimental comparison. BioMedical Engineering OnLine, 19, 04 2020.

[9] Steffi L Colyer, Murray Evans, Darren P Cosker, and Aki IT Salo. A review of the evolution of vision-based motion analysis and the integration of advanced computer vision methods towards developing a markerless system. Sports medicine-open, 4(1):24, 2018.

[10] Weiguang Huo, Samer Mohammed, Yacine Amirat, and Kyoungchul Kong. Active impedance control of a lower limb exoskeleton to assist sit-to-stand movement. In 2016 IEEE International Conference on Robotics and Automation (ICRA), pages 3530–3536. Ieee, 2016.

[11] Paweł Maciejasz, Jörg Eschweiler, Kurt Gerlach-Hahn, Arne Jansen-Troy, and Steffen Leonhardt. A survey on robotic devices for upper limb rehabilitation. Journal of neuroengineering and rehabilitation, 11(1):3, 2014.

[12] Damiano Zanotto, Yasuhiro Akiyama, Paul Stegall, and Sunil K Agrawal. Knee joint misalignment in exoskeletons for the lower extremities: Effects on user's gait. IEEE Transactions on Robotics, 31(4):978–987, 2015.

[13] Matthias B Näf, Karen Junius, Marco Rossini, Carlos Rodriguez-Guerrero, Bram Vanderborght, and Dirk Lefeber. Misalignment compensation for full human-exoskeleton kinematic compatibility: State of the art and evaluation. Applied Mechanics Reviews, 70(5), 2018.

[14] Weiguang Huo, Samer Mohammed, and Yacine Amirat. Impedance reduction control of a knee joint human-exoskeleton system. IEEE Transactions on Control Systems Technology, 27(6):2541–2556, 2018.

[15] R. Mallat, V. Bonnet, M. A. Khalil, and S. Mohammed. Upper limbs kinematics estimation using affordable visual-inertial sensors. IEEE Transactions on Automation Science and Engineering, pages 1–11, 2020.

[16] Randa Mallat, Vincent Bonnet, Mohamad Khalil, and Samer Mohammed. Toward an Affordable Multi-Modal Motion Capture System Framework for Human Kinematics and Kinetics Assessment: Proceedings of the 4th International Symposium on Wearable Robotics, WeRob2018, October 16-20, 2018, Pisa, Italy, pages 65–69. 01 2019.

[17] Randa Mallat, Vincent Bonnet, Raphaël Dumas, Mohamed Adjel, Mohamad Ali Khalil, and Samer Mohammed. Sparse visual-inertial measurement units placement for gait kinematics assessment. IEEE Transactions on Neural Systems and Rehabilitation Engineering, 2020 (In revision).

[18] Randa Mallat, Vincent Bonnet, Weiguang Huo, Patrick Karasinski, Yacine Amirat, Mohamad Khalil, and Samer Mohammed. Human-exoskeleton system dynamics identification using affordable sensors. In 2018 IEEE International Conference on Robotics and Automation (ICRA), pages 6759–6765. IEEE, 2018.

[19] R Mallat, V Bonnet, G Venture, R Dumas, M Khalil, and S Mohammed. Dynamics assessment and minimal model of an orthosis-assisted knee motion. In 2020 8th IEEE RAS/EMBS International Conference for Biomedical Robotics and Biomechatronics (BioRob), pages 352–357. IEEE.

[20] Duane Knudson. Fundamentals of biomechanics. Springer Science & Business Media, 2007.

[21] Shyamal Patel, Hyung Park, Paolo Bonato, Leighton Chan, and Mary Rodgers. A review of wearable sensors and systems with application in rehabilitation. Journal of neuroengineering and rehabilitation, 9(1):1–17, 2012.

[22] Hyun Kim, Nhayoung Hong, Myungjoon Kim, Sang Yoon, Hyeong Yu, Hyoun-Joong Kong, Su-jin Kim, Young Jun Chai, Hyung Choi, June Choi, Kyu Eun Lee, Sungwan Kim, and Hee Kim. Application of a perception neuron® system in simulation-based surgical training. Journal of Clinical Medicine, 8:124, 01 2019.

[23] Tung-Wu Lu and Chu-Fen Chang. Biomechanics of human movement and its clinical applications. The Kaohsiung journal of medical sciences, 28:S13–S25, 2012.

[24] Hiroshige Tateuchi, Haruhiko Akiyama, Koji Goto, Kazutaka So, Yutaka Kuroda, and Noriaki Ichihashi. Gait kinematics of the hip, pelvis, and trunk associated with external hip adduction moment in patients with secondary hip osteoarthritis: toward determination of the key point in gait modification. BMC Musculoskeletal Disorders, 21(1):1–8, 2020.

[25] Kojiro Hyodo, Akihiro Kanamori, Hideki Kadone, Tatsuya Takahashi, Masaya Kajiwara, and Masashi Yamazaki. Gait analysis comparing kinematic, kinetic, and muscle activation data of modern and conventional total knee arthroplasty. Arthroplasty Today, 6(3):338–342, 2020.

[26] Marcela dos Santos Delabary, Elren Passos Monteiro, Rebeca Gimenes Donida, Mariana Wolffenbuttel, Leonardo Alexandre Peyré-Tartaruga, and Aline Nogueira Haas. Can samba and forró brazilian rhythmic dance be more effective than walking in improving functional mobility and spatiotemporal gait parameters in patients with parkinson's disease? BMC neurology, 20(1):1–10, 2020.

[27] Shanshan Chen, John Lach, Benny Lo, and Guang-Zhong Yang. Toward pervasive gait analysis with wearable sensors: A systematic review. IEEE journal of biomedical and health informatics, 20(6):1521–1537, 2016.

[28] Aaron M Dollar and Hugh Herr. Lower extremity exoskeletons and active orthoses: Challenges and state-of-the-art. IEEE Transactions on robotics, 24(1):144–158, 2008.

[29] Amin Ahmadi, François Destelle, Luis Unzueta, David S Monaghan, Maria Teresa Linaza, Kieran Moran, and Noel E O'Connor. 3d human gait reconstruction and monitoring using body-worn inertial sensors and kinematic modeling. IEEE Sensors Journal, 16(24):8823–8831, 2016.

[30] Eva Dorschky, Marlies Nitschke, Ann-Kristin Seifer, Antonie J van den Bogert, and Bjoern M Eskofier. Estimation of gait kinematics and kinetics from inertial sensor data using optimal control of musculoskeletal models. Journal of biomechanics, 95:109278, 2019.

[31] Thiago Braga Rodrigues, Debora Pereira Salgado, Ciarán Ó Catháin, Noel O'Connor, and Niall Murray. Human gait assessment using a 3d marker-less multimodal motion capture system. Multimedia Tools and Applications, 79(3):2629–2651, 2020.

[32] Felix Kluge, Heiko Gaßner, Julius Hannink, Cristian Pasluosta, Jochen Klucken, and Björn M Eskofier. Towards mobile gait analysis: concurrent validity and test-retest reliability of an inertial measurement system for the assessment of spatio-temporal gait parameters. Sensors, 17(7):1522, 2017.

[33] Karina Berner, John Cockcroft, and Quinette Louw. Kinematics and temporospatial parameters during gait from inertial motion capture in adults with and without hiv: a validity and reliability study. BioMedical Engineering OnLine, 19(1):1–25, 2020.

[34] Guoliang Luo, Yean Zhu, Rui Wang, Yang Tong, Wei Lu, and Haolun Wang. Random forest–based classsification and analysis of hemiplegia gait using low-cost depth cameras. Medical & Biological Engineering & Computing, 58(2):373–382, 2020.

[35] Vrutangkumar V Shah, James McNames, Martina Mancini, Patricia Carlson-Kuhta, Rebecca I Spain, John G Nutt, Mahmoud El-Gohary, Carolin Curtze, and Fay B Horak. Quantity and quality of gait and turning in people with multiple sclerosis, parkinson's disease and matched controls during daily living. Journal of Neurology, pages 1–9, 2020.

[36] Basilio Pueo, Jose Manuel Jimenez-Olmedo, et al. Application of motion capture technology for sport performance analysis. 2017.

[37] Xiaoming Liu, Zhongyuan Chen, Wanchun Chen, and Xiaolan Xing. Motion estimation using optical flow sensors and rate gyros. In 2016 IEEE International Conference on Mechatronics and Automation, pages 1708–1715. IEEE, 2016.

[38] Jin Ho Park, Gyulee Park, Ha Yeon Kim, Ji-Yeong Lee, Yeajin Ham, Donghwan Hwang, Suncheol Kwon, and Joon-Ho Shin. A comparison of the effects and usability of two exoskeletal robots with and without robotic actuation for upper extremity rehabilitation among patients with stroke: a single-blinded randomised controlled pilot study. Journal of neuroengineering and rehabilitation, 17(1):1–12, 2020.

[39] Gabriele Rescio, Alessandro Leone, and Pietro Siciliano. Supervised expert system for wearable mems accelerometer-based fall detector. Journal of Sensors, 2013, 2013.

[40] Paola Pierleoni, Alberto Belli, Lorenzo Palma, Marco Pellegrini, Luca Pernini, and Simone Valenti. A high reliability wearable device for elderly fall detection. IEEE Sensors Journal, 15(8):4544–4553, 2015.

[41] Roberto Ugolotti, Federico Sassi, Monica Mordonini, and Stefano Cagnoni. Multi-sensor system for detection and classification of human activities. Journal of Ambient Intelligence and Humanized Computing, 4(1):27–41, 2013.

[42] Jessica Colombel, Vincent Bonnet, David Daney, Raphael Dumas, Antoine Seilles, and François Charpillet. Physically consistent whole-body kinematics assessment based on an rgb-d sensor. application to simple rehabilitation exercises. Sensors, 20(10):2848, 2020.

[43] Ive Weygers, Manon Kok, Marco Konings, Hans Hallez, Henri De Vroey, and Kurt Claeys. Inertial sensor-based lower limb joint kinematics: A methodological systematic review. Sensors, 20(3):673, 2020.

[44] Mohammed H Iqbal, Abdullatif Aydin, Oliver Brunckhorst, Prokar Dasgupta, and Kamran Ahmed. A review of wearable technology in medicine. Journal of the Royal Society of Medicine, 109(10):372–380, 2016.

[45] Ryan P Hubble, Geraldine A Naughton, Peter A Silburn, and Michael H Cole. Wearable sensor use for assessing standing balance and walking stability in people with parkinson's disease: a systematic review. PloS one, 10(4):e0123705, 2015.

[46] Daniela TarniŢă. Wearable sensors used for human gait analysis. Rom J Morphol Embryol, 57(2):373–382, 2016.

[47] M Barandas, H Gamboa, and JM Fonseca. A real time biofeedback system using visual user interface for physical rehabilitation. Procedia Manufacturing, 3:823–828, 2015.

[48] Weiguang Huo, Samer Mohammed, Yacine Amirat, and Kyoungchul Kong. Fast gait mode detection and assistive torque control of an exoskeletal robotic orthosis for walking assistance. IEEE Transactions on Robotics, 34(4):1035–1052, 2018.

[49] Li Li, Ziyang Xie, and Xu Xu. Moped25: A multimodal dataset of full-body pose and motion in occupational tasks. Journal of Biomechanics, 113:110086, 2020.

[50] Li Li, Tara Martin, and Xu Xu. A novel vision-based real-time method for evaluating postural risk factors associated with musculoskeletal disorders. Applied Ergonomics, 87:103138, 2020.

[51] Maury A Nussbaum, Brian D Lowe, Michiel de Looze, Carisa Harris-Adamson, and Marty Smets. An introduction to the special issue on occupational exoskeletons, 2019.

[52] Marty Smets. A field evaluation of arm-support exoskeletons for overhead work applications in automotive assembly. IISE Transactions on Occupational Ergonomics and Human Factors, 7(3-4):192–198, 2019.

[53] Boyi Dai, William E Garrett, Michael T Gross, Darin A Padua, Robin M Queen, and Bing Yu. The effects of 2 landing techniques on knee kinematics, kinetics, and performance during stop-jump and side-cutting tasks. The American journal of sports medicine, 43(2):466–474, 2015.

[54] Jonathan Sinclair and Lindsay Bottoms. Gender differences in the kinetics and lower extremity kinematics of the fencing lunge. International Journal of Performance Analysis in Sport, 13(2):440–451, 2013.

[55] Caroline Martin, Richard Kulpa, Paul Delamarche, and Benoit Bideau. Professional tennis players' serve: correlation between segmental angular momentums and ball velocity. Sports Biomechanics, 12(1):2–14, 2013.

[56] Caroline Martin, Benoit Bideau, Nicolas Bideau, Guillaume Nicolas, Paul Delamarche, and Richard Kulpa. Energy flow analysis during the tennis serve: comparison between injured and noninjured tennis players. The American journal of sports medicine, 42(11):2751–2760, 2014.

[57] Caroline Martin, Benoit Bideau, Paul Delamarche, and Richard Kulpa. Influence of a prolonged tennis match play on serve biomechanics. PLoS One, 11(8):e0159979, 2016.

[58] Machar Reid, Georgia Giblin, and David Whiteside. A kinematic comparison of the overhand throw and tennis serve in tennis players: How similar are they really? Journal of Sports Sciences, 33(7):713–723, 2015.

[59] Eline van der Kruk and Marco M Reijne. Accuracy of human motion capture systems for sport applications; state-of-the-art review. European journal of sport science, 18(6):806–819, 2018.

[60] Herbert Hatze. The meaning of the term" biomechanics". Journal of biomechanics, 7(2):189, 1974.

[61] Susan Hall. Basic biomechanics. McGraw-Hill Higher Education, 2014.

[62] Sebastian Wolf. Handbook of human motion. Springer, 2018.

[63] Vladimir M Zatsiorsky and Boris I Prilutsky. Biomechanics of skeletal muscles. Human Kinetics, 2012.

[64] Ge Wu, Sorin Siegler, Paul Allard, Chris Kirtley, Alberto Leardini, Dieter Rosenbaum, Mike Whittle, Darryl D D'Lima, Luca Cristofolini, Hartmut Witte, et al. Isb recommendation on definitions of joint coordinate system of various joints for the reporting of human joint motion—part i: ankle, hip, and spine. Journal of biomechanics, 35(4):543–548, 2002.

[65] T-W Lu and JJ O'connor. Bone position estimation from skin marker co-ordinates using global optimisation with joint constraints. Journal of biomechanics, 32(2):129–134, 1999.

[66] Wisama Khalil and Etienne Dombre. Modeling, identification and control of robots. Butterworth-Heinemann, 2004.

[67] Wisama Khalil and Denis Creusot. Symoro+: a system for the symbolic modelling of robots. 1997.

[68] Maxime Gautier. Numerical calculation of the base inertial parameters of robots. Journal of robotic systems, 8(4):485–506, 1991.

[69] Gergely Nagymáté and Rita M Kiss. Affordable gait analysis using augmented reality markers. PloS one, 14(2):e0212319, 2019.

[70] Gabriele Bleser, Gustaf Hendeby, and Markus Miezal. Using egocentric vision to achieve robust inertial body tracking under magnetic disturbances. In 2011 10th IEEE International Symposium on Mixed and Augmented Reality, pages 103–109. IEEE, 2011.

[71] Alexander M Aurand, Jonathan S Dufour, and William S Marras. Accuracy map of an optical motion capture system with 42 or 21 cameras in a large measurement volume. Journal of biomechanics, 58:237–240, 2017.

[72] Magnus Burenius, Josephine Sullivan, and Stefan Carlsson. Motion capture from dynamic orthographic cameras. In 2011 IEEE International Conference on Computer Vision Workshops (ICCV Workshops), pages 1634–1641. IEEE, 2011.

[73] Rita Stagni, Silvia Fantozzi, Angelo Cappello, and Alberto Leardini. Quantification of soft tissue artefact in motion analysis by combining 3d fluoroscopy and stereophotogrammetry: a study on two subjects. Clinical Biomechanics, 20(3):320–329, 2005.

[74] Elena Ceseracciu, Zimi Sawacha, and Claudio Cobelli. Comparison of markerless and marker-based motion capture technologies through simultaneous data collection during gait: proof of concept. PloS one, 9(3):e87640, 2014.

[75] Young-Shin Cho, Seong-Ho Jang, Jae-Sung Cho, Mi-Jung Kim, Hyeok Dong Lee, Sung Young Lee, and Sang-Bok Moon. Evaluation of validity and reliability of inertial measurement unit-based gait analysis systems. Annals of rehabilitation medicine, 42(6):872, 2018.

[76] Paul Allard, Aurelio Cappozzo, Arne Lundberg, and Christopher Vaughan. Three-dimensional analysis of human locomotion. John Wiley & Sons, Inc., 1998.

[77] Gutemberg Guerra-Filho. Optical motion capture: Theory and implementation. RITA, 12(2):61–90, 2005.

[78] Lynsey D Duffell, Natalie Hope, and Alison H McGregor. Comparison of kinematic and kinetic parameters calculated using a cluster-based model and vicon's plug-in gait. Proceedings of the Institution of Mechanical Engineers, Part H: Journal of Engineering in Medicine, 228(2):206–210, 2014.

[79] Mickaël Begon, Michael Skipper Andersen, and Raphaël Dumas. Multibody kinematics optimization for the estimation of upper and lower limb human joint kinematics: a systematized methodological review. Journal of biomechanical engineering, 140(3), 2018.

[80] Valentina Camomilla, Aurelio Cappozzo, and Giuseppe Vannozzi. Three-dimensional reconstruction of the human skeleton in motion. Handbook of human motion. Cham: Springer International Publishing, pages 17–45, 2018.

[81] A buyer's guide to 3-d motion capture systems for sport. https://simplifaster.com/articles/3d-motion-capture-sport/.

[82] Gergely Nagymáté and Rita M Kiss. Application of optitrack motion capture systems in human movement analysis. Recent Innovations in Mechatronics, 5(1.):1–9, 2018.

[83] Optitrack - General FAQs. https://optitrack.com/support/faq/general.html.

[84] Patric Eichelberger, Matteo Ferraro, Ursina Minder, Trevor Denton, Angela Blasimann, Fabian Krause, and Heiner Baur. Analysis of accuracy in optical motion capture–a protocol for laboratory setup evaluation. Journal of biomechanics, 49(10):2085–2088, 2016.

[85] Pierre Merriaux, Yohan Dupuis, Rémi Boutteau, Pascal Vasseur, and Xavier Savatier. A study of vicon system positioning performance. Sensors, 17(7):1591, 2017.

[86] Paul Lückemann, Steph Forrester, Aimée Mears, Jonathan Shepherd, and Jon Roberts. Assessment of measurement uncertainty in optical marker tracking of high-speed motion. In Multidisciplinary Digital Publishing Institute Proceedings, volume 49, page 72, 2020.

[87] Valentina Camomilla, Raphaël Dumas, and Aurelio Cappozzo. Human movement analysis: The soft tissue artefact issue. 2017.

[88] Alberto Leardini, Lorenzo Chiari, Ugo Della Croce, and Aurelio Cappozzo. Human movement analysis using stereophotogrammetry: Part 3. soft tissue artifact assessment and compensation. Gait & posture, 21(2):212–225, 2005.

[89] Ugo Della Croce, Alberto Leardini, Lorenzo Chiari, and Aurelio Cappozzo. Human movement analysis using stereophotogrammetry: Part 4: assessment of anatomical landmark misplacement and its effects on joint kinematics. Gait & posture, 21(2):226–237, 2005.

[90] Lorenzo Chiari, Ugo Della Croce, Alberto Leardini, and Aurelio Cappozzo. Human movement analysis using stereophotogrammetry: Part 2: Instrumental errors. Gait & posture, 21(2):197–211, 2005.

[91] TP Andriacchi, EJ Alexander, MK Toney, C Dyrby, and J Sum. A point cluster method for in vivo motion analysis: applied to a study of knee kinematics. 1998.

[92] Angelo Cappello, Aurelio Cappozzo, Pier Francesco La Palombara, Luigi Lucchetti, and Alberto Leardini. Multiple anatomical landmark calibration for optimal bone pose estimation. Human movement science, 16(2-3):259–274, 1997.

[93] Automated motion analysis for 3d and 6d data requiring any single camera. https://photron.com/6d-marker/.

[94] Francisco J Romero-Ramirez, Rafael Muñoz-Salinas, and Rafael Medina-Carnicer. Speeded up detection of squared fiducial markers. Image and vision Computing, 76:38–47, 2018.

[95] Itseez. The OpenCV Reference Manual, 2.4.9.0 edition, April 2014.

[96] Jorge J Moré. The levenberg-marquardt algorithm: implementation and theory. In Numerical analysis, pages 105–116. Springer, 1978.

[97] Michail Kalaitzakis, Sabrina Carroll, Anand Ambrosi, Camden Whitehead, and Nikolaos Vitzilaios. Experimental comparison of fiducial markers for pose estimation. In 2020 International Conference on Unmanned Aircraft Systems (ICUAS), pages 781–789. IEEE, 2020.

[98] Raju Gupta. Fiducial marker-based motion capture system for biomechanics and lower limb prosthesis alignment. 2019.

[99] Raphaël Zazackowski. Etude exploratoire du suivi in vivo de la cinématique osseuse. 2017.

[100] Daniel Wagner and Dieter Schmalstieg. Artoolkitplus for pose tracking on mobile devices. 01 2007.

[101] Guoping He, Shangkun Zhong, and Jifeng Guo. A lightweight and scalable visual-inertial motion capture system using fiducial markers. Autonomous Robots, 43(7):1895–1915, 2019.

[102] BR Mantha and B Garcia de Soto. Designing a reliable fiducial marker network for autonomous indoor robot navigation. In Proceedings of the 36th International Symposium on Automation and Robotics in Construction (ISARC), pages 21–24, 2019.

[103] Vincent Bonnet, Nahéma Sylla, Andrea Cherubini, A Gonzáles, C Azevedo Coste, Philippe Fraisse, and Gentiane Venture. Toward an affordable and user-friendly visual motion capture system. In 2014 36th Annual International Conference of the IEEE Engineering in Medicine and Biology Society, pages 3634–3637. IEEE, 2014.

[104] LG Wiedemann, R Planinc, I Nemec, and M Kampel. Performance evaluation of joint angles obtained by the kinect v2. 2015.

[105] Zhe Cao, Gines Hidalgo, Tomas Simon, Shih-En Wei, and Yaser Sheikh. Openpose: Realtime multi-person 2d pose estimation using part affinity fields, 12 2018.

[106] Timo Marcard, Roberto Henschel, Michael Black, Bodo Rosenhahn, and Gerard Pons-Moll. Recovering Accurate 3D Human Pose in the Wild Using IMUs and a Moving Camera: 15th European Conference, Munich, Germany, September 8-14, 2018, Proceedings, Part X, pages 614–631. 09 2018.

[107] MJ Mathie, Branko G Celler, Nigel H Lovell, and ACF Coster. Classification of basic daily movements using a triaxial accelerometer. Medical and Biological Engineering and Computing, 42(5):679–687, 2004.

[108] Frieder Wittmann, Olivier Lambercy, and Roger Gassert. Magnetometer-based drift correction during rest in imu arm motion tracking. Sensors, 19(6):1312, 2019.

[109] Mahmoud El-Gohary and James McNames. Human joint angle estimation with inertial sensors and validation with a robot arm. IEEE Transactions on Biomedical Engineering, 62(7):1759–1767, 2015.

[110] Daniel Roetenberg. Inertial and magnetic sensing of human motion. These de doctorat, 2006.

[111] Eric Foxlin. Pedestrian tracking with shoe-mounted inertial sensors. IEEE Computer graphics and applications, 25(6):38–46, 2005.

[112] Julia M Leach, Martina Mancini, Robert J Peterka, Tamara L Hayes, and Fay B Horak. Validating and calibrating the nintendo wii balance board to derive reliable center of pressure measures. Sensors, 14(10):18244–18267, 2014.

[113] Gentiane Venture, Ko Ayusawa, and Yoshihiko Nakamura. Identification of human mass properties from motion. IFAC Proceedings Volumes, 42(10):988–993, 2009.

[114] James C Walsh, John F Quinlan, Robert Stapleton, David P FitzPatrick, and Damian McCormack. Three-dimensional motion analysis of the lumbar spine during "free squat" weight lift training. The American journal of sports medicine, 35(6):927–932, 2007.

[115] Ole Bischoff, Nils Heidmann, Jochen Rust, and Steffen Paul. Design and implementation of an ultrasonic localization system for wireless sensor networks using angle-of-arrival and distance measurement. Procedia Engineering, 47:953–956, 2012.

[116] Takeshi Miura, Takaaki Kaiga, Katsubumi Tajima, Takeshi Shibata, and Hideo Tamamoto. Sensor number reduction in skeleton estimation from magnetic motion capture data. Journal of Information Processing, 23(5):704–707, 2015.

[117] Eric Foxlin, Michael Harrington, and George Pfeifer. Constellation: a wide-range wireless motion-tracking system for augmented reality and virtual set applications. In Proceedings of the 25th annual conference on Computer graphics and interactive techniques, pages 371–378, 1998.

[118] Jamie A Ward, Paul Lukowicz, and Gerhard Tröster. Gesture spotting using wrist worn microphone and 3-axis accelerometer. In Proceedings of the 2005 joint conference on Smart objects and ambient intelligence: innovative context-aware services: usages and technologies, pages 99–104, 2005.

[119] Cédric Joguet, D David, and Y Caritu. Pen-like, natural graphic gesture capture disposal, based on a microsystem. In Proc. of Smart Objects Conference SOC'03, Grenoble, France, 2003.

[120] Isaac Skog and Peter Händel. A low-cost gps aided inertial navigation system for vehicle applications. In 2005 13th European Signal Processing Conference, pages 1–4. IEEE, 2005.

[121] Juan Li, Juan A Besada, Ana M Bernardos, Paula Tarrío, and José R Casar. A novel system for object pose estimation using fused vision and inertial data. Information Fusion, 33:15–28, 2017.

[122] Mary B Alatise and Gerhard P Hancke. Pose estimation of a mobile robot based on fusion of imu data and vision data using an extended kalman filter. Sensors, 17(10):2164, 2017.

[123] Haoyang Ye and Ming Liu. Lidar and inertial fusion for pose estimation by non-linear optimization. arXiv preprint arXiv:1710.07104, 2017.

[124] Grzegorz Glonek and Adam Wojciechowski. Hybrid orientation based human limbs motion tracking method. Sensors, 17(12):2857, 2017.

[125] Yushuang Tian, Xiaoli Meng, Dapeng Tao, Dongquan Liu, and Chen Feng. Upper limb motion tracking with the integration of imu and kinect. Neurocomputing, 159:207–218, 2015.

[126] Yinlong Zhang, Wei Liang, Hongsheng He, and Jindong Tan. Wearable heading estimation for motion tracking in health care by adaptive fusion of visual–inertial measurements. IEEE journal of biomedical and health informatics, 22(6):1732–1743, 2018.

[127] Ahmed Ahmed and Stergios Roumeliotis. A visual-inertial approach to human gait estimation. In 2018 IEEE International Conference on Robotics and Automation (ICRA), pages 1–8. IEEE, 2018.

[128] Kun Liu, Tao Liu, Kyoko Shibata, and Yoshio Inoue. Ambulatory measurement and analysis of the lower limb 3d posture using wearable sensor system. In 2009 International Conference on Mechatronics and Automation, pages 3065–3069. IEEE, 2009.

[129] J Favre, F Luthi, BM Jolles, O Siegrist, B Najafi, and K Aminian. A new ambulatory system for comparative evaluation of the three-dimensional knee kinematics, applied to anterior cruciate ligament injuries. Knee Surgery, Sports Traumatology, Arthroscopy, 14(7):592–604, 2006.

[130] Yawen Chen, Chenglong Fu, Winnie Suk Wai Leung, and Ling Shi. Drift-free and self-aligned imu-based human gait tracking system with augmented precision and robustness. IEEE Robotics and Automation Letters, 5(3):4671–4678, 2020.

[131] A Brennan, J Zhang, K Deluzio, and Q Li. Quantification of inertial sensor-based 3d joint angle measurement accuracy using an instrumented gimbal. Gait & posture, 34(3):320–323, 2011.

[132] Brice Bouvier, Sonia Duprey, Laurent Claudon, Raphaël Dumas, and Adriana Savescu. Upper limb kinematics using inertial and magnetic sensors: Comparison of sensor-to-segment calibrations. Sensors, 15(8):18813–18833, 2015.

[133] Julien Favre, Rachid Aissaoui, Brigitte M Jolles, Jacques A de Guise, and Kamiar Aminian. Functional calibration procedure for 3d knee joint angle description using inertial sensors. Journal of biomechanics, 42(14):2330–2335, 2009.

[134] Anthony G Schache, Richard Baker, and Larry W Lamoreux. Defining the knee joint flexion–extension axis for purposes of quantitative gait analysis: an evaluation of methods. Gait & posture, 24(1):100–109, 2006.

[135] Daniel Roetenberg, Henk Luinge, and Per Slycke. Xsens mvn: Full 6dof human motion tracking using miniature inertial sensors. Xsens Motion Technologies BV, Tech. Rep, 1, 2009.

[136] Luke Wicent Sy, Michael Raitor, Michael Del Rosario, Heba Khamis, Lauren Kark, Nigel Hamilton Lovell, and Stephen Redmond. Estimating lower limb kinematics using a reduced wearable sensor count. IEEE Transactions on Biomedical Engineering, 2020.

[137] Laura Susana Vargas-Valencia, Arlindo Elias, Eduardo Rocon, Teodiano Bastos-Filho, and Anselmo Frizera. An imu-to-body alignment method applied to human gait analysis. Sensors, 16(12):2090, 2016.

[138] Luca Ricci, Domenico Formica, Laura Sparaci, Francesca Romana Lasorsa, Fabrizio Taffoni, Eleonora Tamilia, and Eugenio Guglielmelli. A new calibration methodology for thorax and upper limbs motion capture in children using magneto and inertial sensors. Sensors, 14(1):1057–1072, 2014.

[139] Thomas Seel, Thomas Schauer, and Jörg Raisch. Joint axis and position estimation from inertial measurement data by exploiting kinematic constraints. In 2012 IEEE International Conference on Control Applications, pages 45–49. IEEE, 2012.

[140] Thomas Seel, Jörg Raisch, and Thomas Schauer. Imu-based joint angle measurement for gait analysis. Sensors, 14(4):6891–6909, 2014.

[141] Philipp Müller, Marc-André Bégin, Thomas Schauer, and Thomas Seel. Alignment-free, self-calibrating elbow angles measurement using inertial sensors. IEEE journal of biomedical and health informatics, 21(2):312–319, 2016.

[142] Chunzhi Yi, Feng Jiang, Zhiyuan Chen, Baichun Wei, Hao Guo, Xunfeng Yin, Fangzhuo Li, and Chifu Yang. Sensor-movement-robust angle estimation for 3-dof lower limb joints without calibration. arXiv preprint arXiv:1910.07240, 2019.

[143] Sarvenaz Salehi, Gabriele Bleser, Attila Reiss, and Didier Stricker. Body-imu autocalibration for inertial hip and knee joint tracking. In Proceedings of the 10th EAI International Conference on Body Area Networks, pages 51–57, 2015.

[144] Henk J Luinge, Peter H Veltink, and Chris TM Baten. Ambulatory measurement of arm orientation. Journal of biomechanics, 40(1):78–85, 2007.

[145] Angelo M Sabatini. Quaternion-based extended kalman filter for determining orientation by inertial and magnetic sensing. IEEE transactions on Biomedical Engineering, 53(7):1346–1356, 2006.

[146] Christoph Schiefer, Rolf P Ellegast, Ingo Hermanns, Thomas Kraus, Elke Ochsmann, Christian Larue, and André Plamondon. Optimization of inertial sensor-based motion capturing for magnetically distorted field applications. Journal of biomechanical engineering, 136(12), 2014.

[147] Claudia Mazza, Marco Donati, John McCamley, Pietro Picerno, and Aurelio Cappozzo. An optimized kalman filter for the estimate of trunk orientation from inertial sensors data during treadmill walking. Gait & posture, 35(1):138–142, 2012.

[148] Daniel Roetenberg, Henk J Luinge, Chris TM Baten, and Peter H Veltink. Compensation of magnetic disturbances improves inertial and magnetic sensing of human body segment orientation. IEEE Transactions on neural systems and rehabilitation engineering, 13(3):395–405, 2005.

[149] Eric R Bachmann, Robert B McGhee, Xiaoping Yun, and Michael J Zyda. Inertial and magnetic posture tracking for inserting humans into networked virtual environments. In Proceedings of the ACM symposium on Virtual reality software and technology, pages 9–16, 2001.

[150] Jonathan FS Lin and Dana Kulić. Human pose recovery using wireless inertial measurement units. Physiological measurement, 33(12):2099, 2012.

[151] Yang Zheng, Ka-Chun Chan, and Charlie CL Wang. Pedalvatar: An imu-based real-time body motion capture system using foot rooted kinematic model. In 2014 IEEE/RSJ International Conference on Intelligent Robots and Systems, pages 4130–4135. IEEE, 2014.

[152] Diego Álvarez, Juan C Alvarez, Rafael C González, and Antonio M López. Upper limb joint angle measurement in occupational health. Computer Methods in Biomechanics and Biomedical Engineering, 19(2):159–170, 2016.

[153] Joseph J LaViola. A comparison of unscented and extended kalman filtering for estimating quaternion motion. In Proceedings of the 2003 American Control Conference, 2003., volume 3, pages 2435–2440. IEEE, 2003.

[154] Vladimir Joukov, Vincent Bonnet, Michelle Karg, Gentiane Venture, and Dana Kulić. Rhythmic extended kalman filter for gait rehabilitation motion estimation and segmentation. IEEE Transactions on Neural Systems and Rehabilitation Engineering, 26(2):407–418, 2017.

[155] Jovana Jovic, Adrien Escande, Ko Ayusawa, Eiichi Yoshida, Abderrahmane Kheddar, and Gentiane Venture. Humanoid and human inertia parameter identification using hierarchical optimization. IEEE Transactions on Robotics, 32(3):726–735, 2016.

[156] Nora Millor, Pablo Lecumberri, Marisol Gómez, Alicia Martínez-Ramírez, and Mikel Izquierdo. Drift-free position estimation for periodic movements using inertial units. IEEE Journal of Biomedical and Health Informatics, 18(4):1131–1137, 2013.

[157] Vincent Bonnet, Claudia Mazza, John McCamley, and Aurelio Cappozzo. Use of weighted fourier linear combiner filters to estimate lower trunk 3d orientation from gyroscope sensors data. Journal of neuroengineering and rehabilitation, 10(1):29, 2013.

[158] Dorothea J Tsang, Meghan Lukac, and Anne E Martin. Characterization of statistical persistence in joint angle variation during walking. Human movement science, 68:102528, 2019.

[159] Vincent Bonnet, Vladimir Joukov, Dana Kulić, Philippe Fraisse, Nacim Ramdani, and Gentiane Venture. Monitoring of hip and knee joint angles using a single inertial measurement unit during lower limb rehabilitation. IEEE Sensors Journal, 16(6):1557–1564, 2015.

[160] Jakob Ziegler, Alexander Reiter, Hubert Gattringer, and Andreas Müller. Simultaneous identification of human body model parameters and gait trajectory from 3d motion capture data. Medical Engineering & Physics, 84:193–202, 2020.

[161] Vincent Bonnet, Claudia Mazza, Philippe Fraisse, and Aurelio Cappozzo. Real-time estimate of body kinematics during a planar squat task using a single inertial measurement unit. IEEE Transactions on Biomedical Engineering, 60(7):1920–1926, 2013.

[162] Arturo Bertomeu-Motos, Luis D Lledó, Jorge A Díez, Jose M Catalan, Santiago Ezquerro, Francisco J Badesa, and Nicolas Garcia-Aracil. Estimation of human arm joints using two wireless sensors in robotic rehabilitation tasks. Sensors, 15(12):30571–30583, 2015.

[163] Arturo Bertomeu-Motos, Andrea Blanco, Francisco J Badesa, Juan A Barios, Loredana Zollo, and Nicolas Garcia-Aracil. Human arm joints reconstruction algorithm in rehabilitation therapies assisted by end-effector robotic devices. Journal of neuroengineering and rehabilitation, 15(1):10, 2018.

[164] Eva Repnik, Urška Puh, Nika Goljar, Marko Munih, and Matjaž Mihelj. Using inertial measurement units and electromyography to quantify movement during action research arm test execution. Sensors, 18(9):2767, 2018.

[165] Matjaž Mihelj, Janez Podobnik, and Marko Munih. Sensory fusion of magnetoinertial data based on kinematic model with jacobian weighted-left-pseudoinverse and kalman-adaptive gains. IEEE Transactions on Instrumentation and Measurement, 68(7):2610–2620, 2018.

[166] Mickael Begon and Patrick Lacouture. Anthropometric modeling for a sport mechanical analysis part i: Models, their parameters and their validation. Science et Motricite, 54:11–33, 01 2005.

[167] Raphaël Dumas, Laurence Cheze, and J-P Verriest. Adjustments to mcconville et al. and young et al. body segment inertial parameters. Journal of biomechanics, 40(3):543–553, 2007.

[168] W. Dempster. Space requirements of the seated operator: geometrical, kinematic, and mechanical aspects of the body, with special reference to the limbs. Wright Air Development Center Technical Report, 55–159, 01 1956.

[169] John McConville, Charles Clauser, Thomas Churchill, Jaime Cuzzi, and Ints Kaleps. Anthropometric relationships of body and body segment moments of inertia. OH: Wright-Patterson Air Force Base, page 113, 12 1980.

[170] Paolo Leva. Adjustments to zatsiorsky-seluyanov's segment inertia parameters. Journal of biomechanics, 29:1223–30, 10 1996.

[171] Gentiane Venture, Ko Ayusawa, and Yoshihiko Nakamura. Motion capture based identification of the human body inertial parameters. In 2008 30th Annual International Conference of the IEEE Engineering in Medicine and Biology Society, pages 4575–4578. IEEE, 2008.

[172] Paolo Leva. Validity and accuracy of four methods for locating the center of mass of young male and female athletes. Journal of Biomechanics, 27:763, 12 1994.

[173] Xabier Iriarte, Miguel Díaz-Rodríguez, and Vicente Mata. A multicriteria approach for optimal trajectories in dynamic parameter identification of parallel robots. In Proceedings of EUCOMES 08, pages 279–285. Springer, 2009.

[174] Johannes Mayr and Hubert Gattringer. Static inertial parameter identification for humanoid robots using a torque-free support. In 2014 IEEE-RAS International Conference on Humanoid Robots, pages 99–104. IEEE, 2014.

[175] Vincent Bonnet, Philippe Fraisse, André Crosnier, Maxime Gautier, Alejandro González, and Gentiane Venture. Optimal exciting dance for identifying inertial parameters of an anthropomorphic structure. IEEE Transactions on Robotics, 32(4):823–836, 2016.

[176] Maxime Gautier and Wisama Khalil. Direct calculation of minimum set of inertial parameters of serial robots. IEEE Transactions on robotics and Automation, 6(3):368–373, 1990.

[177] Maxime Gautier and Wisama Khalil. Exciting trajectories for the identification of base inertial parameters of robots. The International journal of robotics research, 11(4):362–375, 1992.

[178] Maxime Gautier and Gentiane Venture. Identification of standard dynamic parameters of robots with positive definite inertia matrix. In 2013 IEEE/RSJ International Conference on Intelligent Robots and Systems, pages 5815–5820. IEEE, 2013.

[179] Simon Alexanderson. Performance, Processing and Perception of Communicative Motion for Avatars and Agents. PhD thesis, KTH Royal Institute of Technology, 2017.

[180] Diego Felipe Paez Granados, Breno A Yamamoto, Hiroko Kamide, Jun Kinugawa, and Kazuhiro Kosuge. Dance teaching by a robot: Combining cognitive and physical human–robot interaction for supporting the skill learning process. IEEE Robotics and Automation Letters, 2(3):1452–1459, 2017.

[181] Francesco Rea, Alessia Vignolo, Alessandra Sciutti, and Nicoletta Noceti. Human motion understanding for selecting action timing in collaborative human-robot interaction. Front. Robot. AI, 6:58, 2019.

[182] Adam B Zoss, Hami Kazerooni, and Andrew Chu. Biomechanical design of the berkeley lower extremity exoskeleton (bleex). IEEE/ASME Transactions on mechatronics, 11(2):128–138, 2006.

[183] Marco Cempini, Stefano Marco Maria De Rossi, Tommaso Lenzi, Nicola Vitiello, and Maria Chiara Carrozza. Self-alignment mechanisms for assistive wearable robots: A kinetostatic compatibility method. IEEE Transactions on Robotics, 29(1):236–250, 2012.

[184] Michael R Tucker, Jeremy Olivier, Anna Pagel, Hannes Bleuler, Mohamed Bouri, Olivier Lambercy, José del R Millán, Robert Riener, Heike Vallery, and Roger Gassert. Control strategies for active lower extremity prosthetics and orthotics: a review. Journal of neuroengineering and rehabilitation, 12(1):1, 2015.

[185] Yasuhiro Akiyama, Yoji Yamada, and Shogo Okamoto. Interaction forces beneath cuffs of physical assistant robots and their motion-based estimation. Advanced Robotics, 29(20):1315–1329, 2015.

[186] Harrison L Bartlett, Lena H Ting, and Jeffrey T Bingham. Accuracy of force and center of pressure measures of the wii balance board. Gait & posture, 39(1):224–228, 2014.

[187] David Tedaldi, Alberto Pretto, and Emanuele Menegatti. A robust and easy to implement method for imu calibration without external equipments. In 2014 IEEE International Conference on Robotics and Automation (ICRA), pages 3042–3049. IEEE, 2014.

[188] Itseez. Open source computer vision library. https://github.com/itseez/opencv, 2015.

[189] Jorge Lobo and Jorge Dias. Relative pose calibration between visual and inertial sensors. The International Journal of Robotics Research, 26(6):561–575, 2007.

[190] Alexander L Bell, Richard A Brand, and Douglas R Pedersen. Prediction of hip joint centre location from external landmarks. Human movement science, 8(1):3–16, 1989.

[191] Rainald M Ehrig, William R Taylor, Georg N Duda, and Markus O Heller. A survey of formal methods for determining the centre of rotation of ball joints. Journal of biomechanics, 39(15):2798–2809, 2006.

[192] Rainald M Ehrig, William R Taylor, Georg N Duda, and Markus O Heller. A survey of formal methods for determining functional joint axes. Journal of biomechanics, 40(10):2150–2157, 2007.

[193] Ko Ayusawa, Gentiane Venture, and Yoshihiko Nakamura. Real-time implementation of physically consistent identification of human body segments. In 2011 IEEE International Conference on Robotics and Automation, pages 6282–6287. IEEE, 2011.

[194] Silvio Traversaro, Stanislas Brossette, Adrien Escande, and Francesco Nori. Identification of fully physical consistent inertial parameters using optimization on manifolds. In 2016 IEEE/RSJ International Conference on Intelligent Robots and Systems (IROS), pages 5446–5451. IEEE, 2016.

[195] Yatiraj K Shetty. Robust Human Motion Tracking Using Low-cost Inertial Sensors. PhD thesis, Arizona State University, 2016.

[196] Manon Kok, Jeroen D Hol, and Thomas B Schön. Using inertial sensors for position and orientation estimation. arXiv preprint arXiv:1704.06053, 2017.

[197] K Nirmal, AG Sreejith, Joice Mathew, Mayuresh Sarpotdar, Ambily Suresh, Ajin Prakash, Margarita Safonova, and Jayant Murthy. Noise modeling and analysis of an imu-based attitude sensor: improvement of performance by filtering and sensor fusion. In Advances in Optical and Mechanical Technologies for Telescopes and Instrumentation II, volume 9912, page 99126W. International Society for Optics and Photonics, 2016.

[198] Oliver J Woodman. An introduction to inertial navigation. Technical report, University of Cambridge, Computer Laboratory, 2007.

[199] Michael B Del Rosario, Heba Khamis, Phillip Ngo, Nigel H Lovell, and Stephen J Redmond. Computationally efficient adaptive error-state kalman filter for attitude estimation. IEEE Sensors Journal, 18(22):9332–9342, 2018.

[200] Nachi Gupta and Raphael Hauser. Kalman filtering with equality and inequality state constraints. arXiv preprint arXiv:0709.2791, 2007.

[201] Jorge Nocedal and Stephen Wright. Numerical optimization. Springer Science & Business Media, 2006.

[202] Jean-Michel Gracies, Nicolas Bayle, Sarah Goldberg, and David M Simpson. Botulinum toxin type b in the spastic arm: a randomized, double-blind, placebo-controlled, preliminary study. Archives of physical medicine and rehabilitation, 95(7):1303–1311, 2014.

[203] Abduljalil Radman, Waidah Ismail, and Mahadi Bahari. Robotic devices for upper limb stroke rehabilitation: Potential research trends. In 2017 IEEE International Symposium on Robotics and Intelligent Sensors (IRIS), pages 383–388. IEEE, 2017.

[204] DT Wade, R Langton-Hewer, Victorine A Wood, CE Skilbeck, and HM Ismail. The hemiplegic arm after stroke: measurement and recovery. Journal of Neurology, Neurosurgery & Psychiatry, 46(6):521–524, 1983.

[205] James Diebel. Representing attitude: Euler angles, unit quaternions, and rotation vectors. Matrix, 58(15-16):1–35, 2006.

[206] George Rab, Kyria Petuskey, and Anita Bagley. A method for determination of upper extremity kinematics. Gait & posture, 15(2):113–119, 2002.

[207] Pietro Cerveri, Antonio Pedotti, and Giancarlo Ferrigno. Robust recovery of human motion from video using kalman filters and virtual humans. Human movement science, 22(3):377–404, 2003.

[208] P. Zarchan and H. Muso. Fundamentals of kalman filtering: A practical approach. 190, 01 2005.

[209] Inge Söderkvist and Per-Åke Wedin. Determining the movements of the skeleton using well-configured markers. Journal of biomechanics, 26(12):1473–1477, 1993.

[210] Melissa MB Morrow, Bethany Lowndes, Emma Fortune, Kenton R Kaufman, and M Susan Hallbeck. Validation of inertial measurement units for upper body kinematics. Journal of applied biomechanics, 33(3):227–232, 2017.

[211] Andrea Giovanni Cutti, Gabriele Paolini, Marco Troncossi, Angelo Cappello, and Angelo Davalli. Soft tissue artefact assessment in humeral axial rotation. Gait & posture, 21(3):341–349, 2005.

[212] Michael H Schwartz and Adam Rozumalski. The gait deviation index: a new comprehensive index of gait pathology. Gait & posture, 28(3):351–357, 2008.

[213] Joel A E Andersson, Joris Gillis, Greg Horn, James B Rawlings, and Moritz Diehl. CasADi – A software framework for nonlinear optimization and optimal control. Mathematical Programming Computation, 11(1):1–36, 2019.

[214] Michael JD Powell. A direct search optimization method that models the objective and constraint functions by linear interpolation. In Advances in optimization and numerical analysis, pages 51–67. Springer, 1994.

[215] Steven G Johnson. The nlopt nonlinear-optimization package, 2014.

[216] Vincent Bonnet, Raphael Dumas, Aurelio Cappozzo, Vladimir Joukov, Gautier DAUNE, Dana Kulic, Philippe Fraisse, Sebastien Andary, and Gentiane Venture. A constrained extended kalman filter for the optimal estimate of kinematics and kinetics of a sagittal symmetric exercise. Journal of biomechanics, 62, 12 2016.

[217] Mohammad Al-Amri, Kevin Nicholas, Kate Button, Valerie Sparkes, Liba Sheeran, and Jennifer L Davies. Inertial measurement units for clinical movement analysis: reliability and concurrent validity. Sensors, 18(3):719, 2018.

[218] JA Zeni Jr, JG Richards, and JS Higginson. Two simple methods for determining gait events during treadmill and overground walking using kinematic data. Gait & posture, 27(4):710–714, 2008.

[219] Kevin Supakkul. Using positional heel-marker data to more accurately calculate stride length for treadmill walking: a step length approach. arXiv preprint arXiv:1710.09030, 2017.

[220] Ming Hao, Ken Chen, and Chenglong Fu. Smoother-based 3-d foot trajectory estimation using inertial sensors. IEEE Transactions on Biomedical Engineering, 66(12):3534–3542, 2019.

[221] Alper Köse, Andrea Cereatti, and Ugo Della Croce. Bilateral step length estimation using a single inertial measurement unit attached to the pelvis. Journal of neuroengineering and rehabilitation, 9(1):9, 2012.

[222] Jay Kim, Natalie Colabianchi, Jeffrey Wensman, and Deanna H Gates. Wearable sensors quantify mobility in people with lower limb amputation during daily life. IEEE Transactions on Neural Systems and Rehabilitation Engineering, 2020.

[223] Sumire Futamure, Vincent Bonnet, Raphael Dumas, and Gentiane Venture. A sensitivity analysis method for the body segment inertial parameters based on ground reaction and joint moment regressor matrices. Journal of biomechanics, 64:85–92, 2017.

[224] Beomsoo Hwang and Doyoung Jeon. A method to accurately estimate the muscular torques of human wearing exoskeletons by torque sensors. Sensors, 15(4):8337–8357, 2015.

[225] Carmichael F Ong, Jennifer L Hicks, and Scott L Delp. Simulation-based design for wearable robotic systems: an optimization framework for enhancing a standing long jump. IEEE Transactions on Biomedical Engineering, 63(5):894–903, 2015.

[226] Valentina Camomilla, Andrea Cereatti, Giuseppe Vannozzi, and Aurelio Cappozzo. An optimized protocol for hip joint centre determination using the functional method. Journal of biomechanics, 39(6):1096–1106, 2006.

[227] Satoshi Hamai, Taka-Aki Moro-Oka, Nicholas J Dunbar, Hiromasa Miura, Yukihide Iwamoto, and Scott A Banks. In vivo healthy knee kinematics during dynamic full flexion. BioMed research international, 2013, 2013.

[228] Yong Feng, Tsung-Yuan Tsai, Jing-Sheng Li, Shaobai Wang, Hai Hu, Changqing Zhang, Harry E Rubash, and Guoan Li. Motion of the femoral condyles in flexion and extension during a continuous lunge. Journal of Orthopaedic Research, 33(4):591–597, 2015.

[229] Arnaud Barre, Rachid Aissaoui, Kamiar Aminian, and Raphaël Dumas. Assessment of the lower limb soft tissue artefact at marker-cluster level with a high-density marker set during walking. Journal of biomechanics, 62:21–26, 2017.

[230] E Grimpampi, Valentina Camomilla, A Cereatti, P De Leva, and Aurelio Cappozzo. Metrics for describing soft-tissue artefact and its effect on pose, size, and shape of marker clusters. IEEE Transactions on Biomedical Engineering, 61(2):362–367, 2013.

[231] Olivera Stojadinovic, Julia Minkiewicz, Andrew Sawaya, Jonathan W Bourne, Peter Torzilli, Juan Pablo de Rivero Vaccari, W Dalton Dietrich, Robert W Keane, and Marjana Tomic-Canic. Deep tissue injury in development of pressure ulcers: a decrease of inflammasome activation and changes in human skin morphology in response to aging and mechanical load. PloS one, 8(8):e69223, 2013.

[232] Walid Hassani, Samer Mohammed, Hala Rifaï, and Yacine Amirat. Emg based approach for wearer-centered control of a knee joint actuated orthosis. In 2013 IEEE/RSJ International Conference on Intelligent Robots and Systems, pages 990–995. IEEE, 2013.

[233] Philippe Moewis, Heide Boeth, Markus O Heller, Caroline Yntema, Tobias Jung, Ralf Doyscher, Rainald M Ehrig, Yanlin Zhong, and William R Taylor. Towards understanding knee joint laxity: Errors in non-invasive assessment of joint rotation can be corrected. Medical engineering & physics, 36(7):889–895, 2014.

[234] Valentina Camomilla, Tecla Bonci, Raphaël Dumas, Laurence Cheze, and Aurelio Cappozzo. A model of the soft tissue artefact rigid component. Journal of biomechanics, 48(10):1752–1759, 2015.

[235] Jennifer L McGinley, Richard Baker, Rory Wolfe, and Meg E Morris. The reliability of three-dimensional kinematic gait measurements: a systematic review. Gait & posture, 29(3):360–369, 2009.

[236] Gentiane Venture, Ko Ayusawa, and Yoshihiko Nakamura. A numerical method for choosing motions with optimal excitation properties for identification of biped dynamics-an application to human. In 2009 IEEE International Conference on Robotics and Automation, pages 1226–1231. IEEE, 2009.

[237] Aurelio Cappozzo. Minimum measured-input models for assessment of motor ability. Journal of biomechanics, 35:437–46, 05 2002.

List of figures

List of tables

List of Publications

Journals:

[1] **R. Mallat**, V. Bonnet, R. Dumas, M. Adjel, G. Venture, M. Khalil, S. Mohammed "Sparse Visual-Inertial Measurement Units Placement for GaitKinematics Assessment", *IEEE Transactions on Neural Systems and Rehabilitation Engineering*, 2020. (In revision)

[2] **R. Mallat**, V. Bonnet, M. Khalil, S. Mohammed, "Upper Limbs Kinematics Estimation Using Affordable Visual-Inertial Sensors", *IEEE Transactions on Automation Science and Engineering*, 2020.

Peer-review Conferences:

[3] **R. Mallat**, V. Bonnet, G. Venture, R. Dumas, M. Khalil, S. Mohammed, "Dynamics Assessment and Minimal Model of an Orthosis-Assisted Knee Motion", *IEEE RAS/EMBS International Conference for Biomedical Robotics and Biomechatronics (BioRob)*, pp. 352-357, 2020.

[4] **R. Mallat**, V. Bonnet, G. Venture, M. Khalil, S. Mohammed, "Human-Exoskeleton Joint Misalignment: A Systematic Review", *IEEE International Conference on Advances in Biomedical Engineering (ICABME)*, pp. 1-4, 2019.

[5] **R. Mallat**, V. Bonnet, W. Huo, P. Karasinski, Y. Amirat, M. Khalil, and S. Mohammed, "Human-Exoskeleton System Dynamics Identification Using Affordable Sensors", *IEEE International Conference on Robotics and Automation (ICRA)*, pp. 6759-6765, 2018.

[6] **R. Mallat**, V. Bonnet, M. Khalil, S. Mohammed, "Toward an Affordable Multi-Modal Motion Capture System Framework for Human Kinematics and Kinetics Assessment", *International Symposium on Wearable Robotics, (WeRob)*, pp. 6759-6765, 2018.

[7] **R. Mallat**, V. Bonnet, M. Khalil, S. Mohammed, "Dynamic Identification of a Human-Exoskeleton System", *IEEE International Conference on Advances in Biomedical Engineering (ICABME)*, pp. 1-4, 2017.